Application of Matrix Methods for Investigation of Silicon Based Layered Structures

Sergey Dyakov

Trinity College

University of Dublin

A thesis submitted for the degree of

Doctor of Philosophy

2012

Declaration

I declare that this thesis has not been submitted as an exercise for a degree at this or any other university and it is entirely my own work.

I agree to deposit this thesis in the University's open access institutional repository or allow the library to do so on my behalf, subject to Irish Copyright Legislation and Trinity College Library conditions of use and acknowledgement.

Sergey Dyakov

24^{st} of September, 2012
Dublin

To my mother and to my relatives

Abstract

This work is dedicated to the theoretical and experimental investigation of the influence of nano- and microstructuring of silicon systems on their linear optical response. The wavelengths of the light are comparable to the typical size of the investigated structures. For calculation of passive and active optical characteristics in the considered spectral range, the transfer and the scattering matrix methods are used.

The variety of the silicon based samples is considered. Firstly the light propagation through the two-dimensional silicon photonic crystals was investigated experimentally and theoretically. It was demonstrated that the presence of the air/photonic crystal interface leads to appearance of the dips in the reflection spectra in the region of photonic stop-bands. These dips were found to be the surface modes.

Then, the reflection spectra of the grooved silicon structures were investigated. It was found that the scattering matrix method enables us to achieve a good agreement between theoretical and experimental effective refractive indexes of these structures in the spectral range where the effective medium theory is not applicable.

Finally, the intensity of the active optical response from the multilayered structures was studied. It was shown that the intensity of photoluminescence as well as the Raman scattering strongly depends on the thickness and material property of all the layers. The corresponding experimental analysis of the photoluminescence of triple-layered structures with silicon nanocrystals, the Raman scattering from one-dimensional photonic crystal based on porous silicon as well

as the Raman scattering from graphene layer demonstrate excellent agreement with theoretical results.

Acknowledgements

I would like to express my gratitude to several people who have helped me to make this thesis possible.

Firstly, I would like to sincerely thank my supervisor, Prof. Tatiana Perova, for giving me the opportunity to undertake this research project, her time, encouragement and support throughout my work.

This research project has involved collaborative work with four other groups. I would like to express my sincere gratitude to Dr. Ekaterina Astrova, Ioffe Physical Technical Institute, Sankt-Peterburg, Russia, for support, numerous discussions and for providing me with the samples of two-dimensional photonic crystal fabricated by photoelectrochemical etching. I would like sincerely thank Prof. Sergei Tikhodeev from Prokhorov General Physics Institute for inspiring discussions and the opportunity to use the scattering matrix method. I would like to express my acknowledgments to Dr. Denis Zhigunov from Moscow State University for support and essential contribution to the part of the work devoted to the silicon nanocrystals. Many thanks to Prof. Margit Zacharias and Andreas Hartel, Albert Ludwig's University Freiburg, Germany, for the samples with silicon nanocrystals. I would like also thank Prof. Ya-Hong Xie from the Univeristy of Los Angeles for the opportunity to use the sample with high-quality graphene layer.

I thank Prof. V. Yu. Timoshenko from Moscow State University and Prof. N. A. Gippius from the University of Blaise Pascal, Aubiere, France, for support and helpful discussions.

Many thanks to Anna Baldycheva for FTIR measurments of two-dimensional photonic crystals, Yulia Zharova and Galina Li for a lot

of work on the fabrication of the samples with two-dimensional photonic crystals, Congqin Miao for the fabrication of the samples with graphene, Dmitri Kostenko and Andrey Emelyanov for contribution to this work.

I would like to express my acknowledgements to the members of our research group: Viktor Ermakov, David Adley, Elena Krutkova, Joanna Wasyluk and Franz Schmied for their help and interests.

I would like to acknowledge the full financial support from the IRCSET and Trinity College Dublin throughout my PhD work.

I express my acknowledgments to my mother, my wife, aunt Tania, sister Olga and my little nephew Alexey for their permanent support and love. I also thank my friends, Denis and Tatiana, Dmitry and Julia, Peter and Alexandra, Dmitry, Nikolay, Ivan, Alexey, Katia, Andreas, Irina, Alexander and Elena for their ongoing support. Thank you, my Irish friends, David, Julie, Imant, Vitaly, Arayik and Misha for providing me a good time on the way.

Contents

List of Figures

List of Tables

Author's Publications

Peer Reviewed Publications

1. S. A. Dyakov, A. Baldycheva, T. S. Perova, G. V. Li, E. V. Astrova, N. A. Gippius, and S. G. Tikhodeev, "Surface states in the optical spectra of two-dimensional photonic crystals with various surface terminations," *Phys. Rev. B*, vol. 86, p. 115126, 2012.

2. S. A. Dyakov, D. M. Zhigunov, A. Hartel, M. Zacharias, T. S. Perova, and V. Y. Timoshenko, "Enhancement of photoluminescence signal from ultrathin layers with silicon nanocrystals," *Appl. Phys. Lett.*, vol. 100, no. 6, p. 061908, 2012.

3. D. M. Zhigunov, S. A. Dyakov, V. Y. Timoshenko, A. N. Yablonskiy, D. Hiller, and M. Zacharias, "Photoluminescence properties of er-implanted sio/sio2 multilayered structures with amorphous or crystalline si nanoclusters," *Journal of Nanoelectronics and Optoelectronics*, vol. 6, no. 4, pp. 491–494, 2011.

4. S. A. Dyakov, E. V. Astrova, T. S. Perova, S. G. Tikhodeev, N. A. Gippius, and V. Y. Timoshenko, "Optical properties of grooved silicon microstructures: theory and experiment," *JETP*, vol. 113, no. 1, pp. 80–85, 2011.

5. S. A. Dyakov, E. V. Astrova, T. S. Perova, G. V. Fedulova, A. Baldycheva, V. Y. Timoshenko, S. G. Tikhodeev, and N. A. Gippius, "Optical spectra of two-dimensional photonic crystal bars based on macroporous Si," *SPIE Proc.*, vol. 7943, p. 79431I, 2011.

6. I. I. Shaganov, T. S. Perova, V. A. Melnikov, S. A. Dyakov, and K. Berwick, "Size effect on the infrared spectra of condensed media under conditions of 1D, 2D, and 3D dielectric confinement," *J. Phys. Chem. C*, vol. 114, no. 39, pp. 16071–16081, 2010.

7. S. A. Dyakov, D. M. Zhigunov, and V. Y. Timoshenko, "Specific features of erbium ion photoluminescence in structures with amorphous and crystalline silicon nanoclusters in silica matrix," *Semiconductors*, vol. 44, no. 4, pp. 467–471, 2010.

8. D. M. Zhigunov, V. N. Seminogov, V. Y. Timoshenko, V. I. Sokolov, V. N. Glebov, A. M. Malyutin, N. E. Maslova, O. A. Shalygina, S. A. Dyakov, A. S. Akhmanov, V. Y. Panchenko, and P. K. Kashkarov, "Effect of thermal annealing on structure and photoluminescence properties of silicon-rich silicon oxides," *Physica E*, vol. 41, no. 6, pp. 1006–1009, 2009.

9. S. A. Dyakov, E. V. Astrova, S. G. Tikhodeev, V. Y. Timoshenko, and T. S. Perova, "Numerical methods for calculation of optical properties of layered structures," *SPIE Proc.*, vol. 7521, p. 75210G, 2009.

Selected Talks

1. S. A. Dyakov, D. M. Zhigunov, A. Hartel, M. Zacharias, and T. S. Perova, "Interference enhancement of photoluminescence signal from thin layers with silicon nanocrystals," in *Proceedings of the Microscopical Society of Ireland Symposium. Program and Abstracts*, (Cork, Ireland), p. 58, University College Cork, 29–31 August 2012. Students Best Oral Presentation Award.

2. S. A. Dyakov, D. M. Zhigunov, A. Hartel, M. Zacharias, and T. S. Perova, "Interference enhancement of photoluminescence signal from thin layers with silicon nanocrystals," in *Program of the International Conference on Nanoscience + Technology*, (Paris, France), p. 262, Sorbonne, 23–27 July 2012.

3. S. A. Dyakov, D. M. Zhigunov, T. S. Perova, A. Hartel, D. Hiller, and M. Zacharias, "Modeling of photoluminescence intensitiy of ultrathin layer with silicon nanocrystals," in *SPIE Optics + Photonics. Technical Program*, (San Diego, California, USA), p. 61, Convention Center, 23–27 August 2011.

4. S. A. Dyakov, A. Baldycheva, T. S. Perova, E. V. Astrova, and S. G. Tikhodeev, "Optical properties of two-dimensional photonic crystal bars obtained by photoelectrochemical etching of silicon," in *Proceedings of the Microscopical Society of Ireland and the Northern Ireland Biomedical Engineering Society Joint Annual Symposium*, (Jordanstown, Northern Ireland, UK), pp. 11, 18, University of Ulster, 25–27 August 2010.

5. S. A. Dyakov, "Optical characterization of aluminium oxide nanolayers deposited on si membrane," in *Queens University Belfast joint seminar*, (Belfast, Northern Ireland, UK), Queens University Belfast, 24 August 2010.

6. S. A. Dyakov and D. M. Zhigunov, "Spatial light localization in grooved silicon matrix," in *Program of X International Conference Laser and Laser Information Technologies*, (Smolyan, Bulgaria), p. 6, 18–22 October 2009.

Selected Posters

1. S. Dyakov, T. Perova, and Y.-H. Xie, "Interference enhancement of raman signal from layer of graphene," in *Procedings of the International Conference on Nanoscience + Technology*, (Paris, France), p. 154, Sorbonne, 23–27 July 2012.

2. S. A. Dyakov, T. S. Perova, A. V. Baldycheva, E. V. Astrova, G. V. Li, S. G. Tikhodeev, and N. A. Gippius, "Optical properties of two-dimensional photonic crystal bars fabricated by photoelectro-chemical etching of silicon," in *Materials of 8th International Conference Porous Semiconductors Science and Technology*, (Malaga, Spain), p. 243, 25–30 March 2012.

3. A. Baldycheva, S. A. Dyakov, Y. A. Zharova, E. V. Astrova, G. Fedulova, K. Berwick, and T. S. Perova, "Multi-component band-gap devices for integrated silicon microphotonics," in *Conference programme of International Conference Photonics Ireland*, (Malahide, Ireland), p. 2, 7–9 September 2011.

4. S. A. Dyakov, E. V. Astrova, T. S. Perova, G. V. Fedulova, A. Baldycheva, T. V. Yu., S. G. Tikhodeev, and N. A. Gippius, "Optical spectra of two-dimensional photonic crystal bars based on macroporous si," in *Technical Summaries of 20th International Congress on Photonics in Europe*, (Munich, Germany), p. 15, International Conference Centre, 23–26 May 2011.

5. S. A. Dyakov, S. G. Tikhodeev, E. V. Astrova, T. S. Perova, and T. V. Yu., "Investigation of optical properties of one and two-dimensional photonic crystals by means of the scattering matrix method," in *Technical Programme of SPIE Photonics Europe*, (Brussels, Belgium), p. 45, The Square Conference Center, 12–16 April 2010.

6. S. A. Dyakov, E. V. Astrova, T. S. Perova, G. V. Fedulova, A. Baldycheva, T. V. Yu., S. G. Tikhodeev, and N. A. Gippius, "Optical spectra of two-dimensional photonic crystal bars based on macroporous si," in *Technical Programme of SPIE Photonics West*, (San Francisco, California, USA), The Moscone Center, 22–27 January 2010.

7. A. Baldycheva, S. A. Dyakov, K. Berwick, and T. S. Perova, "Tuning of the optical contrast in three-component one-dimensional photonic crystals," in *Conference programme of International Conference Photonics Ireland*, (Kinsale, Ireland), 14–16 September 2009.

8. S. A. Dyakov, A. V. Emelyanov, T. S. Perova, E. V. Astrova, S. G. Tikhodeev, and T. V. Yu., "Ftir microscopy for investigation of properties of grooved silicon: comparison with simulation by scattering matrix method.," in *Proceedings of the Microscopical Society of Ireland Symposium. Program and Abstracts*, (Dublin, Ireland), University College Dublin, 26–28 August 2009.

Chapter 1

Introduction

This thesis is devoted to the investigation of optical properties of nano-and microstructured silicon materials. These structures attracted a great interest of researches due to their potential in fabrication of photonic and optoelectronic devices.

One of the main problems of up-to-date microelectronics is an increase of the information transmission rate. This problem can be solved by creating of the integrated circuits, which contain both electronic and optical elements where the information is transferred by photons. A non-direct band gap as well as an isotropy of the linear optical properties of the main material of microelectronis, silicon, imposes a restriction on its use in fabrication of optical elements. The way out of this situation is a construction of silicon-based nano-and microstructures, which on the one hand possess a strong anisotropy of the optical properties while on the other hand could be the basis of light-emitting devices. Thus by setting a specific geometry of these structures, we can control the light propagation in them. All of these lead to the need for a detailed study of interaction of light with silicon nano and microstructures.

In the present work the interaction of light with periodical one-dimensional and two-dimensional photonic structures is considered. The typical size of the spatial inhomogeneity of the refractive index in the investigated structures is comparable to the light wavelength. In this case the approaches of the effective medium theory as well as of the geometrical optics cannot be applied for calculation of optical characteristics of solids. Different theoretical methods were

developed for the modeling of light propagation in structures with complex geometry, particularly, in photonic crystals. The plane wave expansion method is used for infinite one-, two- and three-dimensional photonic crystals [1]. The spherical-wave expansion method is developed for photonic crystals which are formed by dielectric spheres and cylinders [2, 3]. The 2×2 transfer matrix method [4, 5, 6, 7] is very elegant approach which is applicable for any periodic structures, however, it is not suitable for modeling of the structures with thick absorbing layers, due to a problem with mixing of the large and small numbers in the transfer matrix [8, 9]. The Finite-Difference Time Domain (FDTD) method [1, 10] is the most common one, but it is very time-consuming. The scattering matrix method was developed for the calculation of optical characteristics of the complex structures which can be presented as a system of layers homogeneous along vertical axis and periodical in one or two horizontal directions. In this work we use both the transfer matrix method and the scattering matrix method for the investigation of optical properties of the structures for which these methods are the most appropriate.

Chapter 2

Theoretical methods

The evaluation of propagation of the electromagnetic waves through a structure can be performed by different calculation methods such as plane wave expansion method [1], transfer matrix method [4, 11, 12], scattering matrix method [8, 9, 13], finite-difference time-domain method [10] etc. In the present work the 2×2 Transfer Matrix Method (TMM) and the Scattering Matrix Method (SMM) are used. The TMM is applicable for calculation of optical characteristics of multilayered structures whereas the SMM is the most useful method for investigation of optical properties of structures with complex geometry.

2.1 Transfer matrix method

In the course of study of optical properties of layered structures the most important part is the calculation of such characteristics as reflection, transmission and absorption coefficients as well as the distribution of electric and magnetic fields of the incident light. Another common part of the investigation of optical properties of layered structures is the simulation of active optical response related to the generation of photons of energies other than the energy of the excitation light. For evaluation of above mentioned parameters the most useful method is 2×2 transfer matrix method [4, 11, 12, 14]. In the present section the general procedure of calculation of optical properties by means of TMM is considered.

2.1.1 Calculation of passive optical response

2.1.1.1 Mathematical problem of TMM

Let us consider a system of the N parallel layers placed between two semi-infinite media $\tilde{n}_{01}$ and $\tilde{n}_{02}$ (Fig. 2.1). All substances are considered to be linear homogeneous and isotropic. We assume that the wave vector of incident light is $\vec{k}$, the polarization of incident light is linear and is characterized by the known direction, thicknesses of layers d_j ($j = 1, 2, \ldots, N$), their complex dielectric permittivities $\tilde{\varepsilon}_j = \varepsilon'_j - \varepsilon''_j i$ where i is the complex unit and complex magnetic permeabilities $\tilde{\mu}_j = \mu'_j - \mu''_j i$. We define a z-coordinate of the interface between j and $j+1$ layers as z_j. The mathematical problem of the transfer matrix method is the calculation of the reflection, transmission and absorption coefficients and electromagnetic field distribution of a plane electromagnetic wave propagating through the described layered structure.

2.1.1.2 Plane electromagnetic waves in media

In accordance with the approach described in [11], let us consider a linearly polarized plane electromagnetic wave traveling at an angle of φ ($0 \leq \varphi < \pi/2$) to the positive[1] direction of z-axis in a homogeneous isotropic medium (see Fig. 2.2a). The wave vector has the coordinates $\vec{k} \equiv \{k_x, k_y, k_z\} = \{\frac{2\pi\tilde{n}}{\lambda}\sin\varphi, 0, \frac{2\pi\tilde{n}}{\lambda}\cos\varphi\}$,

[1] We assume that an electromagnetic wave propagates in the *positive* direction of z-axis if the angle between the positive direction of z-axis and the wave vector $\vec{k}$ is less than $\pi/2$ and in *negative* direction if this angle is higher than $\pi/2$. We will characterize the propagation of light by the angle of $\varphi < \pi/2$.

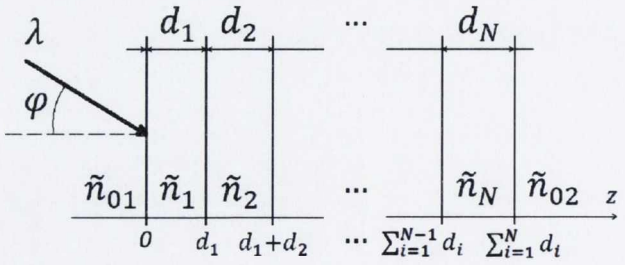

Figure 2.1: Schematic representation of the layered structure.

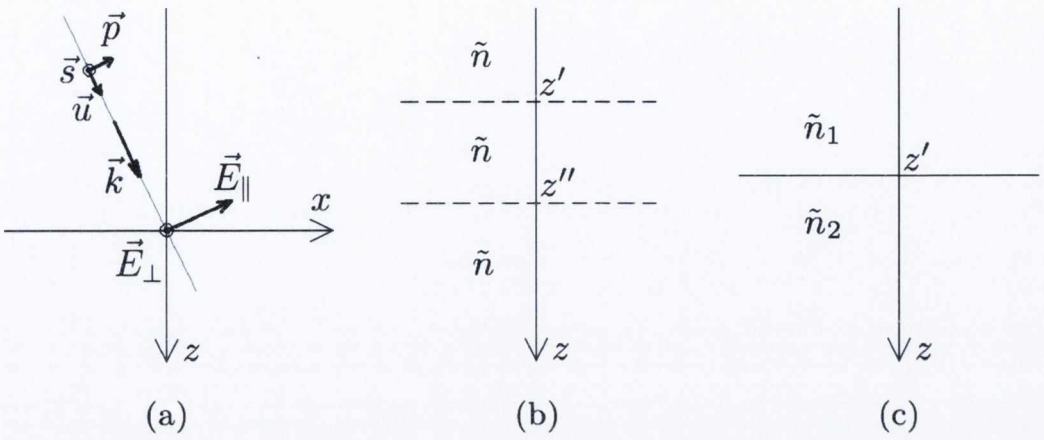

Figure 2.2: (a) Plane electromagnetic wave traveling in isotropic homogeneous medium. (b) Two parallel planes z' and z''. (c) Interface between two media with different dielectric permittivities $\tilde{\varepsilon}_1$ and $\tilde{\varepsilon}_2$

where the complex refractive index $\tilde{n} \equiv n - i\kappa = \sqrt{\tilde{\varepsilon}\tilde{\mu}}$. Let us expand the electric field vector of the wave into two components, $\vec{E}_{\perp}$ and $\vec{E}_{\parallel}$, parallel and perpendicular to the plane of incidence:

$$\vec{E}(x,y,z,t) = \vec{E}_{\parallel}(x,y,z,t) + \vec{E}_{\perp}(x,y,z,t). \tag{2.1}$$

Components of the electric field vectors can be written as

$$\vec{E}_{\parallel}(x,y,z,t) = E_0 \vec{p} \sin\theta \cdot e^{-ik_z z - ik_x x} \cdot e^{i\omega t}, \tag{2.2}$$

$$\vec{E}_{\perp}(x,y,z,t) = E_0 \vec{s} \cos\theta \cdot e^{-ik_z z - ik_x x} \cdot e^{i\omega t}, \tag{2.3}$$

where θ is the angle between vectors $\vec{E}$ and $\vec{E}_{\perp}$. The unit vectors $\vec{s}$ and $\vec{p}$ have the coordinates

$$\vec{p} = \{\cos\varphi, 0, -\sin\varphi\}, \tag{2.4}$$

$$\vec{s} = \{0, 1, 0\}. \tag{2.5}$$

The vectors $\vec{s}$ and $\vec{p}$ are the directions of oscillation of parallel and perpendicular component of the electric field. If the electric field vector $\vec{E}$ of the electromagnetic

wave oscillates along $\vec{s}$-direction then this wave is called s-polarized, along $\vec{p}$-direction the wave is called p-polarized.

Expressions for the components of electric field (2.2) and (2.3) can be written in the following form:

$$\vec{E}_{\parallel}(x,y,z,t) = E_{\parallel}(z)\vec{p}\cdot e^{-ik_x x+i\omega t}, \tag{2.6}$$

$$\vec{E}_{\perp}(x,y,z,t) = E_{\perp}(z)\vec{s}\cdot e^{-ik_x x+i\omega t}, \tag{2.7}$$

where $E_{\parallel}(z)$, $E_{\perp}(z)$ are the amplitudes of the electric field at z-coordinate: $E_{\parallel}(z) = E_0 e^{-ik_z z}\sin\theta$ and $E_{\perp}(z) = E_0 e^{-ik_z z}\cos\theta$. The magnetic field vector can be easily obtained from the known relation between the electric and magnetic field vectors of in plane electromagnetic wave $\vec{H} = \sqrt{\frac{\tilde{\varepsilon}}{\tilde{\mu}}}\left[\vec{u}\times\vec{E}\right]$, where $\vec{u} = Re\left[\frac{\vec{k}}{\|\vec{k}\|}\right]$:

$$\vec{H}_{\parallel}(x,y,z,t) = -\sqrt{\frac{\tilde{\varepsilon}}{\tilde{\mu}}}E_{\perp}(z)\vec{p}\cdot e^{-ik_x x+i\omega t}, \tag{2.8}$$

$$\vec{H}_{\perp}(x,y,z,t) = +\sqrt{\frac{\tilde{\varepsilon}}{\tilde{\mu}}}E_{\parallel}(z)\vec{s}\cdot e^{-ik_x x+i\omega t}. \tag{2.9}$$

The time average energy densities of electric and magnetic fields are

$$w_E(x,y,z) = \frac{\varepsilon'}{16\pi}\left(\vec{E}\vec{E}^*\right), \tag{2.10}$$

$$w_H(x,y,z) = \frac{\mu'}{16\pi}\left(\vec{H}\vec{H}^*\right). \tag{2.11}$$

The time average vector of energy flux density is

$$\langle\vec{S}\rangle = Re\left(\frac{c}{8\pi}\left[\vec{E}\times\vec{H}^*\right]\right). \tag{2.12}$$

2.1.1.3 Plane electromagnetic waves in layered structure

Let us consider to the propagation of an incident plane wave through the layered structure shown in Fig. 2.1. An incident monochromatic wave partially is reflected from the surface $z = 0$ and is partially penetrated into the first layer.

The penetrated wave is partially reflected on the surface $z = d_1$ and partially continues traveling into the sample. The plane wave reflected from the surface $z = d_1$ is partially transmitted through the surface $z = 0$ and partially travels back. As a result the electromagnetic field in each layer is a sum of forward- and backward-traveling plane waves. Thus, the parallel and perpendicular components of the electrical field of the electromagnetic wave in z coordinate of the stratified structure can be represented as:

$$\vec{E}_{\parallel}(x,y,z,t) = \vec{E}^{+}_{\parallel}(x,y,z,t) + \vec{E}^{-}_{\parallel}(x,y,z,t), \tag{2.13}$$

$$\vec{E}_{\perp}(x,y,z,t) = \vec{E}^{+}_{\perp}(x,y,z,t) + \vec{E}^{-}_{\perp}(x,y,z,t), \tag{2.14}$$

where $\vec{E}^{+}_{\parallel,\perp}(x,y,z,t)$ and $\vec{E}^{-}_{\parallel,\perp}(x,y,z,t)$ denote the forward- and backward-traveling plane waves. The wave vector of forward-traveling plane wave in j-th layer has the following coordinates:

$$\vec{k}^{(j)}_{+} = \left\{ \frac{2\pi\tilde{n}_j}{\lambda} \sin\varphi_j, 0, \frac{2\pi\tilde{n}}{\lambda} \cos\varphi_j \right\} \equiv \{k_x, 0, k_z\}, \tag{2.15}$$

while the wave vector of backward-traveling plane wave is:

$$\vec{k}^{(j)}_{-} = \{k_x, 0, -k_z\}. \tag{2.16}$$

The expressions for $\sin\varphi_j$ and $\cos\varphi_j$ can be found from the Snell's law:

$$\sin\varphi_j = \frac{\tilde{n}_{01}\sin\varphi}{\tilde{n}_j}, \tag{2.17}$$

$$\cos\varphi_j = \sqrt{1 - \left(\frac{\tilde{n}_{01}\sin\varphi}{\tilde{n}_j}\right)^2}. \tag{2.18}$$

If the remaining square root in formula (2.18) is negative then the cosine of the angle of wave propagation can be found from the following formal expression:

$$\cos\varphi_j = -i\sqrt{\left(\frac{\tilde{n}_{01}\sin\varphi}{\tilde{n}_j}\right)^2 - 1}. \tag{2.19}$$

For simplicity we will skip symbols "+", "-", and "j" later on. In accordance with (2.15) , (2.16) we will use only k_x k_z.

As

$$\vec{E}_{\parallel}^{\pm}(x,y,z,t) = E_{\pm}\sin\theta\,\vec{p}_{\pm}e^{\mp ik_z z - ik_x x}\cdot e^{i\omega t}, \tag{2.20}$$

$$\vec{E}_{\perp}^{\pm}(x,y,z,t) = E_{\pm}\cos\theta\,\vec{s}_{\pm}e^{\mp ik_z z - ik_x x}\cdot e^{i\omega t}, \tag{2.21}$$

where

$$\vec{p}_{\pm} = \{\pm\cos\varphi_j, 0, -\sin\varphi_j\}, \qquad \vec{s}_{\pm} = \{0,1,0\}, \tag{2.22}$$

then the electric field vectors at z-coordinate are

$$\vec{E}_{\parallel}(x,y,z,t) = \left[E_{\parallel}^{+}(z)\vec{p}_{+} + E_{\parallel}^{-}(z)\vec{p}_{-}\right]\cdot e^{-ik_x x + i\omega t}, \tag{2.23}$$

$$\vec{E}_{\perp}(x,y,z,t) = \left[E_{\perp}^{+}(z)\vec{s}_{+} + E_{\perp}^{-}(z)\vec{s}_{-}\right]\cdot e^{-ik_x x + i\omega t}, \tag{2.24}$$

where

$$E_{\parallel}^{\pm}(z) = E_{\pm}\sin\theta\,e^{-ik_z z}, \tag{2.25}$$

$$E_{\perp}^{\pm}(z) = E_{\pm}\cos\theta\,e^{-ik_z z}. \tag{2.26}$$

We can obtain the expressions for the parallel and perpendicular components of the magnetic field from the equations (2.8) and (2.9):

$$\vec{H}_{\parallel}(x,y,z,t) = \sqrt{\frac{\tilde{\varepsilon}}{\tilde{\mu}}}\left[E_{\perp}^{+}(z)\vec{p}_{+} + E_{\perp}^{-}(z)\vec{p}_{-}\right]\cdot e^{-ik_x x + i\omega t}, \tag{2.27}$$

$$\vec{H}_{\perp}(x,y,z,t) = -\sqrt{\frac{\tilde{\varepsilon}}{\tilde{\mu}}}\left[E_{\parallel}^{+}(z)\vec{s}_{+} + E_{\parallel}^{-}(z)\vec{s}_{-}\right]\cdot e^{-ik_x x + i\omega t}. \tag{2.28}$$

As can be seen from equations (2.20-2.24), the electrical field in each layer is characterized by the amplitudes of forward- and backward-traveling plane waves $\vec{E}_{\parallel}^{\pm}(z)$ and $\vec{E}_{\perp}^{\pm}(z)$, and by the components of the wave vector, k_x k_z, in this layer.

Let us now introduce 2×1-column vectors of amplitudes

$$\mathbf{E}_{\parallel}(z) \equiv \begin{bmatrix} E_{\parallel}^{+}(z) \\ E_{\parallel}^{-}(z) \end{bmatrix}, \tag{2.29}$$

$$\mathbf{E}_{\perp}(z) \equiv \begin{bmatrix} E_{\perp}^{+}(z) \\ E_{\perp}^{-}(z) \end{bmatrix}. \tag{2.30}$$

We will skip symbols "$\parallel$" and "$\perp$" for simplicity later on. Thus, the vectors $\mathbf{E}(z)$ and $\vec{k}$ characterizes the propagation of plane electromagnetic waves in a layer.

2.1.1.4 Phase shift of amplitude vector

Let us consider two plane electromagnetic waves traveling through medium $\tilde{\varepsilon}$ (Fig. 2.2b) in forward- and backward directions:

$$\vec{E}^{+}(x,y,z,t) = E^{+}(z)\vec{a}e^{-ik_x x} \cdot e^{i\omega t}, \tag{2.31}$$

$$\vec{E}^{-}(x,y,z,t) = E^{-}(z)\vec{a}e^{-ik_x x} \cdot e^{i\omega t}, \tag{2.32}$$

where $\vec{a}$ is either $\vec{s}$ or $\vec{p}$. It is quite easy to obtain the following relation between amplitudes $E^{\pm}(z')$ and $E^{\pm}(z'')$ from equations (2.25) and (2.26):

$$E^{\pm}(z') = E^{\pm}(z'') \cdot e^{\pm ik_z(z''-z')}. \tag{2.33}$$

Equation (2.33) leads to the relation between vectors $\mathbf{E}(z')$ and $\mathbf{E}(z'')$:

$$\begin{bmatrix} E^{+}(z') \\ E^{-}(z') \end{bmatrix} = \begin{pmatrix} e^{ik_z(z''-z')} & 0 \\ 0 & e^{-ik_z(z''-z')} \end{pmatrix} \begin{bmatrix} E^{+}(z'') \\ E^{-}(z'') \end{bmatrix}. \tag{2.34}$$

More precisely, equation (2.34) can be written as

$$\mathbf{E}(z') = \mathbb{P}\mathbf{E}(z''), \tag{2.35}$$

where

$$\mathbb{P} = \begin{pmatrix} e^{ik_z(z''-z')} & 0 \\ 0 & e^{-ik_z(z''-z')} \end{pmatrix}. \tag{2.36}$$

The matrix $\mathbb{P}$ is called a *propagation matrix*. Equations (2.34)–(2.36) are valid for both perpendicular and parallel orientations of the electric field vector.

2.1.1.5 Interaction of plane wave with an interface

An electromagnetic field of a plane wave traveling in the positive direction in the homogeneous isotropic medium is characterized by the vector of amplitudes

$$\mathbf{E}(z) = \begin{bmatrix} E^+(z) \\ 0 \end{bmatrix}. \tag{2.37}$$

Equation (2.37) implies that there is no backward-traveling plane waves, because $E^-(z) = 0$. In contrast, if a plane wave propagates in the negative direction, the vector of amplitudes is

$$\mathbf{E}(z) = \begin{bmatrix} 0 \\ E^-(z) \end{bmatrix}. \tag{2.38}$$

Les us now consider an interface at z'-coordinate between two media $\tilde{\varepsilon}_1$ and $\tilde{\varepsilon}_2$. Let then two above described electromagnetic plane waves travel simultaneously and their angles of incidence are φ_1 and φ_2 (Fig. 2.2c). It is essential that $\tilde{n}_1 \sin\varphi_1 = \tilde{n}_2 \sin\varphi_2$. In this case the electromagnetic field is characterized by vectors

$$\mathbf{E}_a(z) = \begin{bmatrix} E^+(z) \\ E^-(z) \end{bmatrix}_a \qquad (z < z'), \tag{2.39}$$

$$\mathbf{E}_b(z) = \begin{bmatrix} E^+(z) \\ E^-(z) \end{bmatrix}_b \qquad (z > z'). \tag{2.40}$$

We would like to find matrix $\mathbb{I}$ which makes relation between vectors $\mathbf{E}(z' - 0)$ and $\mathbf{E}(z' + 0)$ [1]:

$$\begin{bmatrix} E^+(z' - 0) \\ E^-(z' - 0) \end{bmatrix} = \begin{pmatrix} I_{11} & I_{12} \\ I_{21} & I_{22} \end{pmatrix} \begin{bmatrix} E^+(z' + 0) \\ E^-(z' + 0) \end{bmatrix}, \tag{2.41}$$

or briefly

$$\mathbf{E}(z' - 0) = \mathbb{I}\mathbf{E}(z' + 0). \tag{2.42}$$

[1] Strength of electric and magnetic fields as well as vector $\mathbf{E}(z)$ are not defined at $z = z_k$, because some of the components of electric and magnetic fields have discontinuity of the first kind at these z-coordinates. Hence in this work we introduce the following notation: $z' \pm 0 = \lim_{\varepsilon \to 0} (z' \pm \varepsilon)$.

Let us consider the special case when only one plane wave is incident on the z'-interface. The complex amplitudes of the transmitted and reflected plane waves in media $\tilde{\varepsilon}_2$ and $\tilde{\varepsilon}_1$ are given, respectively, by

$$E^+(z'+0) = tE^+(z'-0), \tag{2.43}$$

$$E^-(z'-0) = rE^+(z'-0), \tag{2.44}$$

and $E^-(z'+0) = 0$, where r and t are the Fresnel reflection and transmission coefficients of the z'-interface. Elements I_{11} and I_{12} can be found from equations (2.41), (2.43) and (2.44):

$$I_{11} = \frac{1}{t}, \qquad I_{12} = \frac{r}{t}. \tag{2.45}$$

Elements I_{21} and I_{22} can be found by considering another special case when backward-traveling plane wave interacts with the z_0-interface. Using symmetry considerations [11] we find that

$$I_{21} = \frac{r}{t}, \qquad I_{22} = \frac{1}{t} \tag{2.46}$$

and therefore

$$\mathbb{I} = \frac{1}{t}\begin{pmatrix} 1 & r \\ r & 1 \end{pmatrix}. \tag{2.47}$$

Formulas (2.37)–(2.47) are valid for both components of electric field vector, however the Fresnel coefficients for parallel and perpendicular components are different [11]:

$$r_\parallel = \frac{\tilde{\varepsilon}_2\tilde{\mu}_1 k'_z - \tilde{\varepsilon}_1\tilde{\mu}_2 k''_z}{\tilde{\varepsilon}_2\tilde{\mu}_1 k'_z + \tilde{\varepsilon}_1\tilde{\mu}_2 k''_z}, \qquad r_\perp = \frac{\tilde{\mu}_2 k'_z - \tilde{\mu}_1 k''_z}{\tilde{\mu}_2 k'_z + \tilde{\mu}_1 k''_z} \tag{2.48}$$

$$t_\parallel = \frac{2\sqrt{\tilde{\varepsilon}_1\tilde{\varepsilon}_2}\mu_2 k'_z}{\tilde{\varepsilon}_2\tilde{\mu}_1 k'_z + \tilde{\varepsilon}_1\tilde{\mu}_2 k''_z}, \qquad t_\perp = \frac{2\tilde{\mu}_2 k'_z}{\tilde{\mu}_2 k'_z + \tilde{\mu}_1 k''_z}, \tag{2.49}$$

where k'_z and k''_z are the z-components of wave vectors of forward-traveling waves in media $\tilde{\varepsilon}_1$ and $\tilde{\varepsilon}_2$.

Matrix $\mathbb{I}$ is called an *interface matrix*. It establishes relation between vectors of amplitudes $\mathbf{E}(z'-0)$ and $\mathbf{E}(z'+0)$ at immediately opposite sides of the z_0-interface.

2.1.1.6 Transfer matrix

Let us now consider to the stratified structure shown in Fig. 2.1. It consists of two semi-infinite media, interfaces and spaces between the interfaces. The incident electromagnetic wave initiates forward- and backward-traveling plane waves in each layer. The interface and propagation matrices enable us to relate the vector of amplitudes $\mathbf{E}(z_0-0)$ before the structure at $z=0$ with the vector of amplitudes at any other z-coordinate.

A matrix $\mathbb{T}$ which establishes relation between vectors of amplitudes $\mathbf{E}(z_0-0)$ and $\mathbf{E}(z_N+0)$ is called a *total transfer matrix* of the structure.

Let us denote the propagation matrix between two interfaces z_k and z_{i+k} as $\mathbb{P}(z_j, z_{j+1})$. According to the equation (2.36), it is given by the following expression

$$\mathbb{P}(z_j, z_{j+1}) = \begin{pmatrix} e^{ik_z d_j} & 0 \\ 0 & e^{-ik_z d_j} \end{pmatrix}, \tag{2.50}$$

where k_z is the z-projection of the forward-traveling plane wave in j-th layer. An interface matrix of the z_k-interface is given by

$$\mathbb{I}(z_j) = \frac{1}{t_j} \begin{pmatrix} 1 & r_j \\ r_j & 1 \end{pmatrix}, \tag{2.51}$$

where r_j and t_j are the Fresnel coefficients for the z_j-interface and can be found by equations (2.48) and (2.49)[1].

Therefore, the total transfer matrix for whole structure can be expressed as:

$$\mathbb{T} = \mathbb{I}(z_0)\mathbb{P}(z_0, z_1)\mathbb{I}(z_1)\mathbb{P}(z_1, z_2)\mathbb{I}(z_2)\ldots\mathbb{I}(z_{N-1})\mathbb{P}(z_{N-1}, z_N)\mathbb{I}(z_N). \tag{2.52}$$

2.1.1.7 Reflection, transmission and absorption coefficients

Let us consider an incident forward-traveling plane wave with amplitude $E^o(z)$ $(z<0)$. Interaction of this wave with the layered structure leads to appearance of the reflected and transmitted plane waves with amplitudes $E^-(z_0-0)$ $(z<z_0)$ and $E^+(z_N+0)$ $(z>z_N)$.

[1]Note that in order to find r_j and t_j by equations (2.48) and (2.49) one have to do the following changes: $\tilde{\varepsilon}_1 \to \tilde{\varepsilon}_j$, $\tilde{\varepsilon}_2 \to \tilde{\varepsilon}_{j+1}$, $k_z' \to k_z^{(j)}$, $k_z'' \to k_z^{(j+1)}$.

We define a *reflection coefficient* as a ratio of the z-component of Pointing vector of the reflected wave to that of the incident wave:

$$R = -\frac{S_z^r}{S_z^{in}}. \tag{2.53}$$

The *transmission coefficient* is a ratio of the z-component of Pointing vector of the transmitted wave to that of the incident wave:

$$T = -\frac{S_z^t}{S_z^{in}}. \tag{2.54}$$

From equations (2.9)–(2.12), (2.53), (2.54) we can obtain the reflection and transmission coefficients:

$$R = \frac{|E_{\parallel}^-(z_0 - 0)|^2 + |E_{\perp}^-(z_0 - 0)|^2}{|E_0|^2}, \tag{2.55}$$

$$T = \frac{\mu_{01}}{\mu_{02}} \cdot \frac{Re(k_z(z_N + 0))}{Re(k_z(z_0 - 0))} \cdot \frac{|E_{\parallel}^+(z_N + 0)|^2 + |E_{\perp}^+(z_N + 0)|^2}{|E_0|^2}. \tag{2.56}$$

The *absorption coefficient* is defined is a portion of energy of the incident light which is absorbed by the substances of the layered structure and can be found from the expression

$$A = 1 - R - T. \tag{2.57}$$

It is assumed that the amplitude of incidence plane wave at $z = \lim_{\varepsilon \to 0}(-\varepsilon) = z_0 - 0$ is known and equals to E_0, whereas the amplitudes of reflected and transmitted plane waves are unknown. We can use the total transfer matrix and calculate these amplitudes and, therefore, calculate the reflection, transmission and absorption coefficients of the given layered structure.

In terms of transfer matrix the interaction of the incidence plane wave with a layered structure can be written as

$$\begin{bmatrix} E_0 \\ E^-(z_0 - 0) \end{bmatrix} = \mathbb{T} \begin{bmatrix} E^+(z_N + 0) \\ 0 \end{bmatrix}, \tag{2.58}$$

where $\mathcal{E}_0$ is the amplitude of the incident wave and is equal to 1. Zero component in the vector of amplitudes in equation (2.58) reflects the fact that there is no backward traveling wave in lower semi-infinite medium and it cannot be

created by incident wave from the upper semi-infinite medium. Equation (2.58) leads to the following relation between the amplitudes of incident, reflected and transmitted waves:

$$E_0 = T_{11}E^+(z_N + 0) \tag{2.59}$$

$$E^-(z_0 - 0) = T_{21}E^+(z_N + 0). \tag{2.60}$$

Thus,

$$E^+(z_N + 0) = \frac{1}{T_{11}}\mathcal{E}_0 \tag{2.61}$$

$$E^-(z_0 - 0) = \frac{T_{21}}{T_{11}}\mathcal{E}_0. \tag{2.62}$$

Using equations (2.53), (2.61) we obtain the following expression for reflection coefficient:

$$\boxed{R = \left|\frac{T_{21}^{\parallel}}{T_{11}^{\parallel}}\right|^2 \sin^2\theta + \left|\frac{T_{21}^{\perp}}{T_{11}^{\perp}}\right|^2 \cos^2\theta} \tag{2.63}$$

where $T_{21}^{\parallel}$ and $T_{11}^{\parallel}$ are elements of the transfer matrix $\mathbb{T}^{\parallel}$ for parallel component of the fields, while $T_{21}^{\perp}$ and $T_{11}^{\perp}$ are for perpendicular component.

Comparison between equations (2.54) and (2.62) leads to expression for transmission coefficient:

$$\boxed{T = \frac{\mu_{01}}{\mu_{02}} \cdot \frac{Re(k_z(z_N + 0))}{Re(k_z(z_0 - 0))} \cdot \left[\left|\frac{1}{T_{11}^{\parallel}}\right|^2 \sin^2\theta + \left|\frac{1}{T_{11}^{\perp}}\right|^2 \cos^2\theta\right]} \tag{2.64}$$

Thus, the knowledge of the total transfer matrix of the layered structure enables us to find the reflection, transmission and absorption coefficients.

2.1.1.8 Distribution of the electromagnetic field

Let us consider a linearly polarized plane electromagnetic wave with an amplitude E_0, a wave vector $\vec{k}$ and angle of polarization θ. This wave is incident on the layered structure. We are now going to calculate the x-, y- and z-components of

electrical and magnetic fields at coordinate $z = h$, $z_k < h < z_{k+1}$. The transfer matrix between coordinates $z_0 - 0$ and h is

$$\mathbb{T}_h \equiv \mathbb{T}(z_0 - 0, h) = \mathbb{I}(z_0)\mathbb{P}(z_0, z_1)\mathbb{I}(z_1)\mathbb{P}(z_1, z_2)\mathbb{I}(z_2)\ldots\mathbb{I}(z_k)\mathbb{P}(z_k, h). \tag{2.65}$$

According to the definition of the transfer matrix $\mathbb{T}_h$,

$$\begin{bmatrix} \mathcal{E}_0 \\ E^-(z_0 - 0) \end{bmatrix} = \mathbb{T}_h \begin{bmatrix} E^+(h) \\ E^-(h) \end{bmatrix}, \tag{2.66}$$

where $\mathcal{E}_0 \equiv E^+(z_0 - 0)$ is the known amplitude of the incident plane wave. Then

$$\begin{bmatrix} \mathcal{E}_0 \\ E^-(z_0 - 0) \end{bmatrix} = \mathbb{T} \begin{bmatrix} E^+(z_N + 0) \\ 0 \end{bmatrix}, \tag{2.67}$$

where $\mathbb{T}$ is the total transfer matrix of the structure. Zero component in the vector of amplitudes in the right side of the equation (2.67) means that there is no wave incident on the sample from the bottom semi-infinite medium. Equation (2.67) also means that

$$\mathcal{E}_0 = T_{11}E^+(z_N + 0) \tag{2.68}$$

$$E^-(z_0 - 0) = T_{21}E^+(z_N + 0), \tag{2.69}$$

and, therefore,

$$E^-(z_0 - 0) = \frac{T_{21}}{T_{11}}\mathcal{E}_0. \tag{2.70}$$

From equations (2.66), (2.70) it follows that

$$\mathcal{E}_0 \begin{bmatrix} 1 \\ \dfrac{T_{21}}{T_{11}} \end{bmatrix} = \mathbb{T}_h \begin{bmatrix} E^+(h) \\ E^-(h) \end{bmatrix}, \tag{2.71}$$

and thus,

$$\boxed{\begin{bmatrix} E^+(h) \\ E^-(h) \end{bmatrix} = \mathcal{E}_0\mathbb{T}_h^{-1} \cdot \frac{1}{T_{11}} \begin{bmatrix} T_{11} \\ T_{21} \end{bmatrix}}. \tag{2.72}$$

Formulas (2.65)–(2.72) are valid for both parallel and perpendicular components of electric field.

We calculated amplitudes of the electric field at h-coordinate for forward- and backward traveling plane waves by means of the transfer matrix. Using equations (2.23) and (2.24) we can determine the total amplitudes of the parallel and perpendicular components of the electric field. Then using equations (2.10) and (2.12) we can obtain the time average electric and magnetic energy densities and the time average Pointing vector at any (x, z)-coordinate.

2.1.2 Calculation of active optical response

In addition to calculation of the reflection, transmission and absorption coefficients, the evaluation of other optical characteristics of the stratified structure such as the intensity of photoluminescence (PL) and Raman scattering is of interest too.

Irrespective to the origin of the photoluminescence and the Raman scattering, the PL or Raman light can be out-coupled from the sample or loosen by different loss mechanisms [15, 16, 16, 17, 18, 19]. Among the loss mechanisms there are an absorption by the substrate or other layers, a coupling to the wave-guided or leaky modes [20, 21, 22], a Rayleigh scattering on the local inhomogenieties of the spatial distribution of the refractive index [23]. Despite the fact that the photoluminescence and the Raman scattering are the quantum mechanical processes, the contribution of all of these mechanisms can be described in terms of the classical electromagnetism.

In the oscillating dipole approach, the intensity of PL or Raman scattering is approximated by the intensity of the system of oscillating electrical dipoles placed in the active layer.

2.1.2.1 System oscillating electrical dipoles

In order to calculate the intensity of out-coupled dipole emission, let us consider a system of dipoles located at the plane at z'-coordinate. In [15] it was shown that it makes sense to consider two systems of dipoles, namely vertical dipoles and horizontal dipoles the dipole moment of which is chaotically oriented in xy-plane. The angular radiation pattern for vertical dipoles is defined by the following

expression:

$$\left(\frac{dI}{d\Omega}\right)_Z^p = \frac{3}{8\pi}\sin^2\psi \tag{2.73}$$

Due to the axial symmetry, the radiation of the vertical dipole is purely p-polarized. The angular radiation pattern for vertical dipole is shown in Fig. 2.3. The radiation of the system of horizontal chaotically oriented dipoles has both s- and p-components. The angular radiation pattern is defined by the following expressions:

$$\left(\frac{dI}{d\Omega}\right)_{XY}^p = \frac{3}{16\pi}\cos^2\psi \tag{2.74}$$

$$\left(\frac{dI}{d\Omega}\right)_{XY}^s = \frac{3}{16\pi}. \tag{2.75}$$

Electromagnetic field of an oscillating dipole is a wave with a complex wave front profile. For the calculation of the intensity of light, emitted by dipoles and emerged from the sample, one have to approximate the radiation of dipoles by the plane waves, which amplitude depends on the direction of their propagation. As follows from the equations (2.75), (2.74) and (2.73), the amplitudes of the

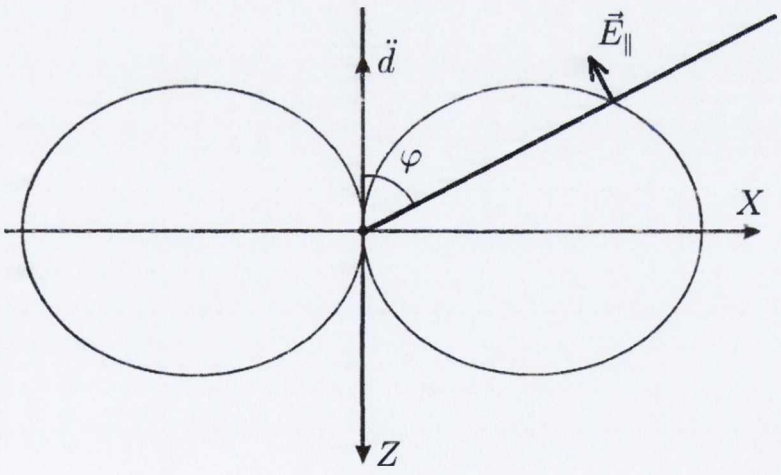

Figure 2.3: The angular radiation pattern for vertical point oscillating electrical dipole.

plane waves corresponding for the vertical dipoles are

$$A_s = 0, \quad A_p = A_0\sqrt{\frac{3}{8\pi}}\sin\psi, \tag{2.76}$$

and for the horizontal chaotically oriented dipoles

$$A_s = A_0\sqrt{\frac{3}{16\pi}}, \quad A_p = A_0\sqrt{\frac{3}{16\pi}}\cos\psi. \tag{2.77}$$

The propagation of the plane waves with given amplitudes both inside and outside the layered structure is fully described by the transfer matrix method.

2.1.2.2 Change of the vector of amplitude at the radiating plane

It can be shown [15] that the boundary conditions for the electric and magnetic fields in case of the plane of electric currents leads to the following expression for the change of the vector of amplitudes at the radiating plane at z'-coordinate

$$\mathbf{E}(z'-0) = \mathbf{E}(z'+0) + \Delta, \tag{2.78}$$

where for vertical dipoles

$$\Delta = A_p \begin{bmatrix} -1 \\ 1 \end{bmatrix}, \tag{2.79}$$

and for horizontal chaotically oriented dipoles

$$\Delta = A_s \begin{bmatrix} -1 \\ 1 \end{bmatrix}, \quad \Delta = A_p \begin{bmatrix} -1 \\ -1 \end{bmatrix}. \tag{2.80}$$

Note that the amplitude parameters A_s and A_p are related to each other by equations (2.76) and (2.77). The parameter A_0 from these equations is proportional to the absolute value of the amplitude of electric field strength of excitation light at z'-coordinate:

$$A_0 = \alpha|\vec{E}_{exc}(0,0,z',0)|. \tag{2.81}$$

The proportionality factor α can be chosen to be equal to 1.

2.1.2.3 Out-coupling of the emitted light from the sample

In calculating the intensity of out-coupled dipole radiation, we assume that the only source of the electromagnetic waves in the layered structure is the plane of oscillating dipoles. Thus, the amplitudes of the plane waves, incident on the sample from top and bottom semi-infinite media, are zero. Therefore, the vectors of amplitudes at $z = 0 - 0$ and $z = h + 0$ ($h = z_N$) have the following forms:

$$\mathbf{E}(0-0) = \begin{bmatrix} 0 \\ E^-(0-0) \end{bmatrix}, \quad \mathbf{E}(z_N+0) = \begin{bmatrix} E^+(h+0) \\ 0 \end{bmatrix}. \tag{2.82}$$

For calculation the amplitudes of forward- and backward-traveling plane waves $E^+(h+0)$ and $E^-(0-0)$, emitted by oscillating dipoles and emerged from the sample, we have to solve the following system of linear algebraic equations:

$$\begin{cases} \mathbf{E}(0-0) = \mathbb{A}\mathbf{E}(z'-0) \\ \mathbf{E}(z'-0) = \mathbf{E}(z'+0) + \Delta \\ \mathbf{E}(z'+0) = \mathbb{B}\mathbf{E}(h+0). \end{cases} \tag{2.83}$$

In the set of equations (2.83) the first equation is the relation between vectors of amplitudes at $z = 0 - 0$ and $z = z' - 0$. This relation is established by the use of the transfer matrix $\mathbb{A}$. The second equation describes the change of the vector of amplitudes at the plane of oscillating dipoles with coordinate z'. The last equation is the relation between the vectors of amplitudes at $z = z' + 0$ and $z = h$. From the set (2.83) it follows that the amplitude of the plane wave emitted by the z'-plane of oscillating dipoles and out-coupled from the sample towards the negative z-direction is defined as

$$E^-(0-0) = (\mathbb{A}\Delta)_2 - (\mathbb{A}\Delta)_1 \cdot \frac{(\mathbb{A}\mathbb{B})_{21}}{(\mathbb{A}\mathbb{B})_{11}}, \tag{2.84}$$

where the symbol X_{ij} denotes the ij-th element of a matrix X.

The expression (2.84) determines the amplitude of the out-coupled plane wave emitted by one plane of oscillating dipoles at the specified angle of observation ψ_{obs} which is related to the angle of emission in the active layer, ψ, by the Snell's law:

$$\tilde{n}_{01} \sin \psi_{obs} = \tilde{n}_j \sin \psi. \tag{2.85}$$

Note that the angle of emission ψ is needed for calculation of the transfer matrices $\mathbb{A}$ and $\mathbb{B}$[1].

2.1.2.4 Total intensity of out-coupled light

We define the *angular density of intensity* of out-coupled light emitted by a plane(s) of oscillating dipoles as a power of out-coupled light, dP, per unit solid angle, $d\Omega$ and unit sample surface $d\sigma$. In calculating the total intensity of out-coupled light, we have to account for the change in unit solid angle that is due to refraction of plane waves or its analog for evanescent waves (see Fig. 2.4a). It can be shown [15], that the defined angular density of intensity Π_i from i-th plane of oscillating dipoles, located in the j-th layer, can be found from the following expression:

$$\Pi_i \equiv \frac{dP}{d\Omega d\sigma} = |E_i^-(0-0)|^2 \cdot \frac{\tilde{n}_{01} k_{z,01}^2}{\tilde{n}_j k_{z,j}^2}, \tag{2.86}$$

where $k_{z,01}$ and $k_{z,j}$ are z-components of the wave vector of emitted light in the top semi-infinite medium and in the j-th layer, respectively. The first term in equation (2.86) is the square of amplitude of electric field of the plane wave emitted by i-th plane of the oscillating dipoles and out-coupled from the sample. This can be found from expression (2.84). The second term in equation (2.86) is the refraction refinement.

Integration of the angular density of intensity of out-coupled light over the entire range of angles of observation yields the total power emitted by the unit square surface to the top semi-infinite medium:

$$P_i = 2\pi \int_0^{\pi/2} \Pi(\psi_{obs}) \sin\psi_{obs} d\psi_{obs}. \tag{2.87}$$

Integration of the angular density of intensity of out-coupled light over the range of angles of observation $[0; \psi_1]$ gives the power collected by the lens (see Fig. 2.4b). The maximum angle ψ_1 is determined by the diameter of the lens and the distance between sample and the lens.

[1] In general, the direction of observation is characterized by two angles. For the structure under consideration, all layers are assumed to be homogeneous along x- and y-axis. It enables us to characterize the direction of observation only by the angle ψ_{obs} between the direction of emitted light propagation in the top semi-infinite medium and the negative direction of z-axis.

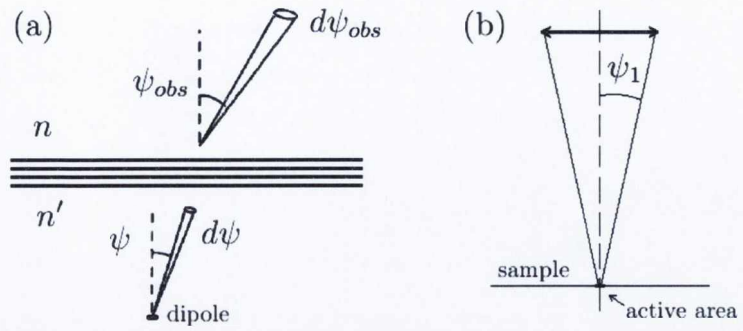

Figure 2.4: (a): Differential solid angle transfer from one layer to another [15]. (b) Collection of the outside power by the lens.

In order to simulate the total power of PL or Raman scattering from one or several active layers we have to place M equidistant planes of oscillating dipoles to the active layer(s), calculate the amplitudes of the out-coupled waves emitted by these planes, $E_i^-(0-0)$ $(i = 1, 2, \ldots, M)$ at all angles of observation in the desired range, integrate the angular density of intensity, and, finally, sum the squares of the obtained powers

$$P = \sum_{i=1}^{M} P_i. \tag{2.88}$$

The number of the emitting planes, M, depends on the thickness of active layer, the refractive index of active layer n_k and the wavelength of dipole emission, λ. The number M must be chosen in such a way that the distance between two nearest planes Δz satisfies the following relation: $n_k \Delta z \ll \lambda$.

Equation (2.88) describes the outside power emitted by either vertically or horizontally oriented dipoles. It can be shown [15] that for isotropic system of dipoles, the extracted power is defined by the following expression

$$P_{iso} = \frac{1}{3} P_{ver} + \frac{2}{3} P_{hor}. \tag{2.89}$$

2.1.3 Algorithm for numerical realization

2.1.3.1 Calculation of optical coefficients

Let us formulate the main steps of the numerical calculation of optical coefficients:

1. Represent the structure as the appropriate system of isotropic homogeneous layers, with their complex dielectric permittivities $\tilde{\varepsilon}_j$, magnetic permeabilities $\tilde{\mu}_j$ and thicknesses d_k.

2. Calculate for each layer components of the wave vector k_x and k_z using formula (2.15).

3. For each interface calculate the coefficients r_j and t_j using formulas (2.48) and (2.49) for both perpendicular and parallel components of electric field vector[1].

4. For each interface calculate the interface matrix using equation (2.51) for both perpendicular and parallel components of electric field vector.

5. For each layer calculate the propagation matrix using equation (2.50) for both perpendicular and parallel components of electric field vector.

6. Calculate the total transfer matrix of the structure using equation (2.52) for both perpendicular and parallel components of electric field vector.

7. Calculate reflection, transmission and absorption coefficient of the investigated structure from expressions (2.63) and (2.64).

2.1.3.2 Calculation of electromagnetic field distribution

For numerical calculations of the electric and magnetic field distributions the following step must be followed:

1. Execute steps 1–6 from the section 2.1.3.1.

2. For each layer calculate the coordinates of the vectors $\vec{s}_\pm$ and $\vec{p}_\pm$ by means of the equation (2.22).

[1]Note that if the angle of polarization $\theta = 0$ or $\theta = \pi/2$ (that corresponds to p- or s-polarization respectively) then only perpendicular or parallel component is required.

3. Calculate the propagation matrices $\mathbb{P}(z_j, h)$ for both components of electric field vector and for all required h-coordinates with equation:

$$\mathbf{P}(z_j, h) = \begin{bmatrix} e^{ik_z(h-z_j)} & 0 \\ 0 & e^{-ik_z(h-z_j)} \end{bmatrix}; \tag{2.90}$$

4. Calculate the transfer matrices $\mathbb{T}_h$ for all required h-coordinates by equation (2.65) for both components of electric field vector.

5. Calculate the amplitudes of the electric field for both components of electric field vector by means of equation (2.72) using the total transfer matrix and the matrices $\mathbb{T}_h$.

6. Calculate x-, y-, z-components of the electric and magnetic fields by equations (2.23)–(2.28), and the time-averaged electric and magnetic energy densities and the time average Pointing vector at any (x, h)-coordinate by formulas (2.10)–(2.12).

2.1.3.3 Calculation of intensity of photoluminescence or Raman scattering

Calculation of the intensity of photoluminescence and of Raman scattering for desired polarization of emission and orientation of oscillating dipoles includes the following steps:

1. Represent the active layers as a system of parallel planes of oscillating dipoles. If the active layer is thin enough, then only one plane can be considered.

2. Calculate the electric field strength at the z-coordinates of the planes of oscillating dipoles.

3. Calculate the change of vector of amplitudes, Δ, by formulas (2.76), (2.77), (2.79), (2.80) and (2.81) for desired range of angles of observation and for all plane of dipoles.

4. Calculate the transfer matrices $\mathbb{A}$ and $\mathbb{B}$ for desired range of angles of observation and for all plane of dipoles.

5. Calculate the amplitude of backward traveling plane wave $E^{-}(0-0)$ using formula (2.84) for desired range of the angles of observation and for all planes of dipoles.

6. Calculate the angular density of out-coupled light using formula (2.86) for desired range of angles of observation for all planes of dipoles.

7. Integrate the angular density of intensity over the desired range of angles of observation using formula (2.87) for all plane of dipoles.

8. Sum the outside emitted powers calculated for all plane of dipoles.

9. The extracted power emitted by isotropic system of dipoles can be found from formula (2.89).

2.2 Scattering matrix method

In this chapter the *scattering matrix method* is considered. The scattering matrix method is a powerful tool for description of propagation of electromagnetic waves in a layered structure, one or several layers of which is periodical in x- and/or y-directions [8, 9]. Examples of these structures are shown in Fig. 2.5.

2.2.1 Mathematical problem of scattering matrix method

Mathematical problem of the scattering matrix method includes calculation of the transmission, reflection, absorption and diffraction coefficients for a given spatial distribution of the dielectric permittivity $\varepsilon(x, y, z)$ of the investigated structure and a given polarization and wave vector of the incident light $\vec{k}_0 \equiv \{k_x, k_y, k_z\}$, where

$$k_x = \frac{\omega}{c} \sin\vartheta \cos\varphi,\ k_y = \frac{\omega}{c} \sin\vartheta \sin\varphi, \tag{2.91}$$

$$k_z = \frac{\omega}{c} \cos\vartheta, \tag{2.92}$$

ω is a frequency of the incident light, c is the speed of light, φ and θ are the angles between the wave vector $\vec{k}_0$ and x- and z-axis, correspondingly.

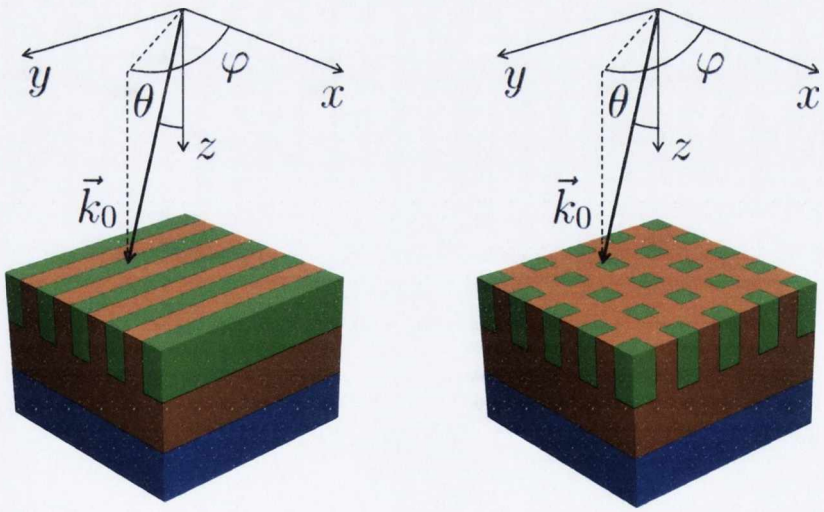

Figure 2.5: Schematics of (a) one-dimensional and (b) two-dimensional photonic crystal structures.

2.2.2 Maxwell's equations in periodical layers

The propagation of the electromagnetic waves in medium is described by Maxwell's equations:

$$\nabla \times \vec{H} - \frac{1}{c}\frac{\partial \vec{D}}{\partial t} = \frac{4\pi}{c}\vec{j} \tag{2.93}$$

$$\nabla \times \vec{E} + \frac{1}{c}\frac{\partial \vec{B}}{\partial t} = 0 \tag{2.94}$$

$$\nabla \vec{B} = 0 \tag{2.95}$$

$$\nabla \vec{D} = 4\pi\rho. \tag{2.96}$$

In the approximation of a linear medium ($\vec{D} = \varepsilon\vec{E}$, $\vec{B} = \mu\vec{H}$), taking into account the relation between the magnetic field $\vec{H}$ and the magnetic induction $\vec{B}$ and between the electric field $\vec{E}$ and the electric displacement vector $\vec{D}$, taking into account the fact that in this system there are no currents ($\vec{j} = 0$) and free charges ($\rho = 0$), as well as taking into account the fact that the time t is included in the expressions for these vectors in the form $e^{i\omega t}$, we obtain the following system of equations:

$$\nabla \times \vec{E} = ik_0\mu\vec{H} \tag{2.97}$$

$$\nabla \times \vec{H} = -ik_0\mu\vec{E}. \tag{2.98}$$

Expanding the equations (2.97) and (2.98) in x-, y-, z-components we obtain:

$$\frac{\partial}{\partial y}E_z - \frac{\partial}{\partial z}E_y = ik_0\mu H_x \tag{2.99}$$

$$\frac{\partial}{\partial z}E_x - \frac{\partial}{\partial x}E_z = ik_0\mu H_y \tag{2.100}$$

$$\frac{\partial}{\partial x}E_y - \frac{\partial}{\partial y}E_x = ik_0\mu H_z. \tag{2.101}$$

$$\frac{\partial}{\partial y}H_z - \frac{\partial}{\partial z}H_y = ik_0\varepsilon E_x \tag{2.102}$$

$$\frac{\partial}{\partial z}H_x - \frac{\partial}{\partial x}H_z = ik_0\varepsilon E_y \tag{2.103}$$

$$\frac{\partial}{\partial x}H_y - \frac{\partial}{\partial y}H_x = ik_0\varepsilon E_z. \tag{2.104}$$

This six equations as well as six boundary conditions determine three field components $\vec{E}(x,y,z)$ and $\vec{H}(x,y,z)$.

Let us consider the case when the dielectric permittivity does not depend on z. In view of this feature it is convenient to exclude z-components of the vectors $\vec{E}$ and $\vec{H}$ from the equations (2.99–2.104). Substitution the equation (2.104) into the equations (2.99) and (2.100) leads to the following set of equations:

$$-ik_0\frac{\partial}{\partial z}E_y = \left(-\frac{\partial}{\partial y}\frac{1}{\varepsilon}\frac{\partial}{\partial y} - k_0^2\mu\right)H_x + \frac{\partial}{\partial y}\frac{1}{\varepsilon}\frac{\partial}{\partial x}H_y \tag{2.105}$$

$$-ik_0\frac{\partial}{\partial z}E_x = -\frac{\partial}{\partial x}\frac{1}{\varepsilon}\frac{\partial}{\partial y}H_x + \left(-\frac{\partial}{\partial x}\frac{1}{\varepsilon}\frac{\partial}{\partial x} + k_0^2\mu\right)H_y. \tag{2.106}$$

The set of equations (2.105, 2.106) can be written in the matrix form:

$$-ik_0\frac{\partial}{\partial z}\begin{pmatrix}E_x\\E_y\end{pmatrix} = M\begin{pmatrix}H_x\\H_y\end{pmatrix}, \tag{2.107}$$

where

$$M \equiv \begin{pmatrix}-\frac{\partial}{\partial x}\frac{1}{\varepsilon}\frac{\partial}{\partial y} & \frac{\partial}{\partial x}\frac{1}{\varepsilon}\frac{\partial}{\partial x} + k_0^2\mu\\ -\frac{\partial}{\partial y}\frac{1}{\varepsilon}\frac{\partial}{\partial y} - k_0^2\mu & \frac{\partial}{\partial y}\frac{1}{\varepsilon}\frac{\partial}{\partial x}\end{pmatrix}. \tag{2.108}$$

Similarly for the set (2.102–2.104) we obtain:

$$-ik_0\frac{\partial}{\partial z}\begin{pmatrix}H_x\\H_y\end{pmatrix} = N\begin{pmatrix}E_x\\E_y\end{pmatrix}, \tag{2.109}$$

where

$$N \equiv \begin{pmatrix}\frac{\partial^2}{\partial x\partial y} & -\frac{\partial^2}{\partial x^2} - k_0^2\mu\varepsilon\\ \frac{\partial^2}{\partial y^2} + k_0^2\mu\varepsilon & -\frac{\partial^2}{\partial y\partial x}\end{pmatrix}. \tag{2.110}$$

From equations (2.107) and (2.109) it follows that

$$-k_0^2\mu\frac{\partial^2}{\partial z^2}\begin{pmatrix}E_x\\E_y\end{pmatrix} = MN\begin{pmatrix}E_x\\E_y\end{pmatrix}. \tag{2.111}$$

The dielectric permittivity of each layer is a periodical function of x and y and, therefore, the electric field as a solution of the set (2.111) can be found as the sum of the plane waves:

$$\vec{E}(x,y,z) = \sum_{G_x}\sum_{G_y}\vec{\mathrm{E}}_{G_x,G_y}\exp\left[i(k_x+G_x)+i(k_y+G_y)\right]\times\exp(iKz), \tag{2.112}$$

where $K \equiv k_z$, $G_x = \frac{2\pi}{L_x} g_x$, $G_y = \frac{2\pi}{L_y} g_y$, $g_{x,y} = 0, \pm 1, \pm 2, \ldots$, where the reciprocal lattice vector is written for the case of rectangular symmetry and L_x and L_y - are the periods of the function $\varepsilon(x, y, z)$ along x- and y-directions. The dielectric permittivity can be expanded in the following Fourier series:

$$\varepsilon_{\vec{G}\vec{G}'} = \frac{1}{S} \int \varepsilon(\vec{r}) \exp(-i(\vec{G} - \vec{G}')\vec{r}) dx dy, \tag{2.113}$$

where $S = (4\pi^2)/(L_x L_y)$ is the square of elementary cell in reciprocal space. Now the expression (2.111) can be rewritten taking into account the Fourier expansions of $\varepsilon(x, y, z)$ and the vector $\vec{E}(x, y, z)$:

$$-k_0^2 \frac{\partial^2}{\partial z^2} \begin{pmatrix} \mathrm{E}_x \\ \mathrm{E}_y \end{pmatrix} = \mathcal{M}\mathcal{N} \begin{pmatrix} \mathrm{E}_x \\ \mathrm{E}_y \end{pmatrix}. \tag{2.114}$$

In expression (2.114), the matrices $\mathcal{M}$ and $\mathcal{N}$ are

$$\mathcal{M} = \begin{pmatrix} \mathrm{d}_x \left[\frac{1}{\varepsilon}\right]_{\vec{G}\vec{G}'} \mathrm{d}_y & -\mathrm{d}_x \left[\frac{1}{\varepsilon}\right]_{\vec{G}\vec{G}'} \mathrm{d}_x + k_0^2 \\ \mathrm{d}_y \left[\frac{1}{\varepsilon}\right]_{\vec{G}\vec{G}'} \mathrm{d}_y - k_0^2 & -\mathrm{d}_y \left[\frac{1}{\varepsilon}\right]_{\vec{G}\vec{G}'} \mathrm{d}_x \end{pmatrix} \tag{2.115}$$

$$\mathcal{N} = \begin{pmatrix} -\mathrm{d}_x \mathrm{d}_y & \mathrm{d}_x^2 - k_0^2 [\varepsilon]_{\vec{G}\vec{G}'} \\ -\mathrm{d}_y^2 + k_0^2 [\varepsilon]_{\vec{G}\vec{G}'} & \mathrm{d}_x \mathrm{d}_y \end{pmatrix}, \tag{2.116}$$

where d_x and d_y are the diagonal matrices with elements $i(k_x + G_x)$ and $i(k_y + G_y)$ correspondingly, $[\varepsilon]_{\vec{G}\vec{G}'}$ and $\left[\frac{1}{\varepsilon}\right]_{\vec{G}\vec{G}'}$ are the matrices, which elements are the Fourier coefficients of the functions $\varepsilon(\vec{r})$ and $\frac{1}{\varepsilon(\vec{r})}$, correspondingly, E_x and E_y are the vectors with elements $E_{x,G}$ and $E_{y,G}$, correspondingly.

Equation (2.114) represents the mathematical problem of finding the eigenvalues of operator $\mathcal{M}\mathcal{N}$ along the z-direction and the corresponding eigenvectors. Accordingly to (2.112), the z-dependence of each eigenvector is defined by the eigenvalue K^2 as $e^{\pm iKz}$. Hence, the eigen problem (2.114) is equivalent to the following one:

$$k_0^2 K^2 \begin{pmatrix} \mathrm{E}_x \\ \mathrm{E}_y \end{pmatrix} = \mathcal{M}\mathcal{N} \begin{pmatrix} \mathrm{E}_x \\ \mathrm{E}_y \end{pmatrix}. \tag{2.117}$$

Vectors and matrices in the eigen problem (2.117) are infinite-dimensional, however in the numerical calculation only the first N_G harmonics around zero and the zeroth order are accounted for. Then, the dimensionality of equation (2.117)

depends on the truncation order N_G. E_x and E_y have the length N_G, $\mathcal{M}$ and $\mathcal{N}$ are $2N_G \times 2N_G$-matrices and, therefore, we can use the numerical tools of linear algebra for eigenvalues and eigenvectors.

Let us represent the field distribution in the investigated structure as a linear combination of eigenfunctions of the matrix $\mathcal{MN}$. Given the fact that the z-dependence is included in the eigenvectors in the form $e^{\pm iKz}$, this linear combination is as follows:

$$\begin{pmatrix} \mathrm{E}_x \\ \mathrm{E}_y \end{pmatrix}^{\pm} = \mathcal{E} \exp(\pm i\mathcal{K}z)\vec{\mathcal{A}}^{\pm}, \tag{2.118}$$

where the matrix $\mathcal{E}$ consists of the eigen vectors of the propagation operator $\mathcal{MN}$:

$$\mathcal{E} \equiv \left[\begin{pmatrix} \mathrm{E}_x \\ \mathrm{E}_y \end{pmatrix}_1 \begin{pmatrix} \mathrm{E}_x \\ \mathrm{E}_y \end{pmatrix}_2 \cdots \begin{pmatrix} \mathrm{E}_x \\ \mathrm{E}_y \end{pmatrix}_{2N_G} \right], \tag{2.119}$$

the matrix $\mathcal{K}$ is the diagonal matrix which elements are the eigenvalues of the matrix $\mathcal{MN}$:

$$\mathcal{K} \equiv \begin{bmatrix} K_1 & 0 & \cdots & 0 \\ 0 & K_2 & \cdots & 0 \\ \vdots & \vdots & \ddots & \vdots \\ 0 & 0 & \cdots & K_{2N_G} \end{bmatrix}, \tag{2.120}$$

and $2N_G$-dimensional vectors $\vec{\mathcal{A}}^{\pm}$ are the coefficients of linear combination of eigenvectors of the matrix $\mathcal{MN}$.

In general, the matrix $\mathcal{MN}$ has $2N_G$ eigenvalues. In case of homogeneous layer and in the absence of absorption, the value of K^2 can be both positive and negative. In the first case, we have two solutions propagating along positive and negative z-direction, correspondingly. In the second case, when $K^2 < 0$, the solution are either exponentially decaying or increasing along z-direction.

In order to obtain the magnetic vectors from the amplitudes, we can start with equation (2.109). For each eigenvalue K_j, the Floquet-Fourier expansion of this equation has the following form:

$$k_0 K_j \begin{pmatrix} \mathrm{H}_x \\ \mathrm{H}_y \end{pmatrix}_j = \mathcal{N} \begin{pmatrix} \mathrm{E}_x \\ \mathrm{E}_y \end{pmatrix}_j. \tag{2.121}$$

Equations (2.114) and (2.121) can be written in the form of formula which transforms a known amplitude vector $\vec{\mathcal{A}}$ into the electric and magnetic vectors:

$$\begin{pmatrix} \mathrm{E}_x \\ \mathrm{E}_y \\ \mathrm{H}_x \\ \mathrm{H}_y \end{pmatrix} = \begin{pmatrix} \mathcal{E}\exp(i\mathcal{K}z) & \mathcal{E}\exp(-i\mathcal{K}z) \\ -\frac{1}{k_0}\mathcal{N}\mathcal{E}\mathcal{K}^{-1}\exp(i\mathcal{K}z) & \frac{1}{k_0}\mathcal{N}\mathcal{E}\mathcal{K}^{-1}\exp(-i\mathcal{K}z) \end{pmatrix} \begin{pmatrix} \vec{\mathcal{A}}^{+} \\ \vec{\mathcal{A}}^{-} \end{pmatrix}, \tag{2.122}$$

or briefly

$$\mathbb{E} = \mathbb{F}\vec{\mathbb{A}}. \tag{2.123}$$

The matrix $\mathbb{F}$ is called as *material matrix*. For calculation z-components of the electric and magnetic field we can use the expressions (2.101) and (2.104):

$$E_z = -\frac{1}{k_0}\left[\frac{1}{\varepsilon}\right]_{\vec{G}\vec{G}'}(\mathrm{d}_x\mathrm{H}_y - \mathrm{d}_y\mathrm{H}_x), \tag{2.124}$$

$$H_z = \frac{1}{k_0}(\mathrm{d}_x\mathrm{E}_y - \mathrm{d}_y\mathrm{E}_x). \tag{2.125}$$

2.2.3 Scattering matrix

Solution of the eigen problem describes how the light can propagate in a given layer. In order to calculate the distribution of the electromagnetic field in the layered structure, one have to calculate the coefficients $\vec{\mathcal{A}}^{\pm}$ of linear combination (2.118) taking into account the boundary conditions for vectors $\vec{E}$ and $\vec{H}$ at the interfaces between the layers. It can be done by calculating the $4N_G \times 4N_G$-dimensional transfer matrix which relates the amplitude vectors $\vec{\mathbb{A}}$ at two different z-coordinates z_a and z_b.

$$\begin{pmatrix} \vec{\mathcal{A}}^{+} \\ \vec{\mathcal{A}}^{-} \end{pmatrix}_b = \mathbb{T}\begin{pmatrix} \vec{\mathcal{A}}^{+} \\ \vec{\mathcal{A}}^{-} \end{pmatrix}_a. \tag{2.126}$$

It can be shown that if the coordinates z_a and z_b are within the same layer then the transfer matrix has the following form

$$\mathbb{T}^{b,a} = \begin{pmatrix} \exp(i\mathcal{K}L) & 0 \\ 0 & \exp(-i\mathcal{K}L) \end{pmatrix}, \tag{2.127}$$

where $L = z_b - z_a$. In this case the transfer matrix is called as a *propagation matrix*. If the coordinates a and b are at immediately opposite sides of the interface z_0 ($z_a = z_0 - 0$ and $z_b = z_0 + 0$) then the transfer matrix is

$$\mathbb{T}^{b,a} = \mathbb{F}_b^{-1}\mathbb{F}_a. \tag{2.128}$$

In this case the transfer matrix is called as an *interface matrix*. If $\mathcal{K}$ has complex parts then, as follows from (2.127), the propagation matrix has the elements both exponentially decreasing and exponentially increasing with increase of L. This cause numerical instabilities in calculation of the propagation matrix. Small elements could be set equal to zero, while sometimes large elements reach the maximum limit of the calculation. There is no possibility of scaling the transfer matrix to avoid this problem. To avoid the described problem of mixing the large and small numbers in the same matrix, the *scattering matrix method* was developed. This method was described by D. M. Whittakker and I. S. Culshaw in 1999 [8] and by S. G. Tikhodeev and N. A. Gippius in 2002 [9]. The scattering matrix, $\mathbb{S}^{b,a}$, is defined by the following expression

$$\begin{pmatrix} \vec{A}_b^+ \\ \vec{A}_a^- \end{pmatrix} = \mathbb{S}^{b,a} \begin{pmatrix} \vec{A}_a^+ \\ \vec{A}_b^- \end{pmatrix}. \tag{2.129}$$

and has dimensionality of $4N_G \times 4N_G$ like the transfer matrix $\mathbb{T}$. The scattering matrix can be calculated by iteration procedure described in [9, 13]. The initial point of the procedure is the evident equality $\mathbb{T}^{a,a} = \mathbb{S}^{a,a} = 1$. Then, the scattering matrix $\mathbb{S}^{n+1,a}$ between coordinates z_{n+1} and z_a can be calculated from the scattering matrix $\mathbb{S}^{n,a}$ using the following expression

$$\mathbb{S}^{n+1,a} = \begin{pmatrix} \mathbb{R}\mathbb{S}_{11}^{n,a} & \mathbb{R}\mathbb{Q} \\ \mathbb{S}_{21}^{n,a} + \mathbb{S}_{22}^{n,a}\mathbb{T}_{21}^{n,n+1}\mathbb{R}\mathbb{S}_{11}^{n,a} & \mathbb{S}_{22}^{n,a}\mathbb{T}_{21}^{n,n+1}\mathbb{R}\mathbb{Q} + \mathbb{S}_{22}^{n,a}\mathbb{T}_{22}^{n,n+1} \end{pmatrix}, \tag{2.130}$$

where

$$\mathbb{Q} = \mathbb{S}_{12}^{n,a}\mathbb{T}_{22}^{n,n+1} - \mathbb{T}_{12}^{n,n+1}, \qquad \mathbb{R} = (\mathbb{T}_{11}^{n,n+1} - \mathbb{S}_{12}^{n,a}\mathbb{T}_{21}^{n,n+1})^{-1}. \tag{2.131}$$

Here we used the symbol notation $\mathbb{X}_{ij}^{m,n}$ for the $2N_G \times 2N_G$ blocks of the $4N_G \times 4N_G$ matrix $\mathbb{S}^{m,n}$

$$\mathbb{S}^{m,n} \equiv \begin{pmatrix} \mathbb{S}_{11}^{m,n} & \mathbb{S}_{12}^{m,n} \\ \mathbb{S}_{21}^{m,n} & \mathbb{S}_{22}^{m,n} \end{pmatrix}. \tag{2.132}$$

If the coordinates z_{n+1} and z_n are within the same j-th layer then the relation between matrices $\mathbb{S}^{n+1,a}$ and $\mathbb{S}^{n,a}$ can be simplified:

$$\mathbb{S}^{n+1,a} = \begin{pmatrix} \exp i\mathcal{K}_j L & 0 \\ 0 & 1 \end{pmatrix} \mathbb{S}^{n,a} \begin{pmatrix} 1 & 0 \\ 0 & \exp i\mathcal{K}_j L \end{pmatrix}. \tag{2.133}$$

As follows from the expression (2.133), there is no mixing of large and small numbers in the same matrix unlike in case of the transfer matrix. Thus, the scattering matrix can be utilized for calculation of the propagation of light through thick absorbing layers.

2.2.4 Distribution of the electromagnetic field

For calculation of field distribution in the investigated structure we have to find the $2N_G$-dimensional amplitude vectors $\vec{\mathcal{A}}_b^{\pm}$ for all required coordinates $z = z_b$ from the following expressions:

$$\vec{\mathbb{A}}(z_b) \equiv \begin{bmatrix} \vec{\mathcal{A}}_b^{+} \\ \vec{\mathcal{A}}_b^{-} \end{bmatrix} = \begin{bmatrix} \mathbb{S}_{11}^{b,a} \vec{\mathcal{A}}_a^{+} + \mathbb{S}_{12}^{b,a} \left(\mathbb{S}_{22}^{b,a}\right)^{-1} \left(\mathbb{S}_{21}^{c,a} - \mathbb{S}_{21}^{b,a}\right) \vec{\mathcal{A}}_a^{+} \\ \left(\mathbb{S}_{22}^{b,a}\right)^{-1} \left(\mathbb{S}_{21}^{c,a} - \mathbb{S}_{21}^{b,a}\right) \vec{\mathcal{A}}_a^{+} \end{bmatrix}, \tag{2.134}$$

where matrices $\mathbb{S}_{ij}^{m,n}$ are the $2N_G \times 2N_G$ blocks of the $4N_G \times 4N_G$ matrix (see (2.132)). Boundary coordinates are $z_a = 0 - 0$ and $z_c = h + 0$ where h is the

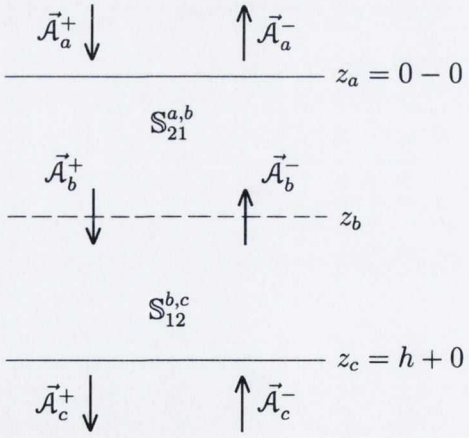

Figure 2.6: Sketch of calculation of the amplitude vectors at any given $z = z_b$ coordinate.

thickness of entire structure. Fig. 2.6 shows the sketch of the calculation of the amplitude vectors at the coordinate $z = z_b$. The scattering matrices $\mathbb{S}^{b,a}$, $\mathbb{S}^{c,a}$ can be found by the procedure described in Sec. 2.2.3. In accordance to [9], the incoming amplitude vector for s-polarization at the coordinate $z = z_a$ is:

$$\vec{\mathcal{A}}^{+}_{a,s} = \begin{bmatrix} \sin\varphi \\ 0 \\ \vdots \\ -\cos\varphi \\ 0 \\ \vdots \end{bmatrix}, \tag{2.135}$$

and for p-polarization at the coordinate $z = z_a$

$$\vec{\mathcal{A}}^{+}_{a,p} = \begin{bmatrix} \cos\varphi\cos\theta \\ 0 \\ \vdots \\ \sin\varphi\cos\theta \\ 0 \\ \vdots \end{bmatrix}. \tag{2.136}$$

Finally, the coefficients of Floquet-Fourier decomposition of electric and magnetic field vectors can be found from equation (2.123).

2.2.5 Optical coefficients

Knowledge of the total scattering matrix $\mathbb{S}^{c,a}$ of the entire system and of the input amplitude vector $\vec{\mathbb{A}}(z_a)$ allows us to calculate the reflection, transmission and absorption coefficients. The simplest way to do this is to calculate the z-projections of the Poynting vector, $\vec{S}$, for incoming, reflected, transmitted, and deflected into vacuum and substrate waves. It can be shown that

$$P \equiv S_z \equiv \mathrm{Re}\left(\frac{c}{8\pi}\left[\vec{E}\times\vec{H}^{*}\right]\right)_z = \frac{c}{8\pi}\mathrm{Re}\left(\mathrm{H}_y^{\dagger}\mathrm{E}_x - \mathrm{H}_x^{\dagger}\mathrm{E}_y\right), \tag{2.137}$$

where symbol "†" denotes the complex conjugation and transposition.

For homogeneous layers it is convenient to consider the wave propagation for each harmonic $\vec{G}$ as long as the effective wave number K represents precisely one reciprocal lattice vector $\vec{G}$:

$$\vec{k}_{\vec{G}} = \begin{pmatrix} k_x + G_x \\ k_y + G_y \\ \sqrt{\frac{\omega^2 \varepsilon_a}{c^2} - (k_x + G_x)^2 - (k_y + G_y)^2} \end{pmatrix}. \tag{2.138}$$

The direction of this vector $\vec{G}$ is a direction of the wave propagation. If $K_{\vec{G}}$ is real and the considered homogeneous layer is either substrate or incoming medium then the corresponding mode outcouples from the structure. Such modes are called as *open channels*. In opposite case, in case of imaginary $K_{\vec{G}}$ we deal with the exponentially decayed harmonic.

The main harmonic $\vec{G} = (0,0)^T$ is always an open channel. Open channels which are not a main mode are called as *diffraction channels*.

In the present work, the *reflection* and *transmission coefficients* for the main harmonic are calculated as the ratios of the respective energy fluxes:

$$R = -\frac{P^r}{P^{in}}, \qquad T = -\frac{P^t}{P^{in}}, \tag{2.139}$$

where P^{in} is the energy flux of the incident wave, P^r, P^t are the energy fluxes of the reflected and transmitted waves, calculated with formula (2.137) for the main harmonic. Minus in formula (2.139) means that the energy of the reflected light propagates in negative z-direction.

Note that the *diffraction coefficient* can be found from the following expression:

$$D = \frac{P_d^t - P_d^r}{P^{in}}, \tag{2.140}$$

where P_d^t and P_d^r are the energy fluxes of the reflected and transmitted waves calculated by equation (2.137) for all harmonic $\vec{G}$ except for the main one. An *absorption coefficient* is defined as

$$A = 1 - T - R - D. \tag{2.141}$$

2.2.6 Algorithm for numerical realization

Let us formulate the main steps in calculation of optical characteristics of the structures by the scattering matrix method:

1. Split the system into the layers homogeneous along the z-axis. Based on Maxwells equations, find the eigen modes of the operator of propagation along the z-axis (see equation (2.117).

2. For each layer construct the material matrices using equations (2.122) and (2.123) and calculate the in-plane components of the local electromagnetic fields via the amplitudes of partial waves. Propagation and interface transfer matrices need to be constructed as well (equations (2.127) and (2.128)) in order to connect the amplitudes in different parts of the structure.

3. Construct the total scattering matrix $\mathbb{S}$ of the whole structure, connecting the incoming and outgoing vector amplitudes via the iterative procedure of Ko and Inkson using equations (2.129), (2.130) and (2.131).

4. Calculate, via the components of $\mathbb{S}$ matrix, the optical properties of the system such as transmission, reflection (2.139), diffraction (2.140), absorption (2.141) and the corresponding spatial distributions of the electromagnetic fields.

Chapter 3

Surface photonic states in two-dimensional photonic crystals

3.1 Introduction

Photonic crystal is an ordered periodic array of materials with different refractive indexes. Fig. 3.1 shows three simplest cases of photonic crystals. The spatial period of the variation of the refractive index is called as *lattice constant*, as it corresponds to the usual crystal lattice constant, which represents a periodic array of atoms. Indeed, many of the basic ideas are shared for ordinary atomic crystals and photonic crystals and they can be used to construct a fundamental theory of photonic crystals, as is shown, for example, in [1]. The behavior of electrons in

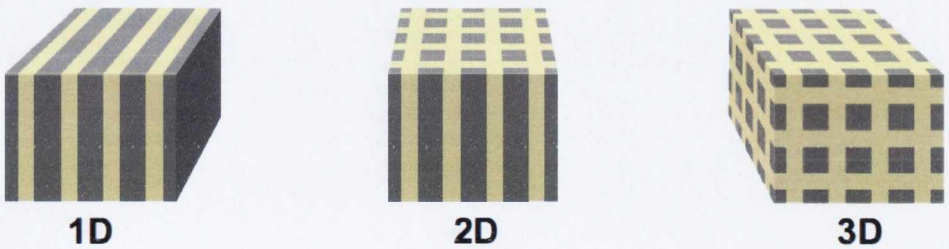

Figure 3.1: Schematic of one-, two-, and three-dimensional photonic crystals. The colors, gray and yellow, indicate different materials.

usual crystals is determined by the periodic electric potential of the atoms and, consequently, by the forbidden electronic energy bands. The propagation of light also can be described in terms of forbidden gaps which are called as *photonic band gaps*. Furthermore, if a defect is introduced to the ordered photonic crystal lattice then the *localized defect modes* can be obtained. The wave functions of these modes are localized mainly near the defect.

Let us consider a one-dimensional photonic crystal, for example, shown in Fig. 3.2. The wave equation for the electric field is:

$$\frac{c^2}{\varepsilon(x)}\frac{\partial^2 E}{\partial x^2} = \frac{\partial^2 E}{\partial t^2}, \tag{3.1}$$

where $\varepsilon(x)$ denotes the position-dependent relative dielectric constant of the one-dimensional photonic crystal, which will be called the *dielectric function* hereafter. In Eqn. (3.1), we assumed that the magnetic permeability of the photonic crystal is equal to that in free space, since we do not consider magnetic materials. Let us find a solution of the Eqn. (3.1) in the form $E(x,t) = E(x)e^{i\omega t}$. Equation (3.1) can be written as:

$$\frac{1}{\varepsilon(x)}\frac{\partial^2 E(x)}{\partial x^2} = \frac{\omega^2}{c^2}E(x). \tag{3.2}$$

The dielectric function $1/\varepsilon(x)$ is also periodic and can be expanded in a Fourier series:

$$\varepsilon^{-1}(x) = \sum_{m=-\infty}^{\infty} \epsilon_m \exp\left(i\frac{2\pi m}{a}x\right), \tag{3.3}$$

where ϵ_m are the Fourier coefficients. According to the Bloch's theorem, the Eqn. (3.2) has a solution $E(x,t)$, which is the sum of Floquet-Fourier waves:

$$E(x) = \sum_{n=-\infty}^{\infty} E_n \exp\left(\frac{-2\pi n}{a}x - ikx\right). \tag{3.4}$$

Using Eqn. (3.3), (3.4) and (3.2) one can obtain:

$$\sum_m \sum_n \left(\frac{2\pi n}{a} + k\right)^2 \epsilon_m E_n e^{-i\frac{2\pi m}{a}x - i\frac{2\pi n}{a}x - ikx} = \frac{\omega^2}{c^2}\sum_n E_n e^{-i\frac{2\pi n}{a}x - ikx}. \tag{3.5}$$

Equation (3.5) leads to

$$\sum_n \left(\frac{2\pi n}{a} + k\right)^2 \epsilon_{m-n} E_n = \frac{\omega^2}{c^2}E_m. \tag{3.6}$$

Now we have the eigenvalue problem for infinite dimensional vector E_m ($m = -\infty \ldots -1, 0, 1, \ldots, \infty$). We have to solve this problem for each desired wave vector k and find the corresponding frequencies $\omega(k)$. This enables us to plot the dispersion relations $\omega(k)$ of the eigenmodes of the one-dimensional photonic crystals characterized by a spatial function of the dielectric permittivity $\varepsilon(x)$. Since the curves $\omega(k)$ are even periodic functions with period $2\pi/a$, it is sufficient to directly solve the eigenvalue problem (3.6) only for the range of wavenumbers $[0, \pi/a]$. By analogy with the problem of a periodic potential in ordinary crystals, the segment $[-\pi/a, \pi/a]$ is called the *first Brillouin zone.*

Dispersion relations of one-dimensional photonic crystals are shown in Fig. 3.2. It is evident from Fig. 3.2 that there are the frequency ranges in which there are no eigenmodes of the considered photonic crystals. These ranges called the *photonic band gaps.* The eigenvalue problem, similar to (3.6), can be written for two-dimensional photonic crystal. In case of the photonic crystal of square

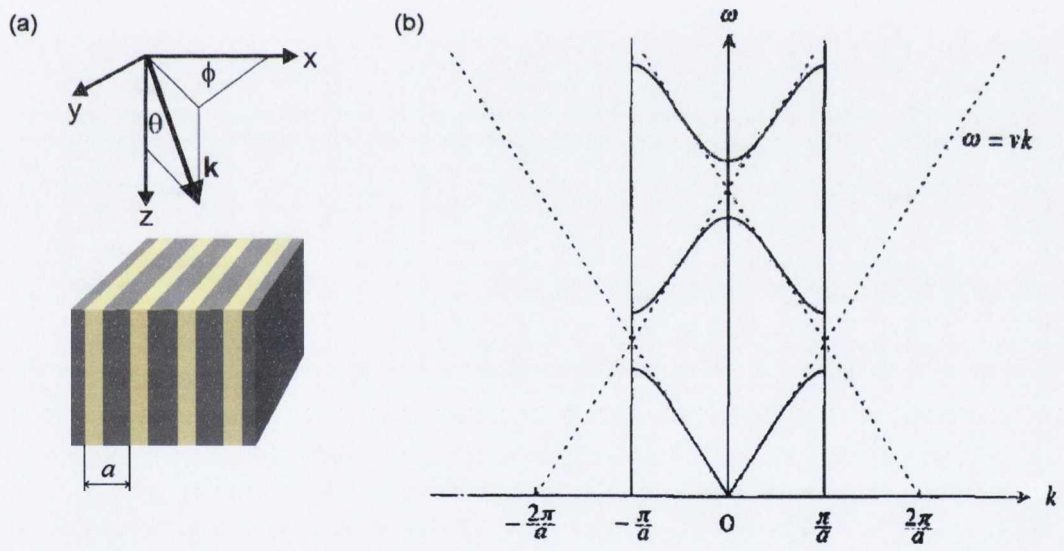

Figure 3.2: (a) Schematic picture of a one-dimensional photonic crystal. (b) Dispersion relation (solid thin line) of this structure with band gaps in the middle and at the boundaries of the first Brillouin zone. The dotted line indicates a dispersion relation in a homogeneous medium with a group velocity $\nu = c/n$. The border of the first Brillouin zone is depicted by the thick black vertical lines at $-\pi/a$ and π/a.

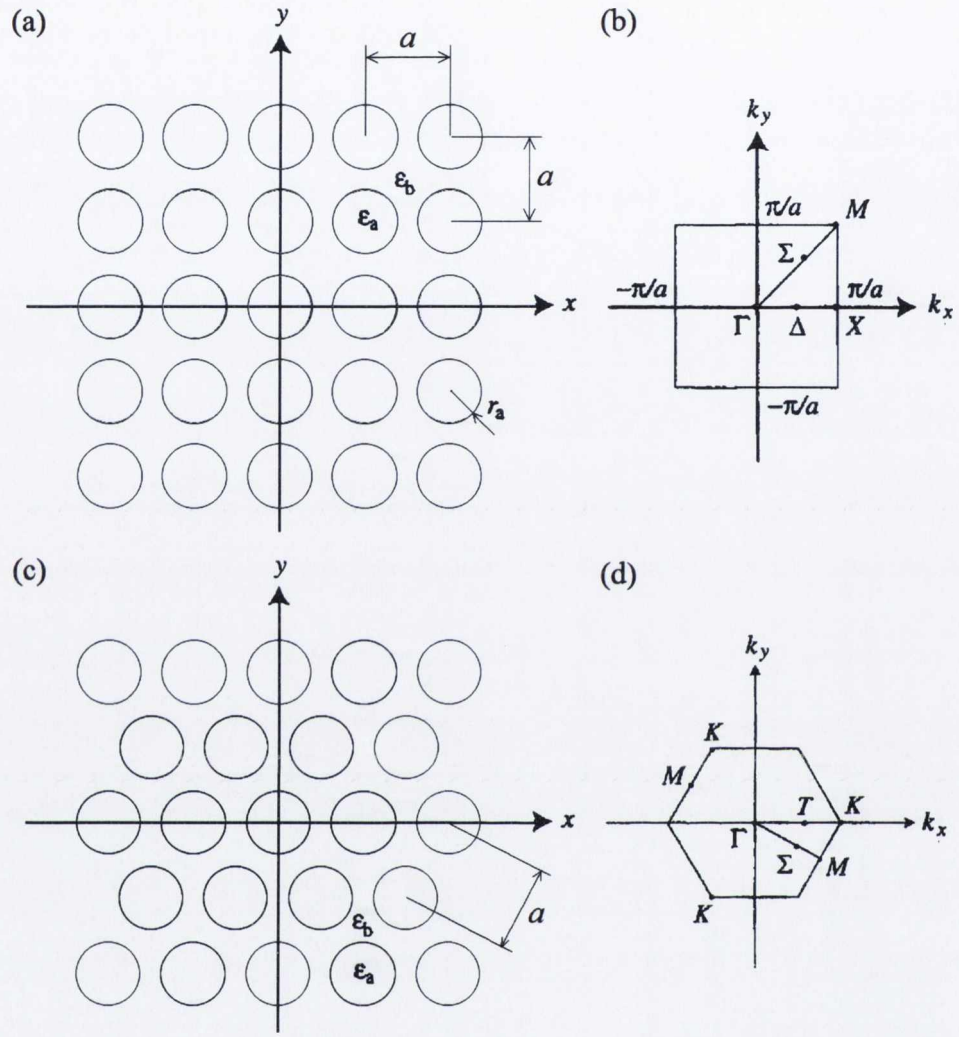

Figure 3.3: Sketch of two-dimensional photonic crystal with (a) square and (b) triangular lattices of circular cylinders and the corresponding first Brillouin zones for (c) square and (d) triangular lattices.

lattice (see Fig. 3.3a), the first Brillouin zone is a square with the side $2\pi/a$ and with the center at the Γ-point. In case of the triangular lattice (see Fig. 3.3c) the first Brillouin zone is a hexagon with the side $2\pi/a$ and the center at the Γ-point. The two-dimensional range of the wave numbers where it is required to solve the eigenproblem is the triangle ΓMX for square lattice and ΓMK for the triangular lattice. The solution of the eigenvalue problem for two-dimensional

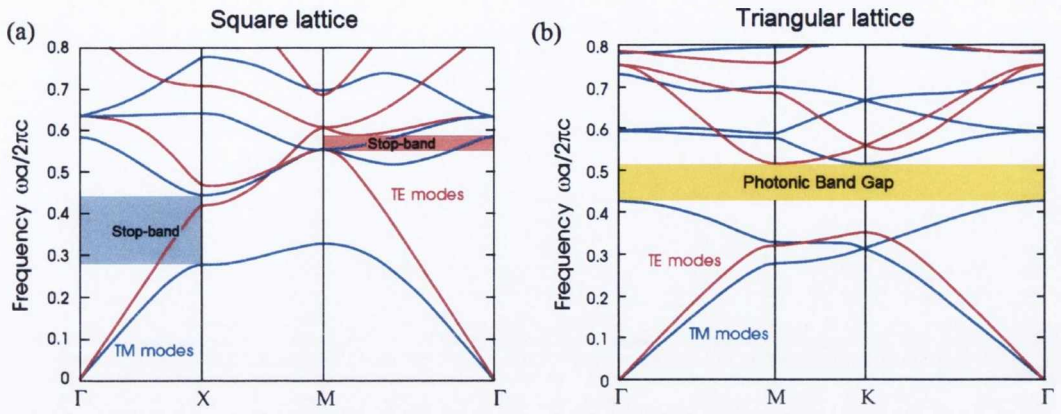

Figure 3.4: The photonic band gap structure for (a) square and (b) triangular array of dielectric columns with radius of $r = 0.2a$. The blue bands represent the TM modes and the red bands represent the TE modes. The columns ($\varepsilon_1 = 8.9$, as for alumina) are embedded in air ($\varepsilon_2 = 1$).

photonic crystals with the square and triangular lattices for the ranges of wave vectors ΓMX and ΓMK, respectively are shown in Fig. 3.4 in a loft form.

It is evident from Fig. 3.4 that for the case of square lattice there is no a *full photonic band gap*, common for all polarizations and all wave vectors. However, there are the so called *stop-bands* in which the wave equation has no solutions only for the individual polarizations and directions. The triangular lattice has the advantage over the square one that it has the full photonic band gap, as shown in Fig. 3.4b. This fact constitutes the main difference between the optical properties of two types of photonic crystal lattices. That is why for possible applications of photonic crystals, it is very important to choose their geometry properly.

The presence of the photonic band gap leads to the following statements:

- In the spectral range of the photonic band gap an eigen-state supported spontaneous emission is impossible. In particular, an electronic-hole recombination must be completely suppressed if the optical transition frequency is within the photonic band gap of the sample.

- Photons can be localized at the photonic crystal defect states that leads to the appearing of the unusual photonic states including bound atomic-photon states.

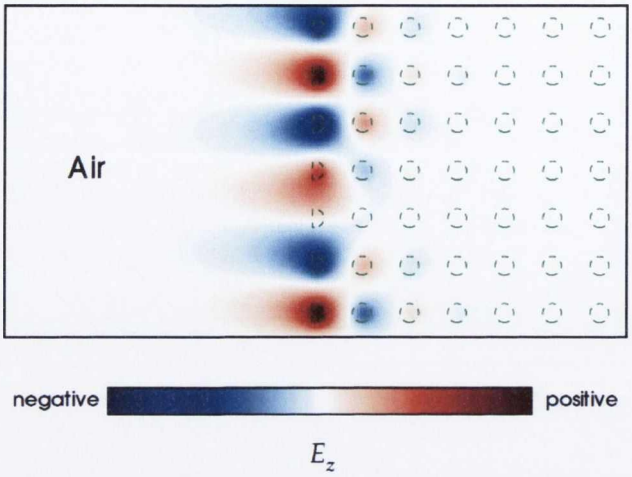

Figure 3.5: Electric field (E_z) pattern associated with a surface-localized state formed by truncating a square lattice of alumina rods (dielectric permittivity $\varepsilon = 8.9$, radius $r = 0.2a$) in air, cutting each rod in half at the boundary. The mode shown corresponds to a surface-parallel wave vector $k_y = 0.4(2\pi/a)$. The dielectric rods are shown as dashed green outlines [27].

Defects of the photonic crystal lattice, the breakdown of the translational symmetry of the spatial distribution of dielectric permittivity, an initial property of a photonic crystal, can change optical properties of the photonic crystals significantly. In this work we consider the violation of the periodicity of the dielectric constant on the interfaces and in the depths of the two-dimensional photonic crystal.

Any fabricated structure inevitably have an interface between the incoming medium and the photonic crystal. This leads to the existence of the so-called *surface states* (see Fig. 3.5). If the dispersion relations $\omega(k)$ of the surface states is within the photonic stop-band, the use of this photonic crystals can be limited. The surface states manifest itself as a dip in the region of a band gap in the reflection spectrum [24, 25, 26]. As can be seen from Fig. 3.6, the existence of the surface-related dip in the reflection spectrum depends on the geometry of the interface. The Tamm surface states of photonic crystals were investigated theoretically in Refs. [28, 29, 30, 31, 32, 33, 34]. These states were experimentally observed in Refs. [35, 36, 37]. It was found that the Tamm surface states in a

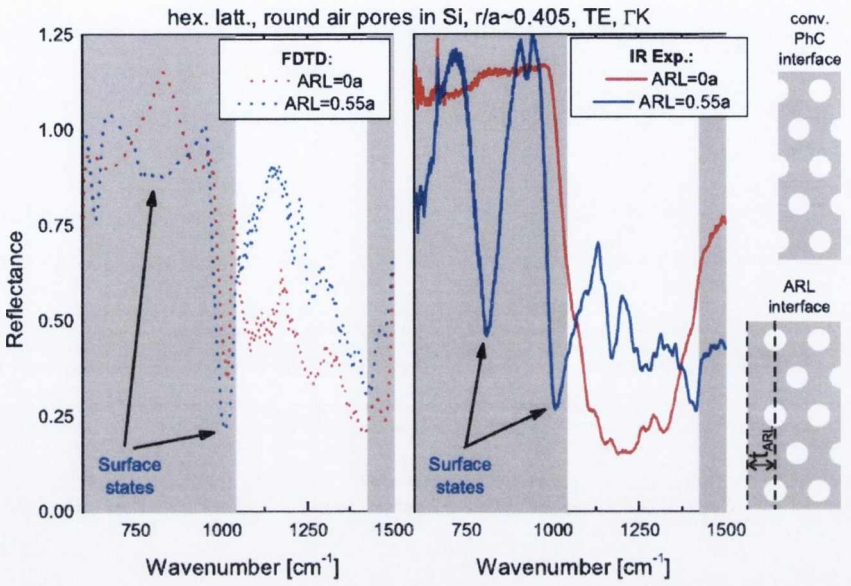

Figure 3.6: Reflection spectra of the plane wave from two types of interfaces between incoming air and two-dimensional photonic crystal, (a) calculated by FDTD method and (b) measured using an FTIR microscope. The photonic crystal is formed by the periodical array of macropores in silicon. The gray regions mark the position of photonic stop-bands for TE polarization [24].

two-dimensional photonic crystal can affect the quality of point imaging by a photonic crystal slab with negative refraction [38, 39]. In Refs. [31, 33], the enhancement of beaming via two-dimensional photonic crystal surface modes was studied. In Ref. [40], broad, surface-associated, dips in the reflection spectra of colloidal photonic crystals were demonstrated. In Refs. [25, 26], it was shown that surface modes generated in a thin layer of the photonic crystal matrix material provide highly efficient coupling of light into a slow light mode of photonic crystal. This effect was used for the fabrication of a miniature gas sensor exhibiting an enhancement of CO_2 infrared absorption by a factor of 3. From these references, it obvious, that the presence of surface states plays a crucial role in the optical characteristics of photonic crystals.

Another type of defects of photonic crystal lattice is a defect in depth of a structure. The first photonic crystal resonators used point and linear defects in the lattice. Recently, the photonic crystal heterostructure resonators were

introduced [41, 42]. It was shown that a very high quality factor together with a small volume of such resonators can be achieved [43, 44]. Fig 3.7 represents an example of the considered type of defects which is formed by a missed row of the cylinders in two-dimensional photonic crystal. This type of the defect can be regarded as a waveguide [45, 46, 47, 48, 49, 50] as well as an area of a double-heterojunction [41]. In the first case the light propagates along the missed row of cylinders, in the second case the light propagates perpendicular to it.

The described properties of photonic crystals allow one to obtain new elements and devices for optoelectronics, namely, photonic crystal fibers, photonic crystal waveguide narrow-band filters, high quality resonators etc. As follows from the literature (see for example [24, 25, 26]), when designing optical elements based on photonic crystals it is necessary to take into account the *imperfections of geometry* of the structure: aperiodicity, interface roughness and the size dispersion of alternating elements. The high contrast of refractive indexes of the silicon-based photonic crystal can lead to significant Rayleigh scattering of light

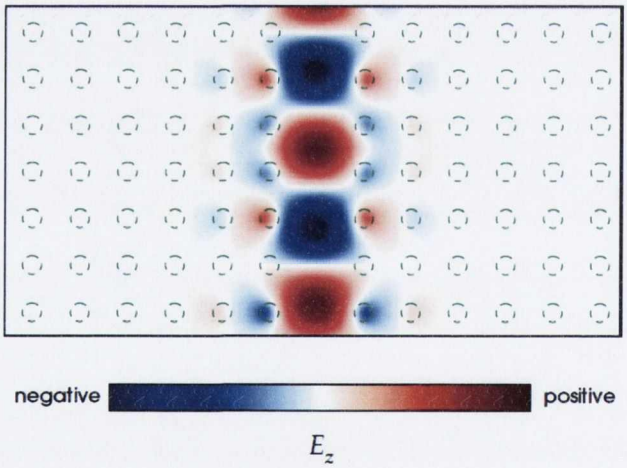

Figure 3.7: Electric field (E_z) pattern associated with a linear defect formed by removing a column of rods from otherwise-perfect square lattice of alumina rods (dielectric permittivity $\varepsilon = 8.9$, radius $r = 0.2a$) in air. The resulting field shown here for a wave vector $k_y = 0.3(2\pi/a)$ along the defect, is a waveguide mode propagating along the defect. The dielectric rods are shown as dashed green outlines [27].

at these imperfections [51], which can cause degradation of the eigen-modes in the photonic crystals and degradation of the resonance peaks in the transmission spectrum. Thus, the fabrication of photonic crystal structures for optoelectronics applications implies the preliminary research of the influence of inhomogeneity on their optical properties.

At the present moment in literature there are large number of publications devoted to the theoretical and experimental investigations of different type of photonic crystal structures and a large number of descriptions of their possible practical applications. At the same time, the quantitative analysis of the impact of geometrical imperfections of the fabricated photonic crystal structure on the surface-mode-related characteristics of their reflection spectra is absent in literature. Finally, the literature contain no data on the interaction between surface states and defect states localized at the interface and in-depth of the sample correspondingly.

Thus, the goal of the present chapter is the theoretical and experimental investigation of the role of the surface (Tamm) states on the reflection and transmission spectra of two-dimensional photonic crystals slabs made of macroporous silicon and theoretical investigation of the interaction between the surface states with defect states localized in-depth of the structure.

3.2 Investigated structures and details of calculation

The object of experimental and theoretical investigations of the present chapter is the silicon photonic crystal slab (PCS) with a triangular lattice of air cylinders (see Fig. 3.8). The reflection and transmission spectra were calculated by means the scattering matrix method (Section 2.2) and then measured using FTIR setup for experimental verification of the theoretical results. The reflection and transmission spectra of the samples were calculated at a normal incidence of light unless otherwise is stated. In calculation of reflection and transmission spectra of the photonic crystal slabs by the scattering matrix method the structure was considered to be infinitely extended in x- and y-directions and having a finite

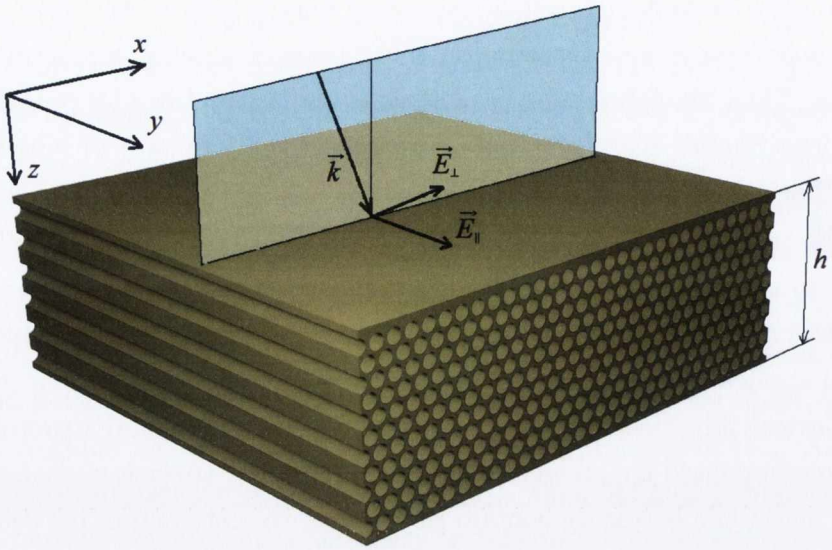

Figure 3.8: Photonic crystal slab with triangular lattice of air cylinders.

number of periods along the z-direction of light incidence, see the explanation of the axes and splitting in Fig. 3.9. Then the structure was split into the system of layers homogeneous along z-direction. In application of the scattering matrix method for the photonic crystal slabs the number of plain waves of $N_g = 29$ and number of stairs per pore $N = 20$ were found to be sufficient. One of the possible splittings of the photonic crystal slab is shown in Fig. 3.9a where an idealized *two-component* model structure is considered. The structure, shown in Fig. 3.9a, is non-absorbing since we are interested in the middle and far-infrared range where the bulk Si is transparent.

Any fabricated structure is characterized by inevitable roughness of inner surfaces of pores. Rayleigh light scattering on rough surfaces can significantly decrease the reflection coefficient from a photonic crystal in the regions of the photonic band gaps. There are a number of publications [4, 23, 52, 53, 54, 55] which show that these light losses are well accounted for by introduction of an imaginary part to the refractive indices of transparent materials. In order to simulate the pore roughness, we proposed [56] a three-component model for two-dimensional photonic crystal slabs explained in Fig. 3.9b. In a three-component model, an absorbing ring around a pore has been introduced to model light losses

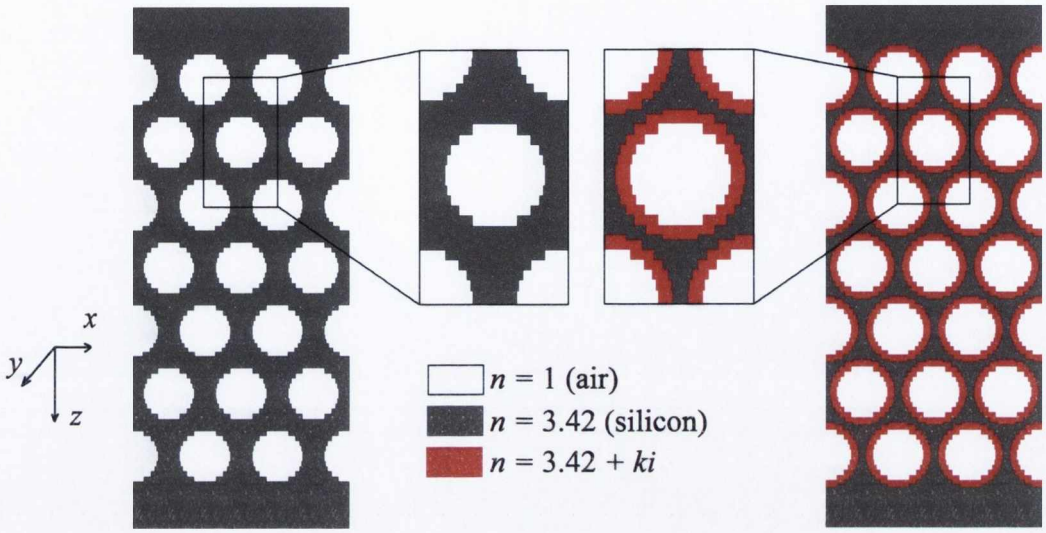

Figure 3.9: (a) Two-component model and (b) three-component model of a 2D photonic crystal slab with an absorbing ring.

due to roughness of the cylindrical air/silicon interface on a scale comparable with λ. It was shown in Ref. [56] that for a 2D photonic crystal lattice with a period of $8\,\mu$m, a ring width $\Delta r = 0.8\,\mu$m and a refractive index, $n_{abs} = 3.42 + 0.2i$, gives a very good fit between the calculated and measured reflection spectra in the region outside the fundamental photonic stop-band. In the present study the period of the fabricated structures is $3.75\,\mu$m, allowing us to register the 1-st (fundamental) photonic stop-band in the wavelength range 7–15 μm. In this chapter the same approach is used as in Ref. [56] for simulation of the influence of roughness on the reflection and transmission spectra. It will be shown in Section 3.4.3 that the parameters of the three-component model providing the best fitting between experimental and theoretical results are $\Delta r = 0.4\,\mu$m and $n_{abs} = 3.42 + 0.03i$.

3.3 Theoretical investigation of two-dimensional photonic crystals

3.3.1 Photonic stop-bands

A two-dimensional photonic crystal slab with a triangular lattice of 11 rows of air cylinders and with a lattice period a is characterized by two geometrical parameters: the radius of the cylinders, r, and the distance between the centers of the first row of cylinders and a plane separating the photonic crystal slab from air, w, denoted the interfacial layer thickness. Different surface terminations of the sample for different values of w are shown in Fig. 3.10. If $w > r$, the photonic crystal slab is separated from air by a homogeneous layer of silicon, while at $0 \leq w < r$ the surface is corrugated. Our goal was to investigate the influence of the geometrical parameters described on the reflection spectra of two-dimensional photonic crystal slabs. All calculations are performed for a normal angle of light incidence in the Γ-M direction because the fabricated structure edges were oriented along the Γ-K direction, orthogonal to the Γ-M direction. The results of calculations of the reflection spectra of the investigated structures for $r = 0.45a$ and $w = 0$ are shown in Figs. 3.11a,b for TM and TE polarizations. We use the notation TE polarization if the electric vector of the incident light is oriented parallel to the macropore channels, and TE polarization if the electric vector is perpendicular to them. It can be seen that the spectra contain regions of high reflection (for $a/\lambda = 0.29$–0.50 in TE polarization and for $a/\lambda = 0.26$–

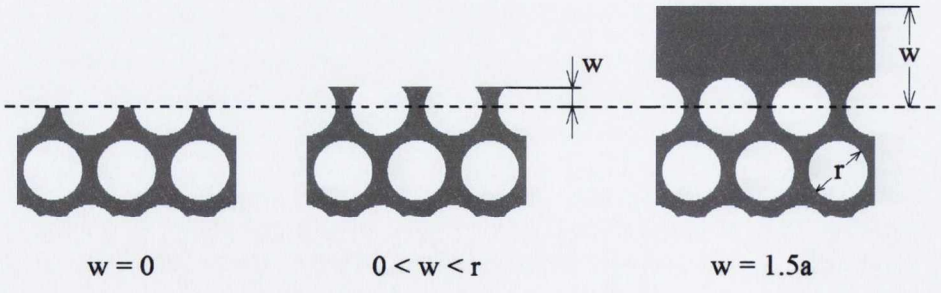

Figure 3.10: Surface termination of the photonic crystal slab for different values of the parameter w.

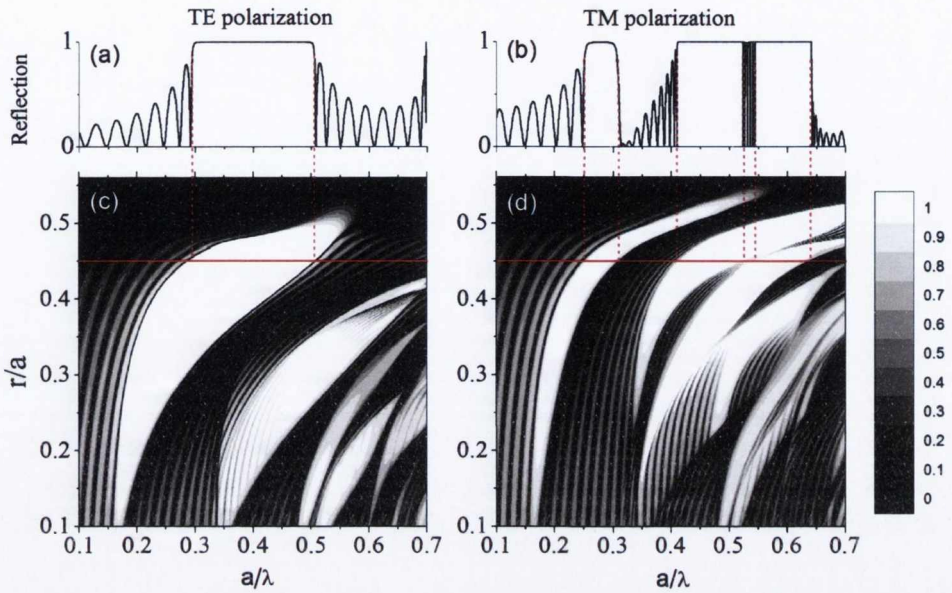

Figure 3.11: Reflection spectra of a two-dimensional photonic crystal slab in (a) TE and (b) TE polarization calculated using a two-component model, $r = 0.45a$, $w = 0$, Γ-M direction. Reflection coefficient in TE (panel c) and TM (panel d) polarizations of a two-dimensional photonic crystal slab as a function of the radius of pores, $r = (0.1\text{–}0.55)a$ and a/λ, for $w = 0$ interfacial layer thickness. The thickness of two-dimensional photonic crystal slab is 11 periods. Red solid and dashed lines show the correspondence between the top and bottom panels. The gray-shades scheme is explained in the bar in the right.

0.30, $a/\lambda = 0.41\text{–}0.52$ and $a/\lambda = 0.55\text{–}0.64$ in TE polarization) and regions with reflection coefficient oscillations between these high reflection regions. The high reflection regions arise due to the stop-bands of the two-dimensional photonic structure. The oscillations of the reflection coefficient outside the stop-bands are the Fabry-Pérot resonances for the light passing through the photonic crystal slab. In the long-wavelength range ($a/\lambda < 0.20$) the effective refractive indexes of the photonic crystal structure can be found by means of the Bruggeman equation:

$$\sum_{j=1}^{2} f_j \frac{\varepsilon_{eff} - \varepsilon_j}{\varepsilon_{eff} + L\varepsilon_j - \varepsilon_{eff}} = 0, \tag{3.7}$$

where for TE polarization depolarization factor $L = 1/2$ and for TE polarization $L = 0$, f_1 and f_2, are the filling fractions of air and silicon, ε_1 and ε_2 are the dielectric permittivities of air and silicon respectively. Calculated values of the refractive indexes are 1.73 and 1.95 for TE and TE polarizations. The periods of the Fabry-Perot oscillations for the homogeneous slabs with the thicknesses $l = 8.66a$ and refractive indexes 1.73 and 1.95 were found from the condition for Fabri-Perot resonance

$$l = \frac{\lambda}{2n_{eff}N}, (N = 1, 2, \dots) \tag{3.8}$$

and equal to $\Delta(a/\lambda)_{TE} = 0.0334$ and $\Delta(a/\lambda)_{TM} = 0.0296$. At the same time, the periods of the Fabry-Perot oscillations obtained from the long wavelength range of reflection spectra in Fig. 3.11a,b are 0.340 and 0.294, i.e. very close to those calculated by the effective medium model. The period of the Fabry-Perot oscillations obtained from the short wavelength range ($a/\lambda > 0.65$) of the reflection spectra are 0.190 for TE polarization and 0.140 for TE polarization. These periods cannot be described by Bruggeman equation because the condition of applicability of effective medium model ($\lambda >> a$) is not fulfilled in the short wavelength range. In order to investigate the influence of pore radius on reflection spectra, the reflection spectra of two-dimensional photonic crystal slab with 11 rows of pores were calculated with parameter $w = 0$ and r varying from $0.1a$ to $0.55a$. The results of these calculations are shown in Figs. 3.11c,d as reflection maps, see the shades of gray bar for explanation of the scale. It can be seen that the TE reflection spectra have the lowest stop-band at $0.1a < r < 0.52a$. The width of the lowest stop-band reaches a maximum at $r = 0.45a$. The maximum width of the lowest stop-band using TE polarization is reached at $r = 0.43a$, whereas the widest second stop-band is provided by a pore radius $r = 0.47a$.

3.3.2 Surface states

As was already mentioned in the Section 3.1, in this work we investigate the surface states which are attributed to the homogeneous silicon layer separating photonic crystal area from the air. The thickness of this homogeneous layer is the only geometrical parameter which affects the existence of the surface states. Let

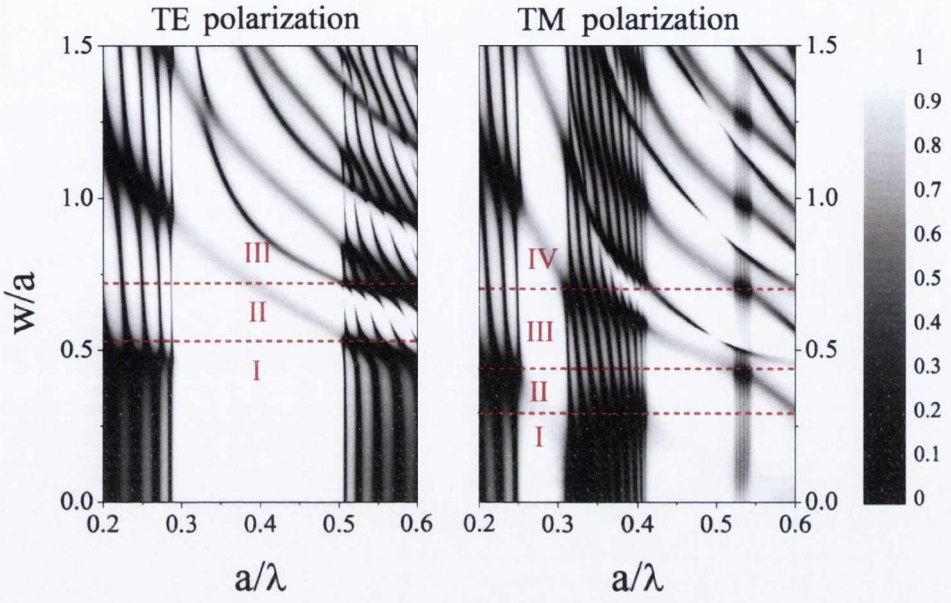

Figure 3.12: Calculated reflection coefficient in TE and TE polarization of a two-dimensional photonic crystal slab as a function of the interfacial layer thickness, w, and a/λ, for $r = 0.45a$, Γ-M direction. Dashed lines and Roman numbers mark the different zones discussed in the text. The grey-shades scheme is explained in the bar in the right.

us investigate the influence of the interface on the reflection spectra. For this, we fixed the radius of the cylinders at $0.45a$ and varied the parameter w in the range of 0–$1.5a$. The results of these calculations with a two-component model are shown in Fig. 3.12. From Fig. 3.12, the calculated reflection spectra in the range $a/\lambda = 0.2$–0.6 consist of stop-bands, Fabry-Pérot oscillations and, additionally, dips within the high reflection regions. The widths and the positions of the stop-bands do not depend on the thickness of the air/PCS interface. Hence, for fixed a, the pore radius is the only parameter which is responsible for the widths and positions of the photonic stop-bands. The period of the Fabry-Pérot oscillations decreases slightly with an increase of interfacial layer thickness. This is expected since the period of the Fabry-Pérot oscillations is inversely proportional to the total sample thickness. The most interesting behavior is demonstrated by the reflection dips inside the photonic stop-bands. The dip position depends on w,

the air/PCS interface thickness. The TE reflection (TE reflection) map can be divided into three (four) zones by the number of these dips in the spectrum, as shown in Fig. 3.12. The TE stop band in zone I-TE does not have these dips. The first dip appears at $w = 0.55a$. The position of the first dip shifts towards lower wavenumbers with increasing w and reaches the left edge of the stop-band at $w = 0.92a$. The high reflection region has only one dip for $0.55a < w < 0.72a$ (zone II-TE). For $w > 0.72$ (zone III-TE) the high reflection region has two or more dips. Similar behavior is observed using TE polarization. The results shown in Fig. 3.12 are very important for the fabrication of structures with triangular lattice of air pores in silicon. Indeed, from Fig. 3.10, the surface termination of a 2D photonic crystal slab is flat when $w > r$. In this case, $w > 0.45a$. At the same time, a "pure" stop band in the TE reflection spectra, i.e., a stop band without surface dips, exists only for $w < 0.55a$ (zone I-TE). Thus, the range of the values of parameter w which provides the flat surface termination and a "pure" photonic stop-band is $0.45a < w < 0.55a$.

In order to understand the origin of the dips in the reflection spectra, we calculated the electromagnetic near-field distribution in the 2D photonic crystal slab. We will limit our discussion to structures of period $a = 4\,\mu$m with a pore radius $r = 0.45a$, an interfacial layer thickness $w = 0.62a$, TE polarization and a normal light incidence. The spatial electric and magnetic field distributions in the near-surface region are shown in Fig. 3.13 for $a/\lambda = 0.46a$, which corresponds to the position of the dip inside the photonic stop-band in the TE reflection spectra. The method used to present the electro-magnetic field is described in Ref. [57]. The electric and magnetic field vectors are shown in Fig. 3.13 as a two dimensional array of cones and circles (actually a face on views of cones perpendicular to the image plane).

The size of the cones is proportional to the field strength at the center of each cone. The length of the blue cones is scaled to the amplitude of the incoming wave in vacuum; in a case of red cones it is reduced by two, to prevent cone overlap. Note that the electric and magnetic fields are depicted at the instant t (measured in units of light period T and shown in the title of each panel) when the field intensities, integrated over the displayed cross sections, reach a maximum. $E_{\max}$ ($H_{\max}$) is the maximum field measured in units of the incoming wave amplitude

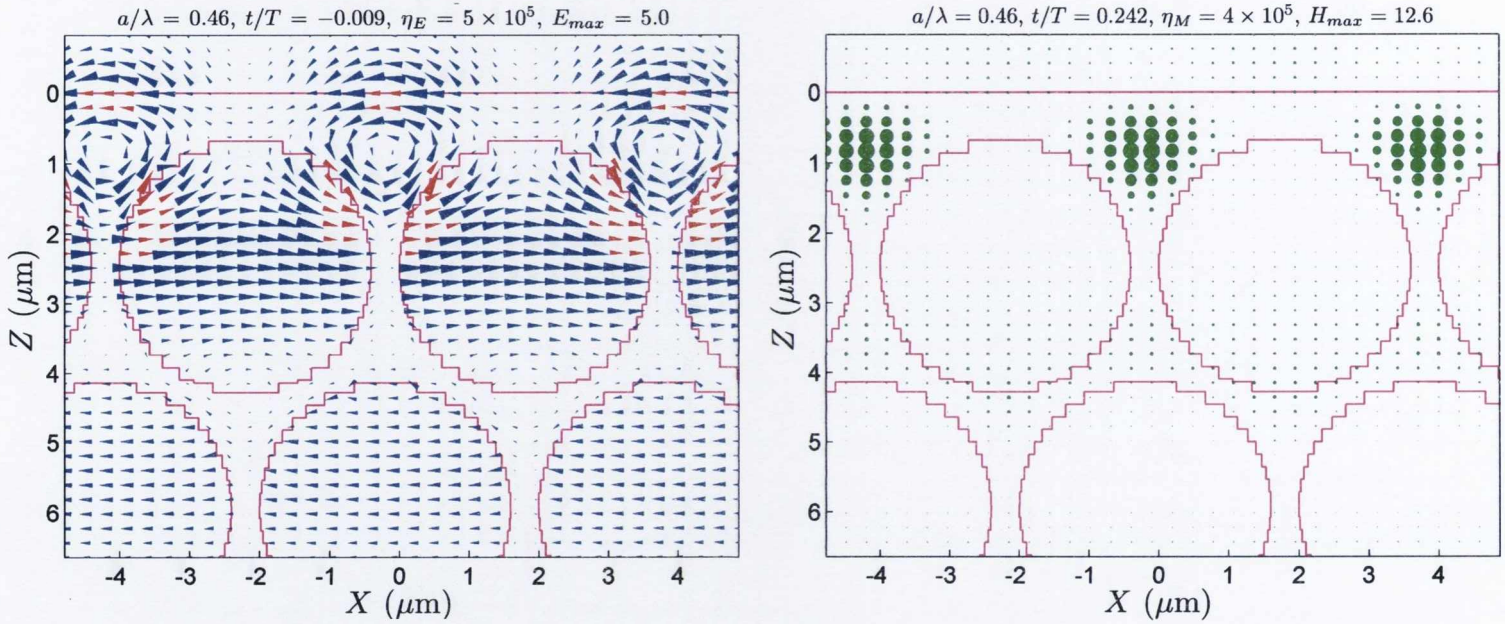

Figure 3.13: Calculated spatial distributions of the electric (blue and red cones in panel (a)) and magnetic (green circles in panel (b)) fields in 2D photonic crystal slab for normal incidence of TE polarized light. The length of the cones (circles area) is proportional to the field strength at the central point of each cone (circle). Cones specify the corresponding electric field direction by their orientation. The magnetic field in the TE polarization is along y-axis. Fields are shown for an incoming frequency $a/\lambda = 0.466$ corresponding to the dip in the photonic stop-band for TE polarization. $r = 0.45a$, $w = 0.62a$. The calculation was performed for $a = 4\,\mu$m.

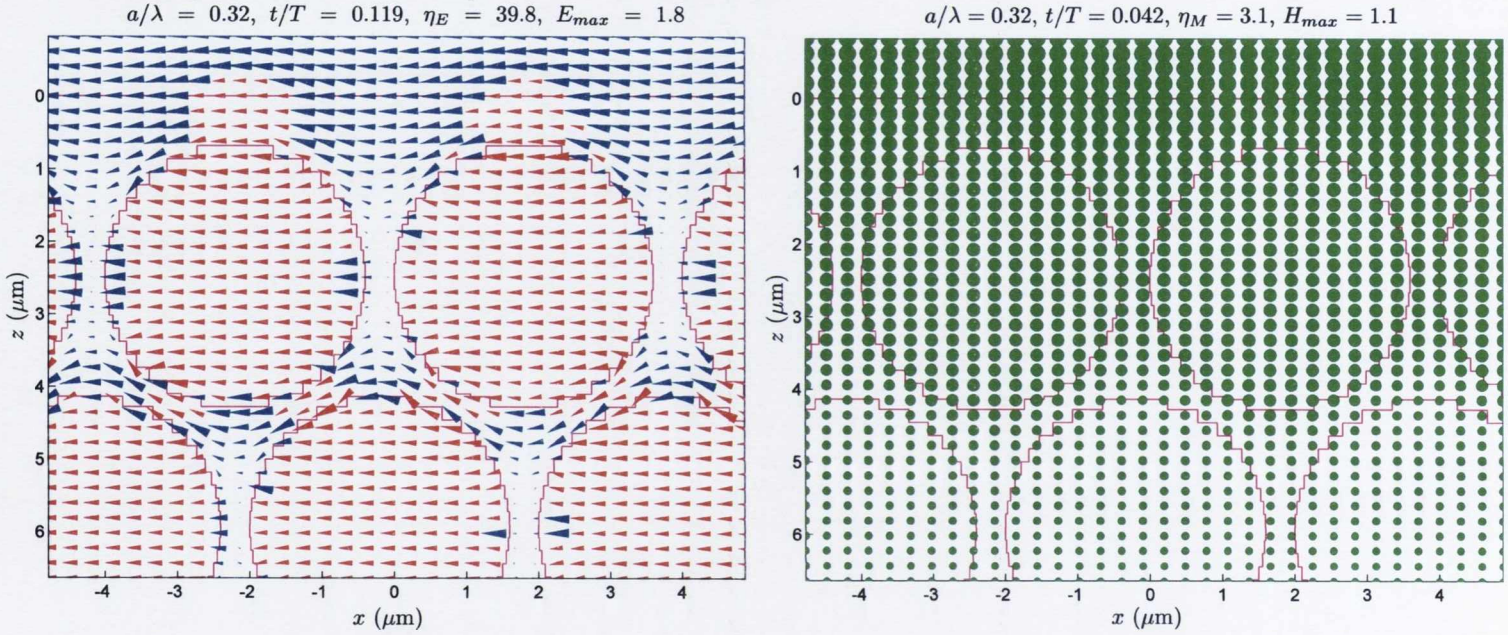

Figure 3.14: Calculated spatial distributions of the electric (blue and red cones in panel (a)) and magnetic (green circles in panel (b)) fields in 2D photonic crystal slab for normal incidence of TE polarized light. The length of the cones (circles area) is proportional to the field strength at the central point of each cone (circle). Cones specify the corresponding electric field direction by their orientation. The magnetic field in the TE polarization is along y-axis. Fields are shown for an incoming frequency $a/\lambda = 0.32$. The calculation was performed for $a = 4\,\mu$m.

(i.e., it shows the field enhancement in the near field zone). It can be seen that the electric and magnetic fields are localized in the near-surface region. Note that electric field in this region takes the shape of vortices located between the upper pores. The maxima of the magnetic fields are in the centers of these vortices. The time difference between the part at which electric and magnetic fields becomes maximal is approximately a quarter of the oscillation period, $t \approx 0.25T$. Hence, the field distribution, shown in Fig. 3.13, corresponds, in the main, to a standing wave. The ratio between the maximal and minimal electric (magnetic) field energies over the period of electromagnetic oscillation η_E (η_M), a so-called field modulation coefficient, are also shown in the title of Figs. 3.13. The η_E and η_M values exceed unities by several orders of magnitude. This is also characteristic of the standing wave of the surface mode. The mode described here is a surface Tamm state [58]: it arises in the stop band due to the total light reflection from the silicon/photonic crystal interface and exponentially decreases inside it. However, it is open for radiative losses on the other partially reflecting air/Si interface and thus differs from the usual Tamm electronic states on the solid/vacuum interface. Such modes have been considered, e.g., in Ref. [34] and are characterized by a small quality factor (as Fabry-Pérot modes).

For comparison, the electromagnetic field distributions were calculated for the the frequency $a/\lambda = 0.32$. The spectral position of this frequency is within the photonic stop-band however this frequency does not support the surface mode. From the results of calculations shown in Fig. 3.14 it follows that the distribution of the electric field does not have the vortices however the average intensity of the field decays with the depth of the structure. The latter is due to the fact that the frequency $a/\lambda = 0.32$ is within the photonic stop-band.

3.3.3 Cavity states

Let us move to the description of the cavity states similar to that shown in Fig. 3.7. The difference between the surface states and the cavity states is that the surface states are located near the surface of the structure while the cavity states are located in depth of the structure. The investigated photonic crystal slab with the cavity is shown in Fig. 3.15. The cavity groove is infiltrated with

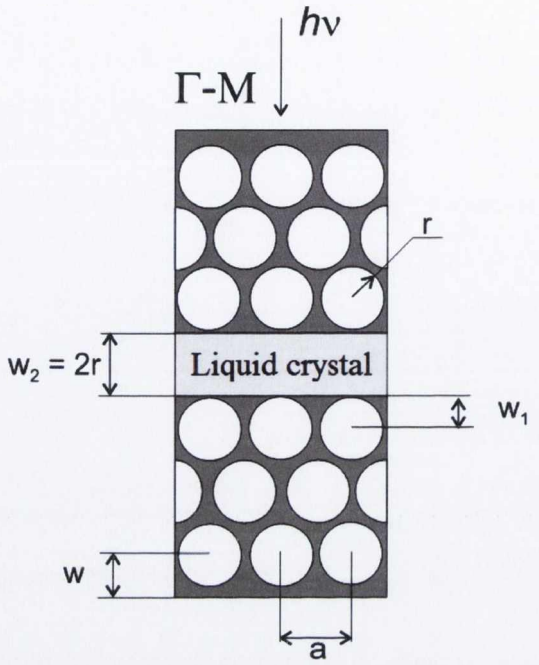

Figure 3.15: Two-dimensional photonic crystal structure with linear defect infiltrated with liquid crystal. a is the lattice period, r is the pore radius. Width of the linear defect is $w_2 = 2r$.

the liquid crystal E7. The refractive index of the liquid crystal can be varied within the range from 1.49 to 1.69 [59]. The reflection spectra of the investigated cavity structures are shown in Fig. 3.16 along with the reflection spectra of the structure without cavity. The refractive index of cavity medium is $n = 1.5$. The spectra were calculated for $w_1 = 0.45a - 0.55a$ and fixed $w = 0.45a$. This value of the parameter w corresponds to the structure without a homogeneous surface layer, i. e. air/PCS interface is tangent to the pores in the first row.

The boundaries of the first photonic stop-band of the corresponding infinite photonic crystal with triangular lattice of air cylinders and $r = 0.45a$ have the spectral positions $a/\lambda = 0.30$ and 0.49 [60] and shown in 3.16 by vertical dashed lines. It can be seen from Fig. 3.16 that the defect layer in the photonic crystal slab leads to appearance of the sharp dip (a) in the region of the stop-band of the reflection spectra. This dip is attributed to the allowed state within the photonic forbidden band. If the parameter $w_1 = 0.45a$ then the "cavity medium/PCS"

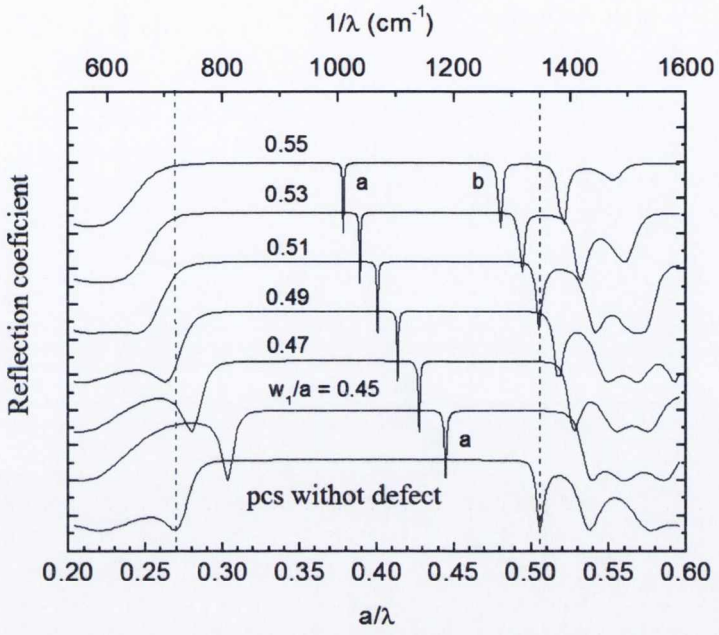

Figure 3.16: Reflection spectra of the two-dimensional photonic crystal structures without defect and with defect for different values of the parameter w_1. Parameter of the microcavity: $w_2 = 2r$, $w = 0.45$, $n = 1.5$. Dashed lines bounds the first photonic stop-band of the corresponding photonic crystal lattice in Γ-M direction, TE polarization. The upper scale shows the values of wavenumber of light for the structure with period of $a = 3.75\,\mu$m.

interface is tangent to the pores in the rows which are bounded the cavity layer. If $w_1 > 0.45a$ then there is a homogeneous silicon layer between the cavity layer and the pores. The increase of the thickness of this homogeneous layer leads to the redshift of the spectral position of the cavity dip. If $w_1 > 0.51a$ then there are two dips, (a) and (b), within the stop-band.

In order to demonstrate the influence of the refractive index of the cavity medium n, we calculated the reflection spectra for different values of the parameter n varying in the range from 1 to 1.7 (Fig. 3.17). It can be seen from Fig. 3.17 that upon the increase of the refractive index of the cavity medium, the reflection dip (a) is redshifted whereas the spectral position of the dip (b) remains the same. Hence, the dip (a) is attributed to the localized state of the linear defect of the

photonic crystal lattice and its spectral position corresponds to the frequency of the microcavity. In order to find the optimal parameters of the cavity, we calculated the cavity wavenumber for the refractive index varied from 1 to 1.7 and the the parameter w_1 varied from $0.45a$ to $0.7a$. The results of these calculations are shown in Fig. 3.18 where three curves for $w_1 = 0.45a$, $0.52a$ $0.63a$ are presented. The solid horizontal lines denote the boundaries of the first stop-band, dashed vertical lines shows the range of variation of the refractive index of the liquid crystal E7. It can be seen from Fig. 3.18 that using the liquid crystal E7 it is possible to achieve the spectral shift of the cavity peak position by a value of $\Delta(a/\lambda) \approx 0.025$ or $\Delta\lambda^{-1} \approx 670\,\mathrm{cm}^{-1}$ in case of $a = 3.75\,\mu\mathrm{m}$. The thickness of homogeneous silicon layer between the cavity and pores, $w_1 - r$, affects the spectral position of the cavity dip in the photonic stop-band. The increase w_1 leads to the redshift of the cavity frequency (see Fig. 3.16). Hence, the proper choice of

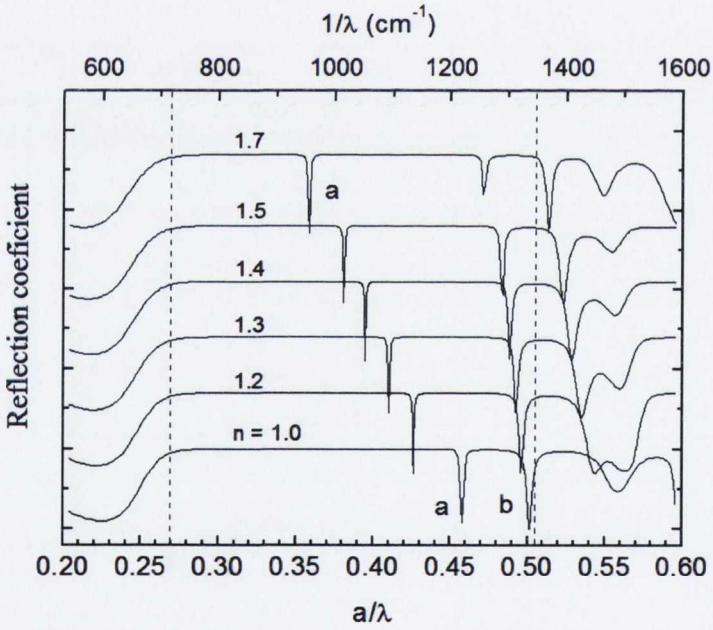

Figure 3.17: Reflection spectra of the photonic crystal slab with linear cavity calculated for different refractive indexes of the cavity medium: $n = 1.0-1.7$. Parameters of the structure: $w_2 = 2r$, $w_1 = 0.55a$, $w = 0.45a$. The upper scale shows the values of light wavenumber for the structure with the period $a = 3.75\,\mu\mathrm{m}$.

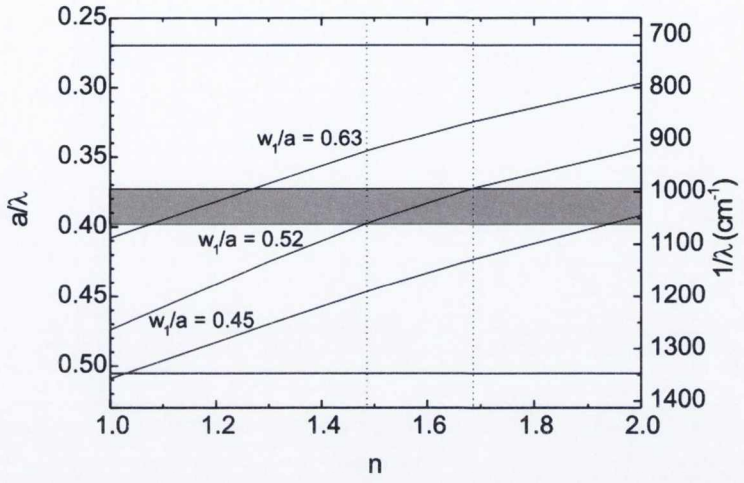

Figure 3.18: Dependence of the cavity wavenumber (dip (a) in Fig. 3.17) on the refractive index of cavity medium. The curves correspond to different parameters $w_1 = 0.45a$, $0.52a$, $0.63a$. Right scale shows the light frequencies for the structure with the period $a = 3.75\,\mu$m.

the thickness of the homogeneous silicon layer enables us to achieve the desired spectral positions of the cavity operating range. For example, for $w_1 = 0.52a$, the cavity frequencies are in the range $a/\lambda = 0.372 - 0.397$ depending on the refractive index of cavity medium and are in the middle of the photonic stop-band. The operating range of the cavity is shown in Fig. 3.18 by gray rectangle.

3.3.4 Interaction of surface and cavity states

Let us consider a photonic crystal slab with a homogeneous silicon layer as well as with a linear defect. As in the previous sections we assume that the photonic crystal has triangular lattice with air pores and the light propagates along Γ-M direction. The sketch of the model structure for the calculations of the reflection spectra is shown in Fig. 3.15. In the present section all calculations are performed for the photonic crystal structures with pores radius of $0.45a$ and the thickness of the defect, w_2, is the double of pore radius, i. e. $0.9a$. From Section 3.3.2 it follows that the surface dip of the ideal structure is characterized by low amplitude (less than 0.01) and, therefore, is invisible in the reflection spectrum plotted with the

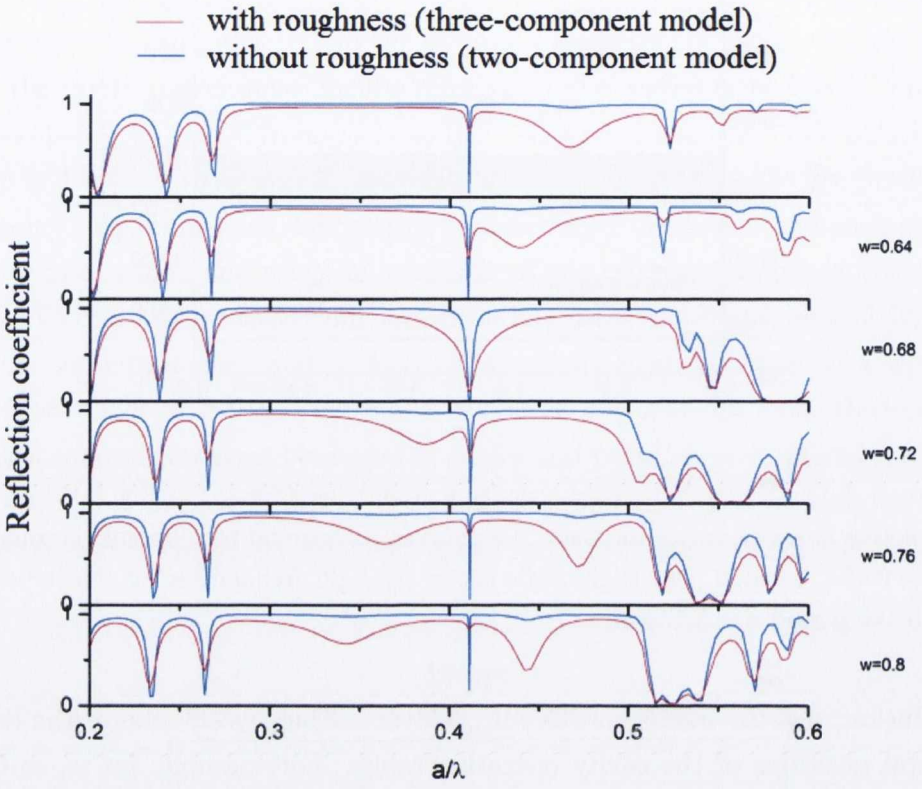

Figure 3.19: Reflection spectra of the photonic crystal slab with linear defect. Pore radius $r = 0.45a$, $w = 0.6a - 0.8a$, thickness of the linear defect $w_2 = 0.9a$, $w_1 = 0.5a$.

vertical range from 0 to 1. At the same time, the roughness of inner surfaces of pores leads to the increase of the amplitudes of the dips without a spectral shift. Thus, for the sake of simplicity, we use the three-component model with the thickness of the absorption ring $\Delta r = 0.4\,\mu$m and the refractive index of the material of the ring $3.42 + 0.1i$. From the other side, the introduction of absorption into the structure leads to a sufficient degradation of the cavity dips. Hence, for presentation of the cavity dips we use the two-component model. Let us calculate the reflection spectra of the photonic crystals structure from Fig. 3.15 containing the surface defect and the linear defect in-depth of the structure. Parameter w is changed between $0.6a$ and $0.8a$, parameter $w_1 = 0.5a$ and is

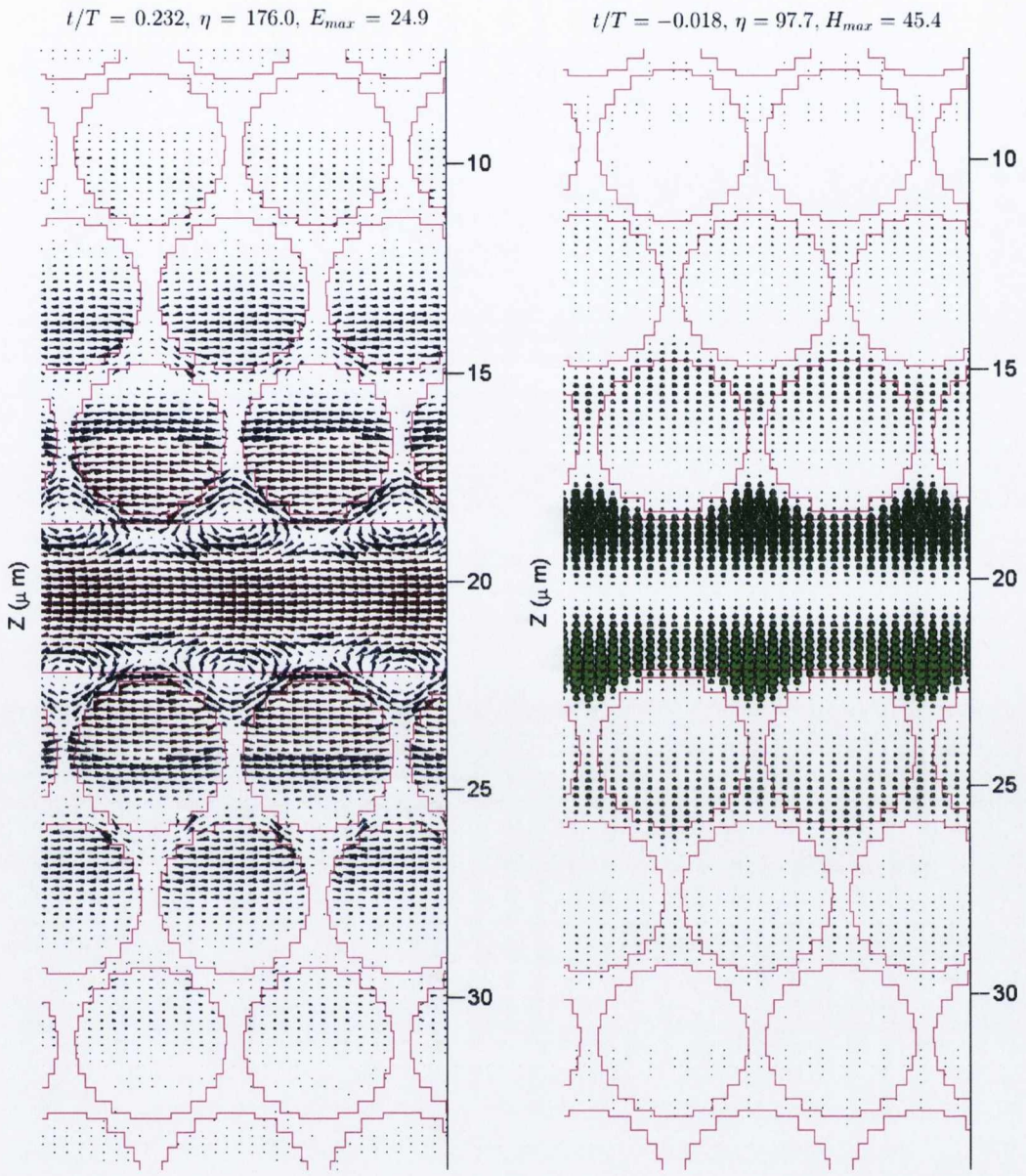

Figure 3.20: Spatial distribution of the electric field at the time moment $t/T = 0.232$ (blue and red arrows on the left panel) and the magnetic field at the time moment $t/T = -0.018$ (green circles on the right panel) in the two-dimensional photonic crystal slab with 10 rows of pores (5 in upper and lower parts) calculated for normal angle of light incidence, TE polarization, $r = 0.45a$, $w = 0.68a$, $w_1 = 0.5a$, $w_2 = 0.9a$. The field are shown for the incident light frequency of $a/\lambda = 0.4107$, that corresponds to the double resonance (intersection of the spectral positions of surface and cavity modes).

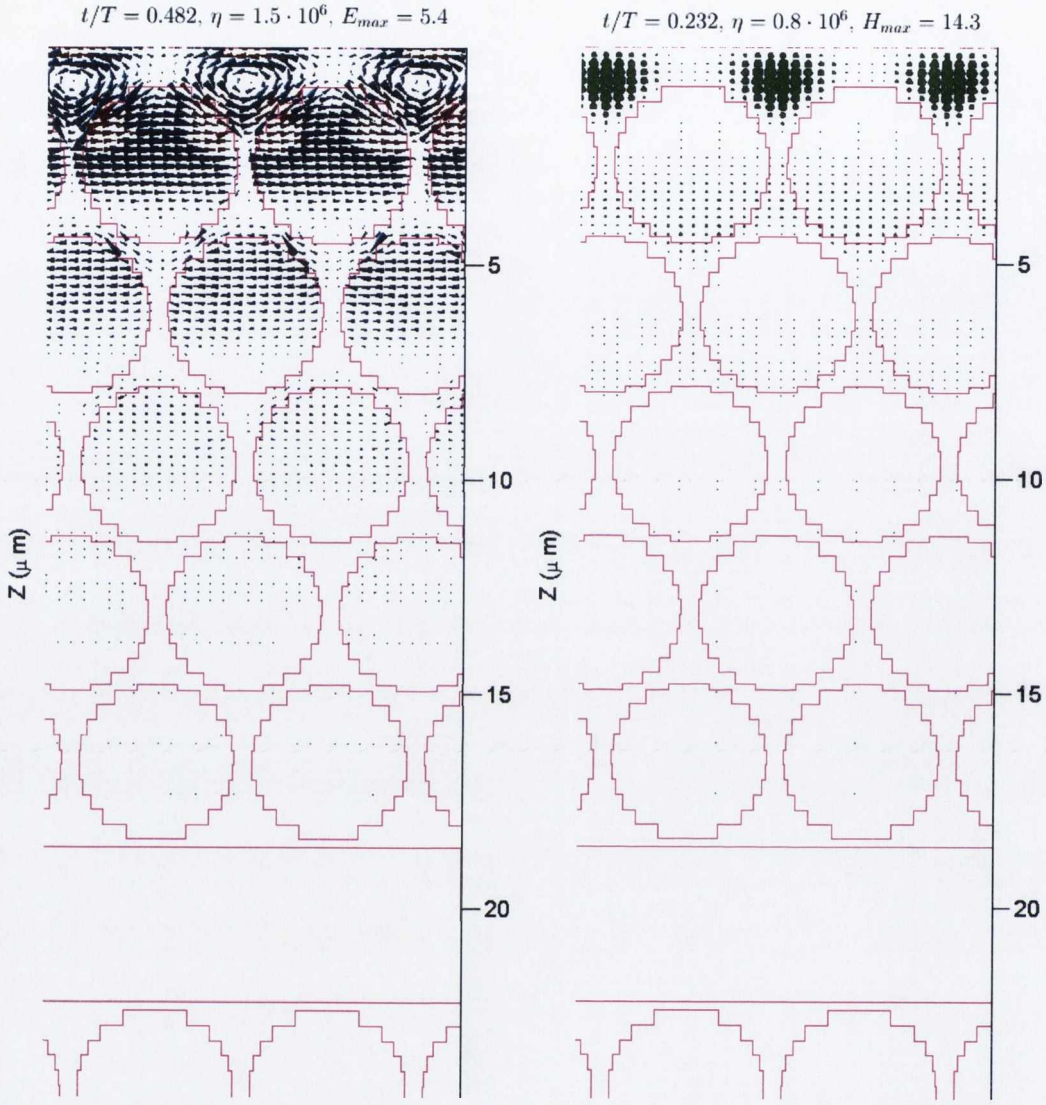

Figure 3.21: Spatial distribution of the electric field at the time moment $t/T = 0.482$ (blue and red arrows on the left panel) and the magnetic field at the time moment $t/T = 0.232$ (green circles on the right panel) in the two-dimensional photonic crystal slab with 10 rows of pores (5 in upper and lower parts) calculated for normal angle of light incidence, TE polarization, $r = 0.45a$, $w = 0.68a$, $w_1 = 0.5a$, $w_2 = 0.9a$. The field are shown for the incident light frequency of $a/\lambda = 0.4107$, that corresponds to the double resonance (intersection of the spectral positions of surface and cavity modes).

fixed. Refractive index of the cavity medium is $n = 1.5$. Results of calculations are shown in Fig. 3.19. It follows from Fig. 3.19 that the spectral position of the cavity dip is constant and does not depend on the width w. At the same time, the spectral position of the surface dips is changed from $a/\lambda = 0.34$ to 0.45. Moreover, for $w = 0.76a$ and $0.8a$ there are two surface dips within the stop-band of the reflection spectrum. The described behavior in the reflection spectra is in accordance with data shown in Fig. 3.12. Note that for $w = 0.68$, the spectral positions of the cavity and the surface dips coincide. Let us calculate now the spatial distribution of the electromagnetic field of incident light at the frequency $a/\lambda = 0.41a$ in the structure with $w = 0.68$ that corresponds to the intersection of spectral positions of the surface and cavity states. The results of calculations of electric and magnetic field distribution for the moments of time $t/T = 0.232$ and $t/T = -0.018$ correspondingly are shown in Fig. 3.20. The fields are located near the linear defect. The electric field has an antinode in the center of the defect, and the magnetic field has a node. The modulation coefficients, η_E and η_M exceed unity by two orders of magnitude. The distributions of the field at the moments of time $t/T = 0.482$ and $t/T = 0.232$ correspondingly (Fig. 3.21) are located at the sub-surface region. The modulation coefficient exceed unity by two orders of magnitude too. The described characteristics of the electromagnetic field indicate that the standing wave at the double resonance has the features of both cavity and surface modes and the nodes of these modes are shifted by a phase of $\pi/2$.

3.4 Experimental observation of surface photonic states in two-dimensional photonic crystals

3.4.1 Fabrication of the samples of two-dimensional photonic crystals

In order to fabricate two-dimensional photonic crystal slabs, we used joint photoelectrochemical etching of deep macropores and trenches in a silicon wafer. [51, 61, 62, 63]. As a starting material, we used n-Si (100) wafers of resistivity $\rho = 5\,\Omega{\cdot}$cm

and a thickness of 250 μm. Nucleation centers were formed by photolithography followed by anisotropic etching in a hot aqueous alkaline solution. The mask layer was silicon dioxide formed by plasma-enhanced chemical vapor deposition.

The triangular lattice of nucleation centers for macropores (pits) had a period of $a = 3.75\,\mu$m. The choice of another geometrical parameter, namely the distance between the nucleation grooves for trenches and the centers of the nearest row of pits, d (see Fig. 3.22), is an important issue. The trenches violate the order in the periodic structure and cause a redistribution of the local current density during etching. It has been shown that distortion of the photonic crystal lattice around the defect can be minimized by following certain rules [51, 63]. Too small a value of d can give a fragile trench, or a trench that reduces with depth; too large a value of d can lead to a wide trench with strongly corrugated walls and a reduced size of pores next to the trench. The optimal value of the parameter d is around a; the width of the trench is of approximately $2r$.

The trenches define rectangular areas of the sample which were removed after detachment of the substrate (Fig. 3.22). The resulting photonic crystal slab

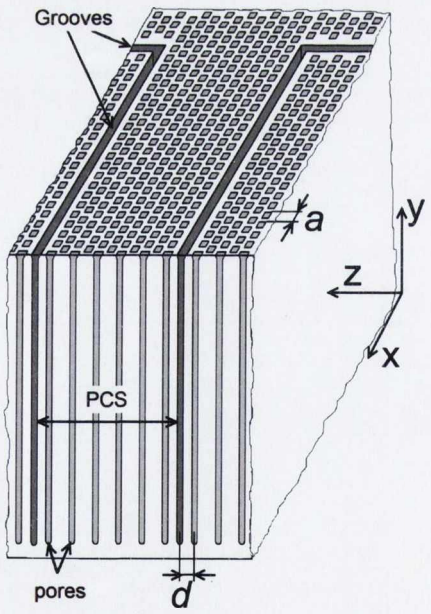

Figure 3.22: Schematic of the photonic crystal slab structure after photo-electrochemical etching of macropores and trenches.

is aligned along Γ-K direction of the photonic crystal lattice and consists of 11 pore rows terminated with a silicon pre-layer of width $w = d - r$. The photomask defines $d = 4.25\,\mu$m ($d/a = 1.13$), which for $r = 0.45a$ gives $w = 0.68a$. Photoelectrochemical etching was performed in an aqueous solution containing 4% hydrofluoric acid (HF) + 5% ethanol at 20°C with backside illumination. A constant radius mode was used, with an initial current density $j = 10$ mA/cm^2 [64]. The etching process leads to the formation of air cylindrical pores of radius $r = 1.4\,\mu$m and trenches of width $2.93\,\mu$m. The etching depth was about $180\,\mu$m. Increase of the etching current density to the critical value of [64, 65] $j_{PS} = 31$ mA/cm^2 and higher leads to the separation of the porous layer from the substrate and the formation of a free-standing membrane. In order to increase

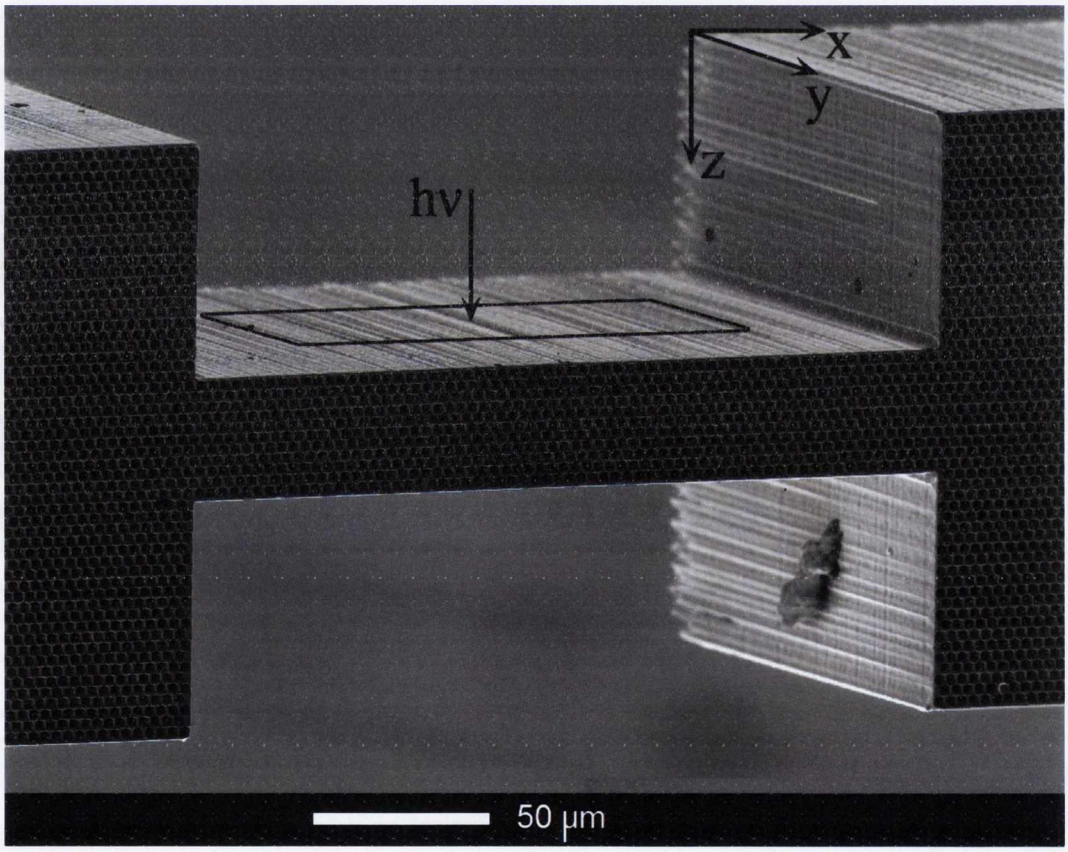

Figure 3.23: Scanning electron microscopy (SEM) image of the two-dimensional photonic crystal.

the pore filling factor r/a, the structures were oxidized in a wet-steam atmosphere at a temperature of 1100°C with subsequent dissolution of the oxide in HF solution. Figure 3.23 shows the SEM image of the resultant structure of the photonic crystal slab. The samples were then glued to a sample holder allowing measurement of the reflection and transmission spectra.

3.4.2 Experimental setup

Fourier Transform Infrared (FTIR) measurements were performed in the range 650–6500 cm^{-1} with a resolution of 8 cm^{-1} using a Digilab FTS 6000 spectrometer in conjunction with a UMA 500 infrared microscope. A gold coated glass slide was used as a 100% reflection reference. A rectangular aperture of 50×200 $\mu\mathrm{m}^2$ for the IR beam was used to provide a reasonable signal to noise ratio (see Fig. 3.24). FTIR measurements were made with a polarizer placed in front of the MCT (Mercury, Cadmium, Telluride) detector attached to the microscope. The incidence light beam was focused on the sample. The angles of incidence were from 10° to 30° in xz incidence plane and due to the long rectangular aperture of the beam did not exceed 8° in yz incidence plane as is shown in Fig. 3.24.

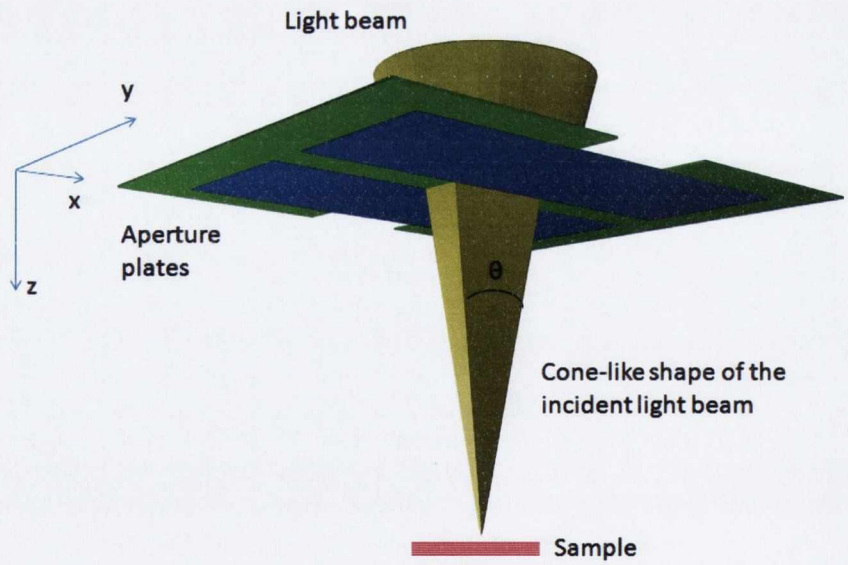

Figure 3.24: Sketch of the illumination of investigated sample by the probe light.

3.4.3 Experimental results

Experimentally obtained reflection spectra for TE and TE polarizations are shown in Figs. 3.25a,b. Theoretical spectra were calculated for a fixed angle of light incidence of 20° with two-component model and are shown by the dotted line in Figs. 3.25c,d. The widths and positions of the photonic stop-bands in the theoretical reflection spectra coincide with those in the experimental spectra. The theoretical spectra demonstrate one dip in the first stop band of the TE spectrum ($a/\lambda = 0.477$) and one dip in the second stop-band of the TM spectrum ($a/\lambda = 0.491$). The amplitude of the dip in the TE reflection spectrum for two-component model is 0.07, rendering it invisible on this scale. From an analysis of the theoretical results shown in Fig. 3.12, these dips are associated with the surface modes. The spectral positions of surface dips in the experimental and theoretical spectra coincide with each other. However, there is some disagreement between experimental and theoretical spectra calculated by the two-component

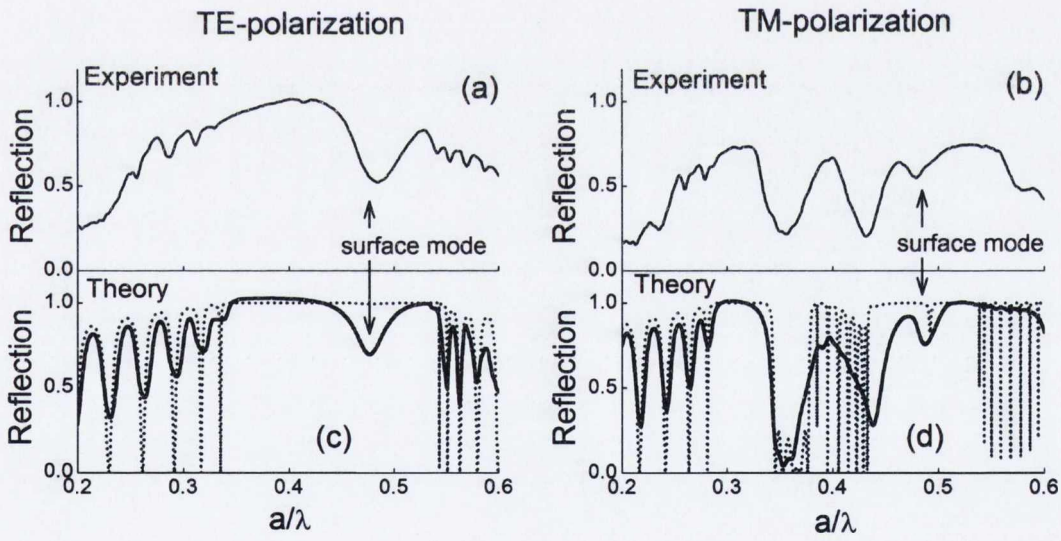

Figure 3.25: (a,b) Experimental and (c,d) theoretical reflection spectra of a 2D photonic crystal slab for TE and TE polarizations. Parameters of calculation: $r = 0.47a$, $w = 0.62a$. In panels (c,d) the dotted (solid) lines denote the reflection spectra calculated using a two-component (three-component) model. $\Delta r = 0.4\,\mu$m, $n_{abs} = 3.42 + 0.03i$.

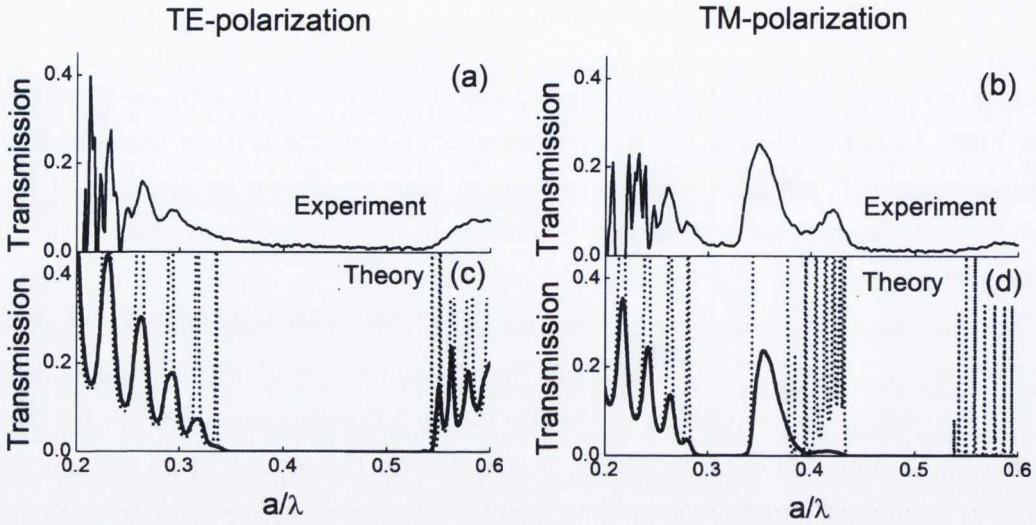

Figure 3.26: (a,b) Experimental and (c,d) theoretical transmission spectra of 2D photonic crystal slab for TE and TE polarizations. Parameters of calculation: $r = 0.47a$, $w = 0.62a$. In panels (c,d) the dotted (solid) lines denote the transmission spectra calculated using a two-component (three-component) model. $\Delta r = 0.4\,\mu$m, $n_{abs} = 3.42 + 0.03i$.

model, in particular in the amplitudes of the surface dips. As already mentioned, the reason for this disagreement may be Rayleigh scattering of light on the rough inner surfaces of the air pores. In order to simulate the scattering losses we used a three-component model (Fig. 3.9b). Another reason for the mismatch between the theoretical and experimental spectra is the deviation of the angle of incidence of light from normal. In order to take these factors into account, we calculated the reflection spectra using a three-component model for various angles of incidence in accordance with the shape of the incident light beam. Because the incident light spot has a long rectangular shape, with an aspect ratio of 4:1, we consider only those directions of incident light that are perpendicular to the axes of the air cylinders. The calculated spectra were integrated over angles of incidence from 10° to 30° in xz incidence plane with the weight coefficients specified in Ref. [66]. The result of this integration is shown in Figs. 3.25c,d by a solid line. From Fig. 3.25c and Fig. 3.25d the theoretical reflection spectra obtained are in very good agreement with the experimental spectra.

The experimental and theoretical transmission spectra of the investigated structure are presented in Fig. 3.26. The transmission spectra have regions of low-transmission, which are associated with photonic stop-bands. Since the intensity of the electromagnetic field decreases with depth of the photonic crystal slab (see Fig. 3.13), the surface-related peaks in the transmission spectra are very weak and cannot be recognized both theoretically and experimentally. The discussed above reflection dips are due to roughness losses which have peaks at the corresponding wavelengths.

Note that the calculation of the reflection and transmission spectra by the three-component model implies the use of the following fitting parameters: the width of the absorbing ring around pores, Δr, and the refractive index of the absorbing ring material material, n_{abs}. The best agreement between experimental and theoretical spectra is achieved using $\Delta r = 0.4\,\mu$m and $n = 3.42 + 0.03i$. Use of these values as fitting parameters enabled us to calculate loss sensitive features of the reflection spectra such as the amplitudes of the surface dip.

3.4.4 Discussions

It was shown in Sec. 3.4.3 that the accounting for the roughness allows to calculate the amplitude of the surface reflection dips correctly. This fact can be understood in terms of a model of asymmetric Fabry-Pérot resonator. Let us consider a homogeneous silicon layer with a refractive index $n = 3.42$ and of thickness d, terminated by two homogeneous media, namely, air and medium 2 (see inset in Fig. 3.27). The layer of silicon in this model can be considered as an interfacial layer separating medium 2 from the air. For a normal incidence of light, the reflection coefficient of the model structure is determined by the following expression:

$$R \equiv |r_0|^2 = \left| \frac{r_1 e^{-i\beta} + r_2 e^{i\beta}}{e^{-i\beta} + r_1 r_2 e^{i\beta}} \right|^2 , \tag{3.9}$$

where r_1 is the Fresnel reflection coefficient at the interface between air and silicon layer, r_2 is the reflection coefficient at the interface between the silicon layer and medium 2 and $\beta = 2\pi nd/\lambda$. From the Fresnel equations it follows that the parameter $r_1 = -0.55$. Let us take r_2 close to 1, which can be modeled by a large

refractive index of the medium 2: $n_2 = (1 + |r_2|)(1 - |r_2|)n_{Si}$. Let us take $|r_2|$ close to 1 and also take into account the π phase shift of the light reflected from the silicon/medium 2 interface. The reflection coefficient as a function of a/λ [1] is shown in Fig. 3.27a for three values of the parameter r_2, namely -0.999, -0.99, and -0.9, where minus accounts for the π phase shift of reflection discussed above. In fact, the curves from Fig. 3.27 are simply the Fabry-Pérot resonances in this asymmetric structure. The presence of the silicon interfacial layer gives rise to dips in the reflection spectrum and the amplitude of these dips increases as values of parameter $|r_2|$ decrease from unity. This situation is similar to that occurring for the 2D photonic crystal slabs investigated, where medium 2 is photonic crystal. Fig. 3.27b demonstrates that the amplitude of the surface dip in the reflection spectra of the photonic crystal slab decreases with increase of the extinction coefficient of the absorbing ring in the three-component model. It means that the amplification of the surface dip in the reflection spectra of a photonic crystal slab is caused by non-100% reflection from the photonic crystal area in the spectral range of the stop-band. In principle, the deviation of the parameter r_2 from unity for photonic crystals is due to two factors. Firstly, the number of pore rows is not infinite. The presence of surface dips in the reflection spectra of the two-dimensional photonic crystal structure without roughness (two-component model) is due to the finite thickness of the 2D photonic crystal slab. The second factor is the presence of roughness on the inner surface of the pores and other geometrical imperfections. From Fig. 3.25c, the amplitude of the surface dip due to the finite thickness of the 2D photonic crystal slab is of the order of 10^{-2}. At the same time, the experimental value of the amplitude of the surface dip is 0.25. Hence, the second factor, the losses, is predominant.

In the absence of roughness related scattering losses, some of the surface dips in the reflection spectra have a very small amplitude and are invisible on the scale of the spectra shown here. In this case, identification of the Tamm states requires measurement of the phase shift of the reflected signal. The calculated dependence $\mathrm{Im}[r_0(a/\lambda)]$ versus $\mathrm{Re}[r_0(a/\lambda)]$, where r_0 is the complex amplitude

[1] In fact, the asymmetric resonator structure is not characterized by the parameter a which denotes the period of the photonic crystal structure. However the reflection spectra are plotted with respect to a/λ to ensure a better correspondence between figures (a) and (b).

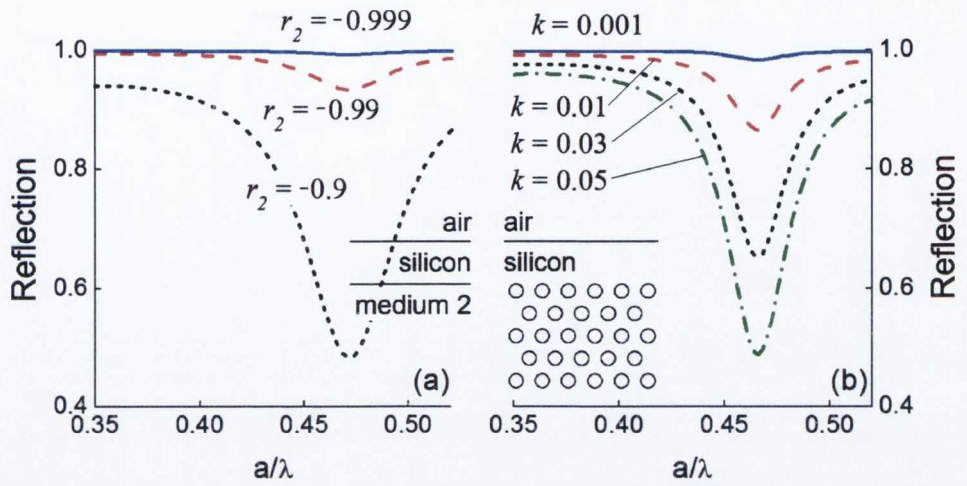

Figure 3.27: Reflection spectra (a) of the asymmetric resonator structure for different reflection coefficients, r_2, between medium 2 and silicon and (b) of the photonic crystals structure for different extinction coefficients k of the absorbing ring. Parameters of the asymmetric resonator: the thickness of silicon layer is $0.62a$ and the normal angle of light incidence. Parameters of the photonic crystal slab: $r = 0.47a$, $w = 0.62a$, $\Delta R = 0.4\,\mu$m, 11 pore rows, angle of light incidence is 20°, TE polarization.

reflectance, is shown in Fig. 3.28a for the layered asymmetric resonator and for the 2D photonic crystal slab with $r = 0.45a$, $w = 0.62a$. In these calculations the range of variation of a/λ is $0.25-0.45$ for asymmetric resonator and $0.35-0.52$ for 2D photonic crystal slab. The latter corresponds to the high reflection region of the 2D photonic crystal slab (see Fig. 3.25). From Fig. 3.12, these values of r and w correspond to the presence of one surface dip in the TE stop-band of the reflection spectrum. In both cases, the asymmetric resonator and the 2D photonic crystal slab, the relative phase of the reflected signal changes by a value of almost 2π with an increase of a/λ from initial value to the final one. It can be seen that non-100% reflection at the interface between silicon layer and medium 2 and between nonstructured silicon layer and photonic crystal area affects the absolute value of r_0 and hardly changes the phase shift of the complex amplitude reflectance. Thus, the presence of surface states in 2D photonic crystal slab can be confirmed by measuring the relative phase of the reflected signal.

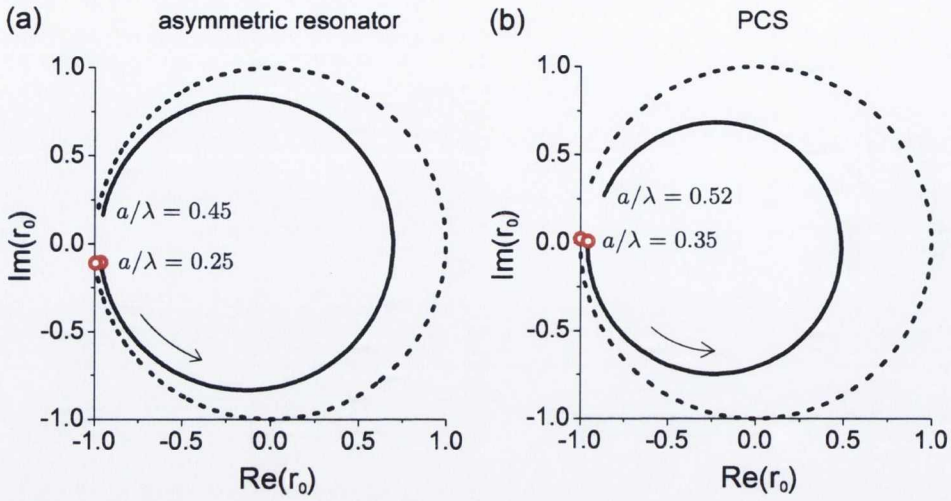

Figure 3.28: Dependence of imaginary part of the complex amplitude reflectance, $\mathrm{Im}(r_0)$, versus the real part of the complex amplitude reflectance, $\mathrm{Re}(r_0)$, for (a) an asymmetric resonator and (b) a 2D photonic crystal slab. Parameters of the structures and the incident light correspond to those in Fig. 3.27. Calculations were performed using a two-component model (dashed line) and a three-component model for $k = 0.1$ (solid line). The red circles denote the initial values of a/λ.

3.5 Conclusions

In conclusion, the reflection and transmission spectra of two dimensional photonic crystal slabs with two types of photonic crystals lattice defects have been investigated theoretically and experimentally. The presence of the homogeneous silicon interfacial layer, separating the 2D photonic crystal slab from air, gives rise to the dips within the photonic stop bands of the reflection spectra in TE and TM polarizations. The spatial distribution of the electromagnetic field in the structures investigated shows that these dips correspond to the photonic surface Tamm states. It was shown that the roughness of the inner surfaces of pores affects the amplitude of the surface-associated dips in the reflection spectra. Absolutely smooth inner surfaces of pores would make the observation of the surface modes within the stop band of the reflection spectrum impossible. Apart, the presence of the linear defect (cavity) in depth of the photonic crystal slab leads to the appearance of the allowed states in the photonic band gap. The

amplitude and the width of the cavity associated dips in the reflection spectra with this type of defect are influences by the roughness of the pores as well as by the relative spectral position of the cavity dips and the surface dips. The electromagnetic field distribution at the frequency that corresponds to the same spectral positions of the surface and cavity dips possesses the properties of both the surface mode and the cavity mode.

Furthermore, it was demonstrated that the phase of the reflected light changes by 2π when the frequency of the incident light passes the frequency of the corresponding surface mode. Thus, this mode can be observed by measurements of the phase shift upon reflection even from an ideal system without losses. A simulation of the roughness of the cylindrical surfaces of the air/silicon interface as well as the deviation of the angle of light incidence from normal enabled us to achieve a satisfactory agreement between the experimental and theoretical spectra of 2D photonic crystal slabs.

Chapter 4

Optical anisotropy of grooved silicon structures

4.1 Optical properties of grooved silicon structures (introduction)

Grooved silicon is a periodic one-dimensional structure consisting of deep trenches with vertical walls (see Fig. 4.1) and characterized by the following interesting optical structures. In the long-wavelength spectral region for $\lambda \gg$ a, where a is the lattice period, they reveal the properties of a uniaxial crystal with the high anisotropy of the effective refractive index [67, 68]. On the hand for infrared (IR)

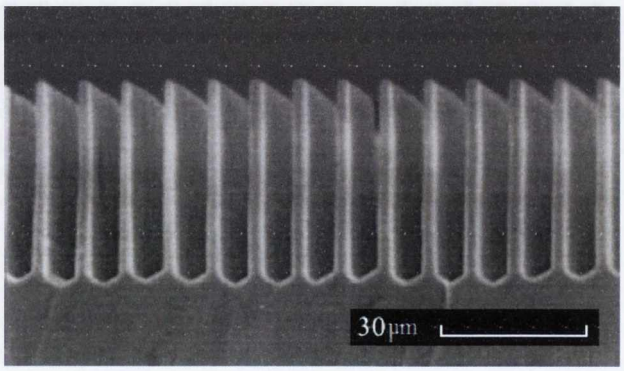

Figure 4.1: Sample of the grooved silicon structure [67].

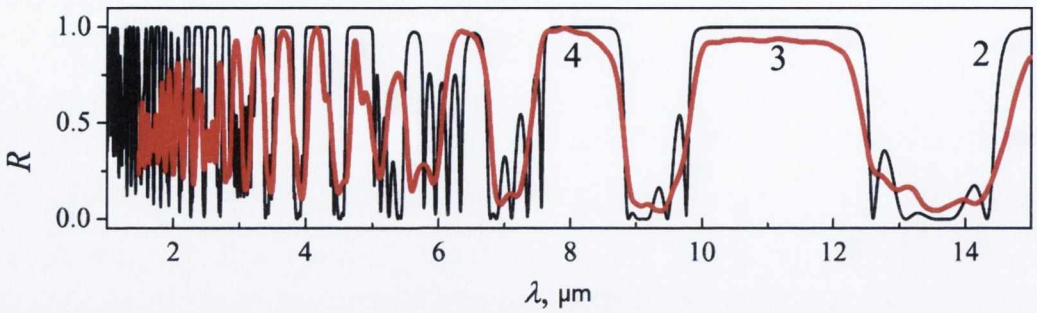

Figure 4.2: Experimentally obtained (red line) and calculated (black line) reflection spectra of grooved silicon structures with period of 7 μm and thickness of grooves of 3.3 μm [73].

light with $\lambda \approx a$, the structure possesses a properties of one-dimensional photonic crystal with broad stop bands [69, 70]. On the other hand, grooved silicon excited by a 1.06 μm laser exhibits an enhanced Raman scattering as demonstrated in [71].

4.1.1 Grooved silicon as one dimensional photonic crystal

Grooved silicon structures can be considered as one-dimensional photonic crystal in case of light propagating perpendicularly to the Si walls and having wavelength of $\lambda \approx a$ [69, 70, 72, 73]. The stop-bands of such photonic crystal are quite broad. The good quality of such photonic crystal is provided by the high optical contrast (the ratio of refractive index of the Si walls to that of the grooves) as well as by the smooth surfaces of the Si walls. Figure 4.2 shows experimental and calculated reflection spectra of grooved silicon structures for the middle IR-range for light propagating along one of the photonic crystal direction. In Ref. [72] the possibility of the shift of photonic stop-band by means of infiltration by different substances is discussed.

4.1.2 Enhancement of Raman signal from grooved silicon

The effect of enhancement of Raman scattering from grooved silicon structures was discovered for excitation wavelength of $\lambda = 1.06\,\mu$m with respect to the non-

modulated substrate [71]. In Ref. [71] the enhancement of Raman scattering was studied at excitation by visible light with the wavelengths of 488 nm and 633 nm as well as by the infrared light with the wavelength of 1064 nm under normal incidence of light beam. The collecting lens with diameter of 5 cm was placed at the distance of 2 cm from the sample

Fig. 4.3(a) shows the typical spectra of grooved silicon structure and of non-structured silicon wafer at the excitation wavelength of $\lambda = 1064$ nm. It can be seen from Fig. 4.3(a) that the shapes and spectral positions of the scattering band for the grooved Si structure and for Si wafer coincide with each other and are shifted by 520.5 cm^{-1} with respect to the excitation wavelength, that corresponds to the scattering on the bulk TO-phonons in c-Si. The intensity of Raman signal for the grooved silicon is 5 time higher than that for the non-structured silicon wafer. In case of the excitation wavelengths of 488 nm and 633 nm there was no enhancement of Raman signal observed from grooved silicon structures.

The increase of the Raman signal from grooved silicon structures can be caused by a weak localization of the excitation light within the structure. In this case the incident light penetrates into the sample and propagates mainly through the silicon walls which act as plane waveguides. In Ref. [74] the effect of the weak light

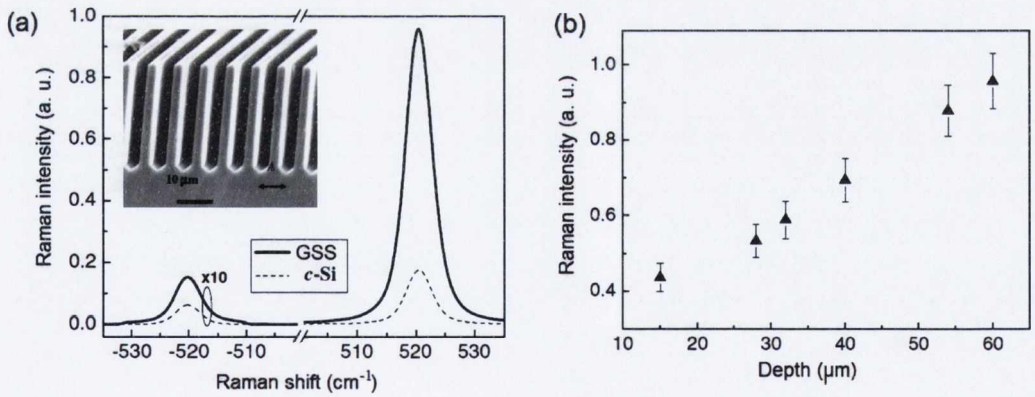

Figure 4.3: (a) The spectrum of Raman signal for the grooved silicon structure (GSS) and for the silicon wafer (c-Si). The excitation wavelength $\lambda = 1064$ nm. Investigated GSS is shown in the inset. (b) Dependence of the Raman intensity from the GSS from the depth of the grooves [71].

localization is discussed without detailed information given on the way of light propagation within the grooved structure. In work [71] the intensity of Raman scattering from grooved silicon structures was studied as a function of the groove depth (see Fig. 4.3b). It can be seen from this figure that the dependence of Raman signal from the groove depth is linear. It was concluded that this fact is the manifestation of the partial light localization in the grooved silicon.

4.1.3 Optical anisotropy of grooved silicon structures

The grooved silicon structures demonstrate the property of high optical anisotropy in the middle and far infrared range of the spectra where $\lambda > a$, where a is the lattice period. In Ref. [67] it is shown that the grooved silicon structures behaves as a negative uniaxial crystal with an optical axis parallel to the wafer plane and exhibits an extremely high optical anisotropy in the mid-IR spectral range. Indeed, the difference in the effective refractive indexes for the ordinary and extraordinary rays, Δn, is about 1.5 while the refractive indexes of anisotropic substances for various directions differs between each other by no more than 0.3 [11]. The spectral dependence of the effective refractive index of ordinary and

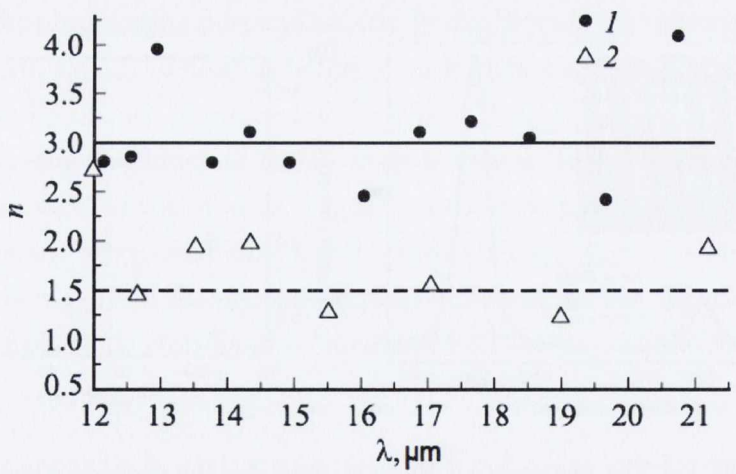

Figure 4.4: Spectral dependence of the effective refractive index of ordinary and extraordinary waves obtained from the reflection spectra of grooved silicon structures in case of normal incidence of light [67].

extraordinary beams can be found from the experimental reflection spectra and is shown in Fig. 4.4.

In work [68] transmission spectra of grooved silicon structures with 4- and 7-μm periods is studied by polarization-sensitive IR and submillimeter spectroscopy in a wide spectral range. Fig. 4.5 shows a typical transmission spectrum of a grooved Si structure in a wide IR range (20–10000 cm^{-1}) for two directions of polarization, with the electric vector parallel or normal to the grooves (curves 1 and 2, respectively). The entire spectral range can be divided into three parts:

- Far-IR range ($\nu = 20$–600 cm^{-1} or $\lambda = 500$–16 μm). In this range, the condition $\lambda \gg a$ is satisfied quite well. Hence, the periods of two type of oscillations of transmission coefficient is properly described by the effective medium model. The small period of the transmission modulation (of 8 cm^{-1}) is independent of the direction of polarization; therefore, it is related to the interference of beams in the Si substrate: $\Delta\nu_0 \approx (2Ln_{Si})^{-1}$, where $L = 170\,\mu$m is the substrate thickness and $n_{Si} = 3.4$ is the refractive

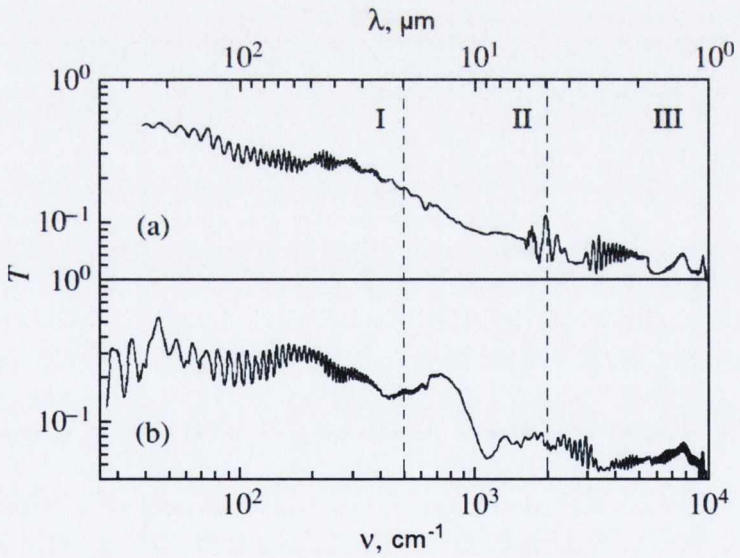

Figure 4.5: Typical transmission spectra of grooved silicon structures in the range 20–10 000 cm^{-1} for two polarization directions: (a) — parallel to the grooves, (b) — perpendicular to the grooves. [68].

index of c-Si. The larger periods of oscillations (88 cm^{-1} and 146 cm^{-1}) is related to the interference of light in the thin anisotropic grooved layer with effective refractive index which is described by the effective medium model.

- Middle IR-range ($\nu = 600$–$3\,000$ cm^{-1} or $\lambda = 16$–3 μm). In this range $\lambda \geq a$, so the spectral dependence of the effective dielectric permittivity cannot be described by the effective medium model. Hence, the calculated birefringence differs from the experimental one [67].

- In the near-IR range ($\nu = 2000$–$10000\,cm^{-1}$ or $\lambda = 3$–1 μm), where the wavelength of radiation is less than specific sizes in a grooved Si structure, evidently, the condition for effective medium approximation is not satisfied, but the approximation of the geometrical optics can be applied. In this case, the period of interference oscillations is independent of the polarization of incident light, it is determined by the interference of beams propagating across the grooves and Si walls, and is described by the relation

$$\Delta\nu = \frac{1}{L(n_{Si} - 1)}. \tag{4.1}$$

Thus, as it follows from the literature, spectra in the middle IR-region have not been described theoretically so far. The aim of the present chapter is to calculate the reflection and transmission spectra of grooved silicon samples at wavelengths of about the period of the structure and larger and compare them with experiments.

4.2 Investigated samples

Grooved silicon structures can be fabricated by different dry and wet etching methods [75, 76, 77, 78]. Methods of dry etching have high precision and resolution. They can be easily integrated into a single technological cycle. Their main advantage is that they do not depend on the crystallographic orientation of the substrate. In microstructuring a very important parameter is the aspect ratio of the depth to the width of the grooves. Etching of deep grooves using reactive

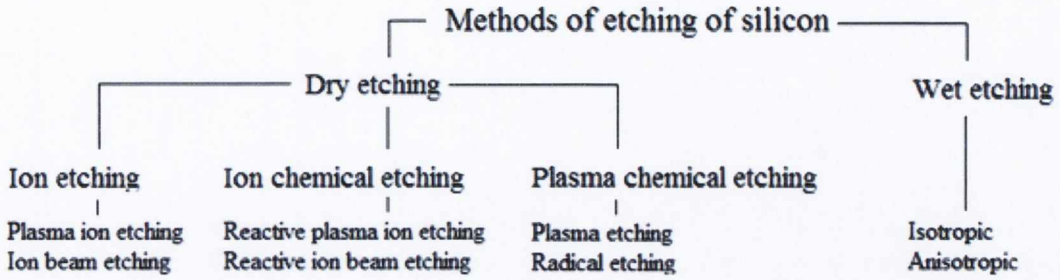

Figure 4.6: Classification of methods of silicon microstructuring.

ion etching has some specific problems. Among them are the uneven etching and cone-like shape of the taper groove, the formation of bottle-like grooves, microscopic irregularities, inclined wall grooves. In order to avoid the formation of defects one needs to make a lot of efforts to develop complex technological regimes of etching. Thus, using dry etching it is difficult to obtain deep (more than 10μm) grooves with smooth mirror like walls. The process of development of technological regimes of dry etching is very time consuming [75, 79].

The anisotropic alkali etching of (110) silicon has an advantage because it enables one to fabricate structures with almost vertical walls having the smoothest Si surface [80]. The ribs of such structures are formed by the (111) crystallographic planes, which are etched approximately 600 times slower than the (110) planes [76, 81].

In the present chapter we study grooved silicon structures fabricated on n-type (110) oriented Si wafer with a resistivity of 5 Ω·cm prepared by anisotropic etching at 70°C in a 44% aqueous solution of potassium hydroxide. The initial Si wafers were polished from both sides and their surfaces were covered by a thermal oxide or a silicon nitride layer. Then, windows for grooves were opened in this layer on the front of the Si wafer by means of photolithography. The length of these windows was 400 μm and their width was 2–4 μm, depending on the period of the structure. Grooves with walls formed by the (111) planes comprised a lattice with a period equal to 4, 5, and 6 μm for different samples. Table 4.1 presents the parameters of samples, and Fig. 4.1 shows the cross section of one of these structures. Figure 4.7 shows the schematic of a sample cut along and perpendicular to the grooves. It is known that the vertical edges of the grooves

Table 4.1: Geometrical parameters of grooved silicon structures.

Sample	Period, a, μm	Thickness of walls, d_{Si}, μm	Depth of grooves, l, μm	Total sample thickness, H, μm
24a4	4	1.0	30	200
24a5	5	1.2	30	200
24a6	6	1.4	30	200
s5	5	1.8	42	225
s6	6	2.6	42	225

obtained by anisotropic etching of Si(110) are inclined [76]. In addition, the bottoms of grooves in the studied structures are V-shaped with an apex angle of about 120° [82]. However, in our calculations, we neglect these details and assume for simplicity that the grooves are infinitely long in the direction of the y-axis and have a rectangular cross section in the xz-plane.

4.3 Experimental setup

The geometry of optical measurements is shown in Fig. 4.7. The reflection and transmission spectra of grooved Si structures were measured in polarized light with Digilab FTS-60A and FTS-6000 Fourier spectrometers in the spectral range from 450 to 6000 cm^{-1} with a resolution of 8 cm^{-1} for the $E_{\parallel}$ and $E_{\perp}$ polarizations. The electric field strength corresponding to the $E_{\parallel}$ or $E_{\perp}$ polarization is directed parallel or perpendicular to the grooves, respectively. The spectra are recorded at normal incidence of light to a sample surface.

4.4 Results and discussion

As follows from Section 2.2, to calculate the optical properties of a grooved Si

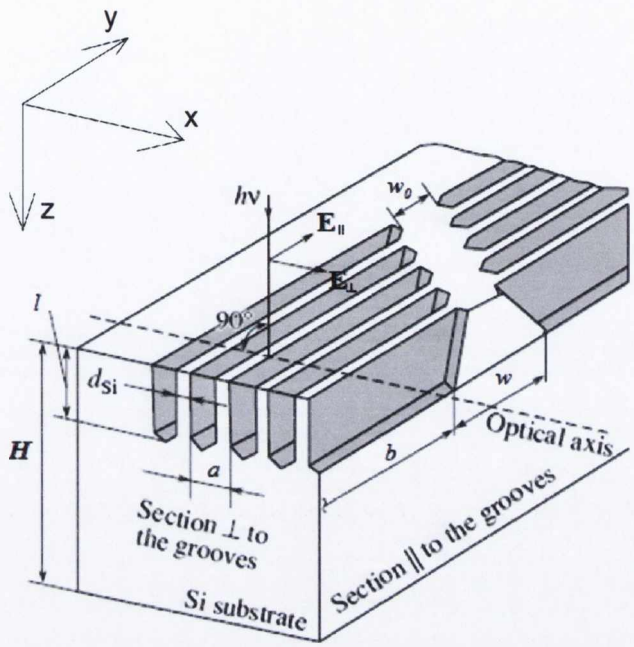

Figure 4.7: Schematic of the sample and the optical measurement: silicon substrate; $S_\parallel$ ($S_\perp$) section parallel (perpendicular) to the grooves; the dashed straight line is the normal to the silicon wall; b is the width of the grooves in the bottom part of the structure; w and w_0 are the widths of solid silicon stripes between the grooves on the surface of the sample and the groove depth, respectively.

structure for the light incident along z-direction (see Fig. 4.7), it is necessary to represent it in the form of a sequence of the layers homogeneous along the z-axis and, possibly, periodic in the direction perpendicular to the z-axis. Figure 4.8(a) shows an example of sample splitting into the layers. The structure is divided into four layers, two of which, the first and the fourth (vacuum), are semi-infinite. The second (silicon/air grooved layer) is periodic in the substrate plane and homogeneous along the z-axis, while the third layer (silicon substrate) is completely homogeneous. We selected calculated optical coefficients by neglecting the absorption of light by free carriers in silicon as well as the interaction of light with crystal lattice phonons. The reflection spectra, calculated for the described model structure, differ considerably from the experimental spectra (Fig. 4.9). The frequent oscillations in the calculated spectrum (thin gray line) are related to

Fabry-Pérot resonances on a rather thick silicon substrate ($\sim 200\,\mu$m).

To observe these oscillations in experiments, the coherence length of light should exceed at least the sample thickness, which is not fulfilled in our case. To exclude such oscillations in calculations, a substrate is usually assumed to be a semi-infinite. The corresponding calculated curve is also shown in Fig. 4.9 (thin black line). Now the characteristic frequency of the remaining oscillations of the calculated spectrum approximately corresponds to the experiment (they are related to Fabry-Pérot resonances on a grooved silicon layer, see the discussion below); however, the amplitude of these oscillations and the qualitative shape of the spectrum is still considerably different from the experimental data. This discrepancy can be explained by Rayleigh light scattering by the irregularities of the groove structure both in the modulated layer and in the intermediate "modulated part – substrate" layer consisting of V-shaped deepenings in the bottom of the grooves. This scattering can be quite considerable because the ratio of the refractive indexes of these layers is rather high. It is well known that the surface roughness introduces sufficient errors to the determination of refractive indices of

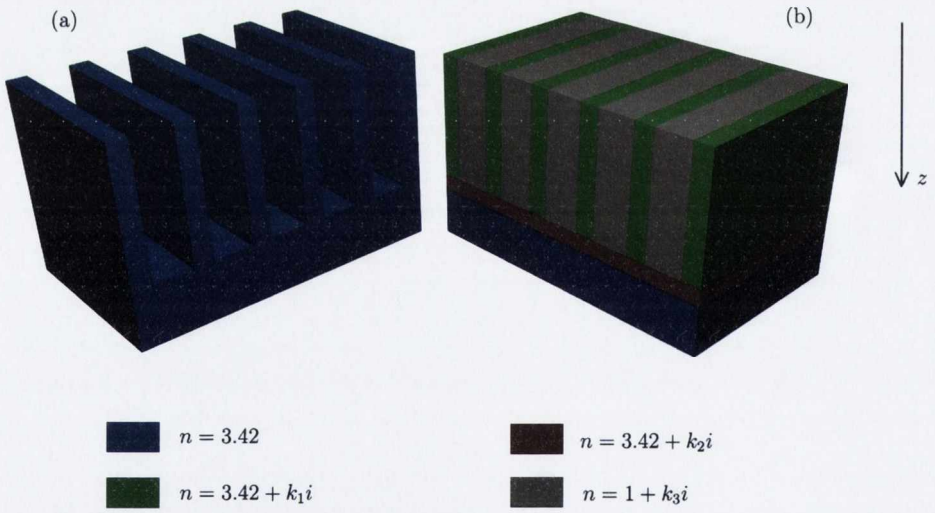

Figure 4.8: Schematics of a grooved Si structure for calculations by the scattering matrix method: (a) ideal sample model; (b) real sample model which takes into account the diffuse scattering.

materials by ellipsometry methods [4], especially to their imaginary parts. The latter is quite natural because roughnesses cause a diffuse scattering resulting in losses during the light propagation. There are many examples in the literature (see, for example [4, 52, 53, 54]) when the scattering losses on the roughness of interfaces were correctly taken into account by adding the imaginary part to the real refractive indices of transparent materials or by increasing the imaginary part of the refractive indices of absorbing materials[1]. Following this approach, we will assign complex refractive indices k_1 and k_2 to the periodic and to the intermediate layers, respectively, in silicon and k_3 to the air in periodic layer. We assume for simplicity that parameters k_1, k_2, and k_3 are independent of the wavelength of light. The resulting model structure is shown in Fig. 4.8b. The

[1]Strictly speaking, it is necessary to distinguish the perfectly periodic modulation of interfaces in a photonic crystal structure and their irregular roughness. The periodic modulations are taken into account in the scattering matrix method and do not require the addition of imaginary parts to take into account the radiation losses [9].

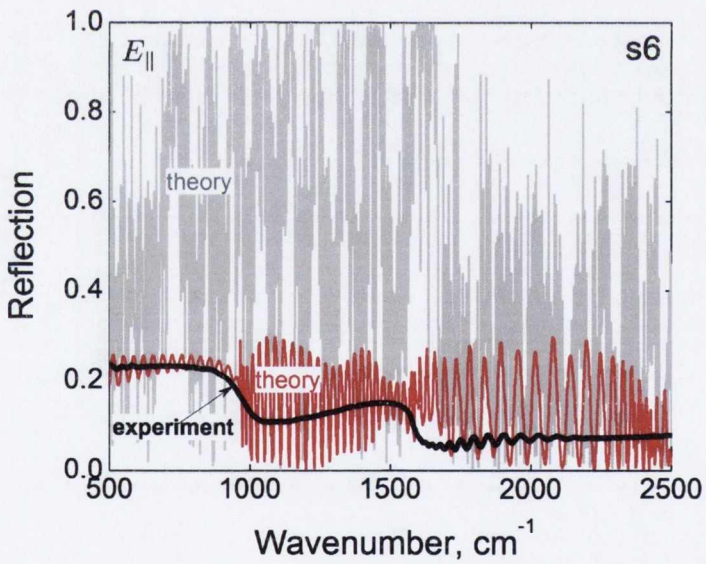

Figure 4.9: Experimental (thick line) reflection spectrum of grooved silicon sample s6 and reflection spectra calculated for ideal sample model for the cases of a finite (Fig. 4.8(a), thin gray line) and semi-infinite (thin black line) silicon substrates for the $E_{||}$ polarization of light.

thickness t of the third layer is related to the V-shaped bottom profile and depends on the groove width $t = d_{air}/2\sqrt{3}$, where $d_{air} = ad_{Si}$ is the groove width. The numerical simulation shows that the parameters k_1 and k_2 begin to make noticeable contributions to the reflection spectra at values exceeding 0.1, while k_3 for the values higher than 0.03. Calculations, performed with different values of k_1, k_2, and k_3 varied from 0.03 to 3 show that the best fit of experimental

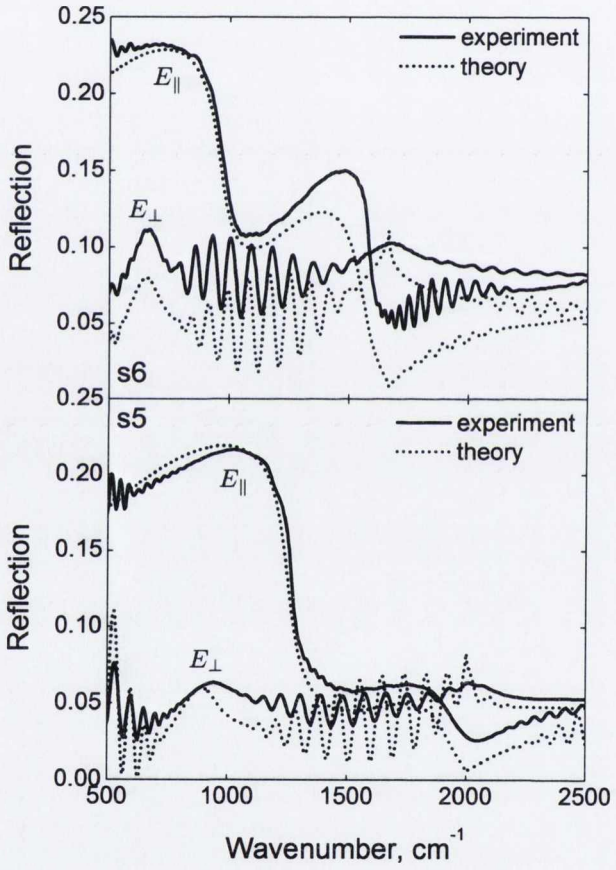

Figure 4.10: Experimental (solid lines) and calculated (dashed lines) reflection spectra of grooved silicon samples $s5$ and $s6$ for the $E_\parallel$- and $E_\perp$-polarizations. Calculations assume the presence of a scattering layer on the modulated layer-substrate interface for which the complex refractive index is set equal to 3.42 + 0.5i; the refractive index of silicon in the modulated layer is set equal to 3.42 + $0.2i$ and that of air is 1 + $0.05i$ (see Fig. 4.8b).

reflection spectra is achieved for $k_1 = 0.2$, $k_2 = 0.5$, and $k_3 = 0.05$ (see Fig. 4.10). This procedure provided a good qualitative fit of experimental reflection spectra for other samples as well (see Fig. 4.11). The obtained experimental and theoretical spectra oscillate due to the Fabry-Pérot resonances appearing during the propagation of light through a modulated layer of the structure. By using the Fabry-Pérot resonance condition

$$\Delta\left(\frac{1}{\lambda}\right) = \frac{1}{2n_{eff}l}, \tag{4.2}$$

where $\Delta\,(1/\lambda)$ is the difference of the reciprocal wavelengths of adjacent Fabry-Pérot resonances and l is the grooved layer depth, we can calculate the effective refractive indexes n_{eff} of grooved silicon (Table 4.2) in the low-frequency spectral region, where the effective medium approximation is better fulfilled.

These values can be compared with values obtained in the effective medium model for $\lambda \gg a$ [11]:

$$n^2_{eff,\|} = f n^2_{Si} + (1-f) n^2_{air} \tag{4.3}$$

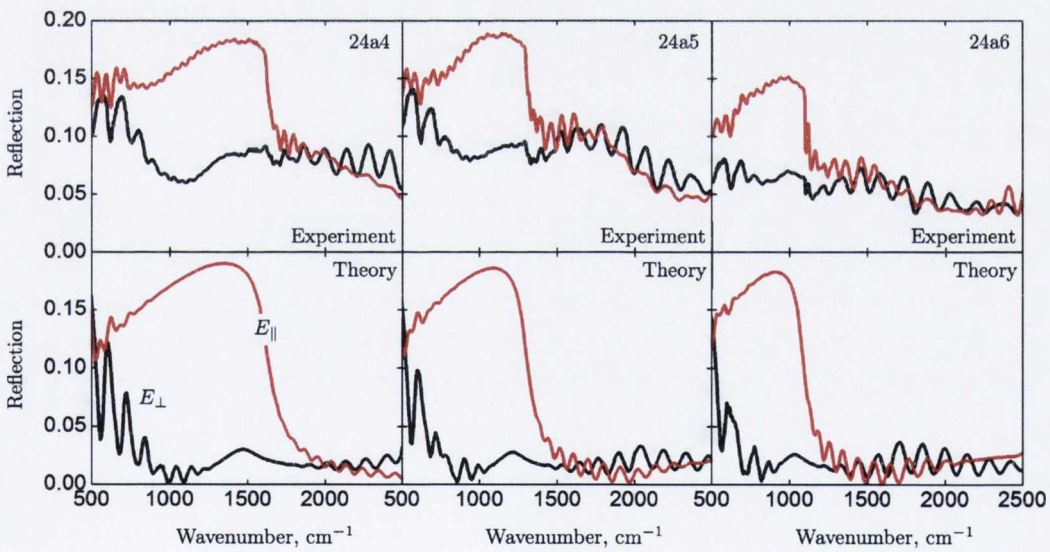

Figure 4.11: Experimental (top) and calculated (bottom) reflection spectra of samples 24*a*4, 24*a*5 and 24*a*6.

Table 4.2: Effective refractive indexes of grooved silicon calculated from the condition of Fabry-Pérot resonances for experimental reflection spectra and reflection spectra calculated by the scattering matrix method (SMM) and using the effective medium model (EMM)

$n_{eff,\parallel}$	s5	s6	24a4	24a5	24a6
Experiment	**2.4±0.1**	**3.3±0.3**	**1.5±0.1**	**1.7±0.1**	**1.5±0.1**
SMM	2.4±0.1	3.5±0.2	1.5±0.1	1.7±0.1	1.4±0.2
EFM	2.2±0.1	2.4±0.1	1.1±0.1	1.1±0.1	1.1±0.1
$n_{eff,\perp}$	s5	s6	24a4	24a5	24a6
Experiment	**1.5±0.1**	**2.6 ±0.2**	**2.7±0.1**	**3.0±0.2**	**3.2±0.3**
SMM	1.5±0.1	2.7±0.1	2.7±0.1	3.0±0.1	3.3±0.2
EMM	1.2±0.1	1.3±0.1	1.9±0.1	1.9±0.1	1.9±0.1
Δn_{eff}	s5	s6	24a4	24a5	24a6
Experiment	**0.9±0.1**	**0.7±0.3**	**1.2±0.1**	**1.2±0.2**	**1.7±0.3**
SMM	0.9±0.1	0.8±0.2	1.2±0.1	1.3±0.2	1.9±0.3
EMM	1.0±0.1	1.2±0.1	0.8±0.1	0.8±0.1	0.8±0.1

$$\frac{1}{n_{eff,\perp}^2} = f\frac{1}{n_{Si}^2} + (1-f)\frac{1}{n_{air}^2}, \tag{4.4}$$

where $f = d_{Si}/a$ is the filling fraction. It follows from Table 4.2 that the scattering matrix method allows us to calculate the effective refractive indexes of periodic silicon layers more accurately than the effective medium theory. For example, the experimental oscillation periods of the reflection coefficient (69 and 125 cm^{-1}) in the low-frequency spectral region for sample 24a4 is quite close to those calculated by the scattering matrix method (72 and 127 cm^{-1}). At the same time, the oscillation periods corresponding to Fabry-Pérot resonances in a periodical layer with a thickness of l and the refractive indexes calculated from the expressions (4.3) are 89 and 148 cm^{-1}. This difference is probably explained by the fact that the condition of applicability of the effective medium approximation $a \ll \lambda$ is not fulfilled accurately enough (in our case, $a/\lambda = 0.18 \div 0.27$).

In the high-frequency region of the reflection spectra, the electrostatic approximation condition is not fulfilled ($\lambda \sim a$). The oscillation periods of 140 and 120 cm^{-1}, calculated by the scattering matrix method in this region, are close to their experimental values of 141 and 138 cm^{-1}. At the same time, the formal use of expressions (4.2) and (4.3) gives oscillation periods of 13 and 21 cm^{-1}, which considerably differ from the experimental values.

4.5 Conclusions

Thus, we have studied the reflection and transmission spectra of grooved silicon structures with different periods and wall thicknesses. The obtained experimental spectra were compared with those calculated by the scattering matrix method. It has been shown that good agreement between experimental data and calculations by the scattering matrix method can be obtained in the modulation region by adding the imaginary parts to the refractive indexes of silicon and air to take into account the losses caused by Rayleigh scattering of light from the roughness of interfaces.

Chapter 5

Influence of the structural parameters of the layered samples on their active optical response

5.1 Enhancement of photoluminescence signal from thin layers with silicon nanocrystals

5.1.1 Optical properties of silicon nanocrystals (introduction)

Ensembles of silicon nanocrystals (SiNCs) in silica matrix have been intensively studied over the last decades because of their ability to emit light at room temperature, to be compatible with standard silicon technology and to have potential for optoelectronic applications [83, 84, 85, 86, 87, 88, 89, 90]. The photoluminescence (PL) from structures with silicon nanocrystals can originate from the relaxation of highly localized defect states or from the band-to-band recombination of quantum confined excitons in the case of good passivation of defects [83]. Regardless of the origin of the PL, the emitted light can be out-coupled, re-absorbed by SiNCs or substrate, or coupled to waveguide modes [16, 17, 18, 91, 92, 93, 94].

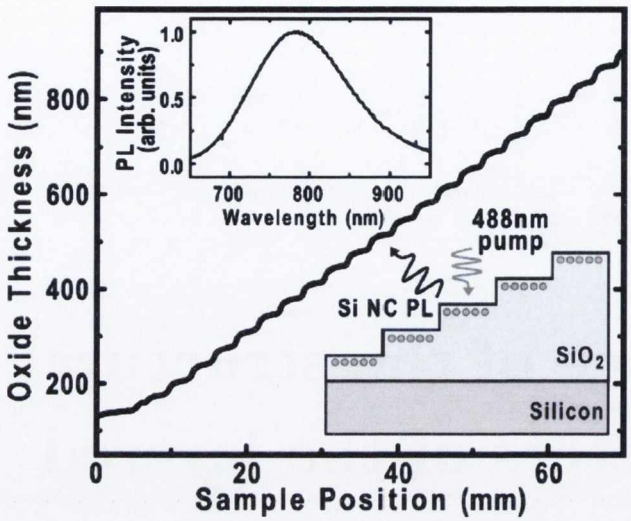

Figure 5.1: Oxide thickness along a sample as measured with spectral ellipsometry. The silicon nanocrystals form near the SiO_2-to-air interface as indicated schematically (inset, lower right). A representative nanocrystal PL spectrum shows typical near-infrared emission (inset, top left). [17].

The PL intensity of the sample strongly depends on the passive optical properties of the structure (i.e. spatial distribution of the refractive index) and the active optical properties of the emitting material (i.e. internal PL spectrum, position and orientation of point sources of PL) [15, 18, 19, 19]. Hence, the PL intensity from structures containing SiNCs can be significantly suppressed or enhanced by appropriate choice of the waveguiding properties.

An optical microcavity is a typical example of a structure which is used to enhance the light emission of a specific wavelength in a specific direction [12, 95]. A SiNCs layer placed between two Bragg mirrors formed by silica layers exhibits a PL whose intensity is 100 times stronger than that of a simple SiNCs layer placed on top of a silicon wafer [95]. The PL intensity can also be strongly enhanced by proper coupling of the emitter field with surface plasmon polaritons (SPPs) supported by thin metal films [22, 96]. This method requires a corrugated surface to compensate for the momentum mismatch between SPPs and emitted photons. Another example where the spatial distribution of refractive index plays a crucial role in propagation of light is a layered structure with deposited anti-reflection

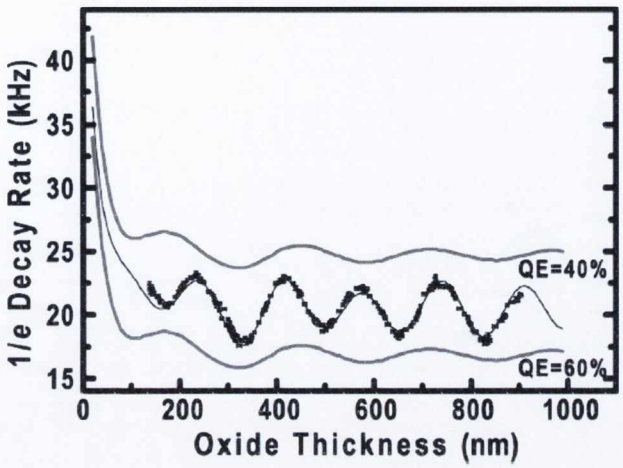

Figure 5.2: Variation of the 750 nm Kohlrausch $1/e$ decay rate with oxide thickness under constant, high power pump conditions (symbols). The periodicity in the data is explained by additional decay proportional to the local pump power (solid line). The grey drawn lines show bounding quantum efficiencies of 40% and 60%. From [17].

coating. The significant decrease in the reflection coefficient of such structures is explained by the destructive interference of light reflected from the surfaces of the sample [12].

In publication [17] the monolayer of silicon nanocrystals on the SiO_2/Si substrate was investigated. The sample with silicon nanocrystals had regions with different thicknesses of SiO_2 layer (see Fig. 5.1). It was found that the rate PL decay from silicon nanocrystals depends on the thickness of SiO_2 layer (see Fig. 5.2). This effect is explained by the change of local density of optical states and is called Purcell effect [97]. Authors of publication [17] compared experimental and theoretical PL decay rate and determined the internal quantum efficiency and internal decay rate of silicon nanocrystals. The similar results of investigation of the PL lifetime of the samples with silicon nanocrystals were reported in [21, 98, 99].

In the present study we will apply this effect to the samples containing SiNCs for increasing the proportion of light which is emitted by the SiNCs and can emerge from the sample. The aim of the work is a calculation of the PL intensity from the triple-layered structures with size controlled SiNCs as a function of layer

thicknesses as well as an experimental verification of the theoretical results.

5.1.2 Fabrication method of silicon nanocrystals

The triple-layer thin films were fabricated [1] on n-type (100)-Si substrates using an Oxford Instruments "Plasmalab 100" PECVD (plasma enhanced chemical vapor deposition) system with SiH_4 and N_2O as precursor gases. Variation of flow ratio $\Gamma = [N_2O]/[SiH_4]$ allows one to control the stoichiometry of the growing layers. Stoichiometric silicon dioxide (SiO_2) was deposited as a buffer and capping layer whereas silicon rich silicon oxynitride (SRON) was deposited as interlayer (see Fig. 5.3). Chamber pressure, total flow rate and flow ratio were kept at 500 mTorr, 730 cm^3/min and 600 respectively for stoichiometric layer of SiO_2 and 600 mTorr, 1080 cm^3/min and 5 for SRON layer. All depositions were carried out at a substrate temperature of 375°C. A deposition rate in the range of only 1.5–2.5 Å/s was achieved as confirmed by systematic ex-situ spectral ellipsometry measurements. The respective layer thickness was then controlled by varying the deposition time. It should be noted, that a deposition rate in the lower Å/s range

[1] Samples with silicon nanocrystals were fabricated by D. M. Zhigunov in the laboratory of M. Zacharias (Albert Ludwigs University Freiburg, Germany)

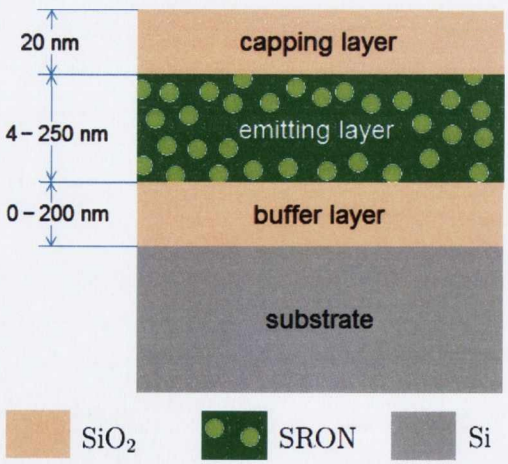

Figure 5.3: Schematic presentation of the investigated structures with silicon nanocrystals. SiNCs are shown by circles.

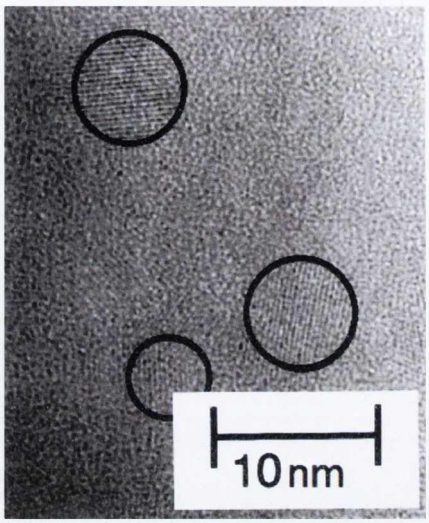

Figure 5.4: TEM image of silicon nanocrystals in silicon dioxide matrix [100].

is mandatory for precise superlattice depositions. Furthermore, we confirmed by extensive ellipsometry wafer mappings that the essential layer homogeneity in the subpercent range can be achieved over the whole 4 in. wafer for the above deposition parameters. The corresponding stoichiometry for the SRON layer was chosen to be $SiO_{1.0}N_{0.22}$. The composition of the layers was determined by X-ray photoelectron spectroscopy (XPS) with a PHI Quantum 2000 (Physical Electronics) XPS spectrometer. Subsequently, all samples were annealed for 1 hour in a high purity N_2 atmosphere at 1150°C. The annealing was carried out in a quartz tube furnace equipped with a turbomolecular pump and an electronically controlled pressure regulation. The furnace tube was first evacuated to 1×10^{-6} mbar in order to avoid any SiNC oxidation by residual oxygen in the annealing atmosphere. Then, a N_2 gas flow of $50\,cm^3/min$ was established at a constant pressure of 1050 mbar. The heating rate for all experiments was fixed to 10 K/min enabling a slow hydrogen effusion during the heating up which is mandatory to avoid cracks in the films. The annealing of the samples at 1150°C lead to formation of silicon nanocrystals in SiO_2 matrix, as is shown in Fig. 5.4. The diameter of silicon nanocrystals was found to be 3.9 ± 0.7 nm. Further details on the sample preparation technique can be found elsewhere.

In the present study three different sets of samples with SiNCs were fabricated

Table 5.1: Geometrical parameters of the samples with silicon nanocrystals.

	Thickness of capping layer	Thickness of inter-layer	Thickness of buffer layer
Series A	20 nm	30 nm	0–200 nm
Series B	20 nm	4–250 nm	25 nm
Series C	5 nm	5 nm	0–100 nm

(see Table 5.1). For the first set of samples the thickness of the SiO_2 buffer layer was varied from 0 to 200 nm, while the thicknesses of interlayer and capping layer were fixed to 30 and 50 nm. On the contrary, the second set of samples was characterized by variable thickness of the SRON layer in the range from 10 to 250 nm, while the thicknesses of the SiO_2 layers were constant with 25 nm for the buffer and 50 nm for the capping layers. For the third series of sample the thickness of the SiO_2 buffer layer was varied from 0 to 100 nm, while the thicknesses of interlayer and capping layer were fixed to 5 nm.

5.1.3 Interference enhancement of photoluminescence signal in structures with silicon nanocrystals

The light emission by SiNCs is a quantum mechanical process with a random spatial emission of the respective photons, but the optical behavior of the emitted light can be modeled using classical electromagnetism [15, 16, 17, 18, 19]. In order to calculate the PL intensity from the samples containing the SiNCs we use the optical model described in Section 2.1.2. According to this model one considers the ensemble of emitting SiNCs as a system of chaotically oriented oscillating electrical dipoles. The amplitude of oscillation of a dipole is proportional to the electric field strength of excitation light at the position of a dipole. The PL intensity from the SiNCs is approximated by the intensity of the out-coupled emission of such oscillating dipoles.

Each layer within the model structure is assumed to have smooth, parallel

interfaces and a certain thickness (Fig. 5.3). The SRON interlayer is considered as a homogeneous isotropic layer with an effective dielectric permittivity $\tilde{\varepsilon}_2$. The emitting dipoles are located on planes which are uniformly distributed over this layer. The number of planes is proportional to the thickness of the interlayer. The propagation of the plane waves of excitation light and the plane waves emitted by oscillating dipoles is simulated by the transfer matrix method (Section 2.1.1. For the calculation, the dielectric permittivities of Si and SiO_2 are taken from the literature [101]. The values of the effective dielectric permittivity of the SRON layer at different wavelengths were determined by means of ellipsometry measurements. The values determined were, $\tilde{\varepsilon}_2 = (2.11 + 0.15i)^2$ at 325 nm, $\tilde{\varepsilon}_2 = (1.88 + 0.019i)^2$ at 488 nm, $\tilde{\varepsilon}_2 = (1.84 + 0.007i)^2$ at 633 nm, and $\tilde{\varepsilon}_2 = (1.82 + 0.0025i)^2$ at 890, 930 and 940 nm. All PL intensities were calculated at normal angle of collection. The angles of incidence of the excitation light were 10° for 325 nm, 47° for 488 nm and 39° for 633 nm. Laser beams were *s*-polarized for excitation wavelengths of 325 nm and 488 nm and *p*-polarized for 633 nm. The PL intensity of a sample with SiNCs depends on three geometrical parameters, namely, the thicknesses of the capping, inter- and buffer layers, d_{cap}, d_{int} and d_{buf}, respectively. In the first stage of simulation, the intensity of the PL intensity was calculated for the thickness of buffer layer varied from 0 to 200 nm whereas the thicknesses of capping layer and interlayer were fixed and equal to 50 nm and 25 nm respectively. The calculations were performed for excitation wavelengths of $\lambda_{ex} = 325$ nm, 488 nm and 633 nm and the corresponding emission wavelengths of $\lambda_{PL} = 890$ nm, 930 nm and 940 nm in accordance with peak position of experimentally obtained PL spectra. The calculated and experimentally observed PL intensities are shown in Fig. 5.5a.

As can be seen from this figure, an excellent agreement was found between theoretical and experimental results. Note that the calculation method does not imply the use of any fitting parameters. In case of the 325 nm excitation wavelength the function of PL intensity on d_{buf} has two local maxima in the investigated range (50 nm and 133 nm), and for 488 nm and 633 nm wavelengths only one maximum exists at 75 nm and 100 nm, respectively. It is worth noting that the PL intensities from a structure with an optimized thickness of the buffer layer are about 20 times stronger than those obtained from the structures without a buffer layer.

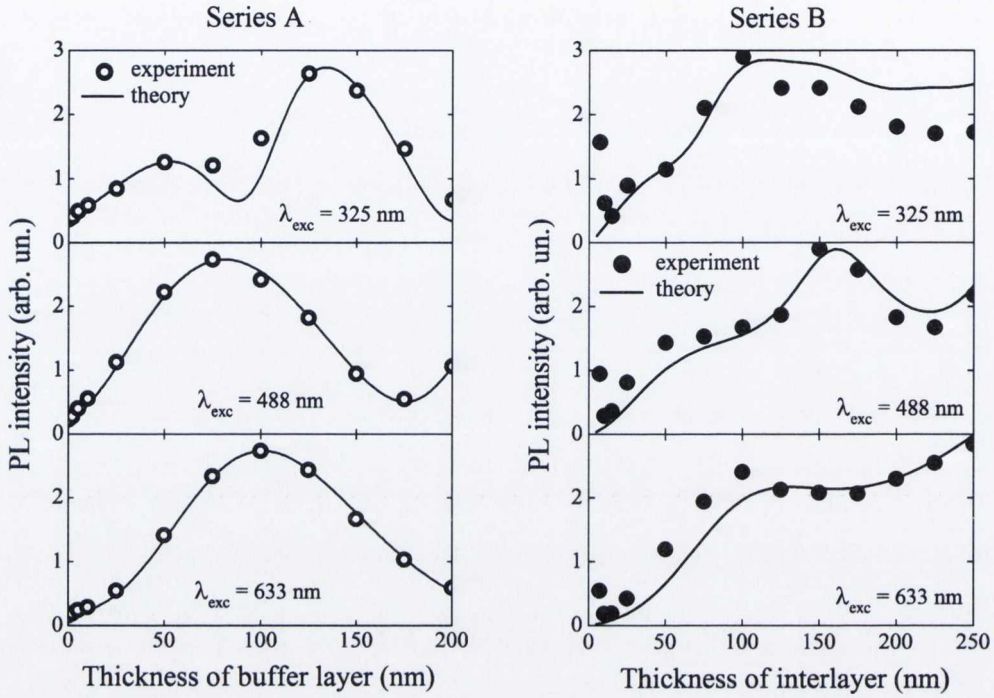

Figure 5.5: Calculated (lines) and experimental (circles) PL intensities of the SiNCs samples as a function of the thickness of the buffer layer (series A) and the thickness of interlayer (series B) for different excitation wavelengths.

From the optical point of view, the process of PL consists of two stages. The first stage is the in-coupling of the excitation wave into the structure with the SiNCs. All specific features of this stage, such as reflection and transmission coefficients, interference, multireflection, etc., are determined by the excitation wavelength. The second stage is the emergence of the PL light from the sample. All characteristics of this stage are determined by the PL wavelength, i.e. by the size of the Si nanocrystals. In order to distinguish the contribution of the first stage on the resulting PL intensity, we calculated the average value of the square of the amplitude of the electric field strength over the SRON layer as a function of buffer layer thickness for different excitation wavelengths (Fig. 5.6). The calculated dependence is periodical due to the Fabry-Pérot resonances appeared while passing the excitation light through the layered structure. We will call this

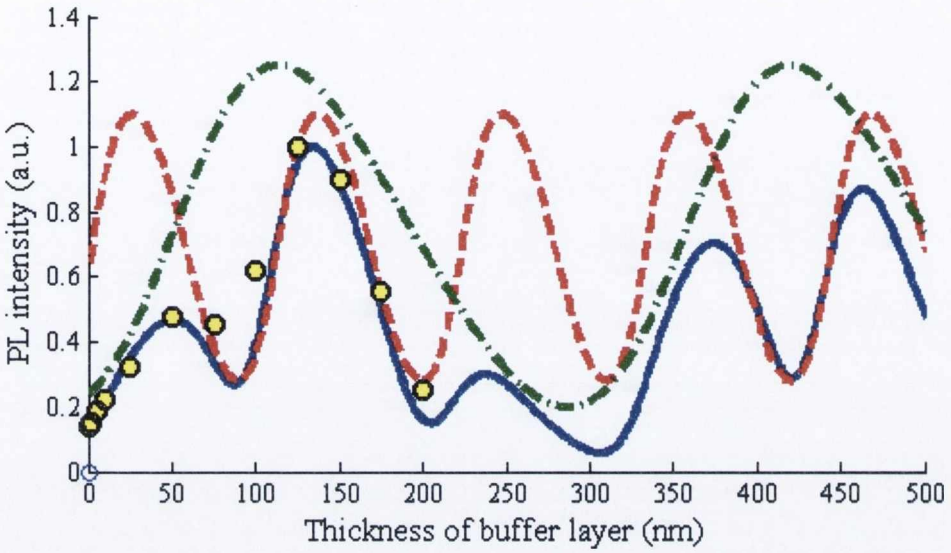

Figure 5.6: Comparison of in-coupling (red dashed line) and out-coupling (green dash-dotted line) efficiencies with calculated (blue solid line) and experimental (dots) PL intensities of the SiNCs samples as functions of buffer layer thickness. $\lambda_{exc} = 325\,\text{nm}$.

dependence as an in-coupling efficiency. In order to reveal the contribution of the second stage, we calculated the PL intensity for the specific case when the amplitude of oscillation of the dipole is constant and does not depend on the excitation electric field strength (Fig. 5.6).

This function is periodical too because of the Fabry-Pérot resonances appeared while the propagating of the photoluminescent light through the sample. In fact, a calculated PL intensity for this case is an out-coupling efficiency. Note that the periods of the in-coupling and out-coupling efficiencies can be found from the condition for two nearest Fabry-Pérot resonances for plane waves traveling through the buffer layer:

$$\Delta d_{buf} = \frac{\lambda}{2n_{buf}\cos\varphi_{buf}}, \tag{5.1}$$

where λ is the wavelength of excitation or PL light, n_{buf} is the refractive index of buffer layer, φ_{buf} is the angle of PL or excitation light propagation in the buffer layer. The initial phases and amplitudes of the periodical functions of

in-coupling and out-coupling efficiencies are determined by the refractive indexes and thicknesses of all the layers as well as by the substrate material and can be found by the transfer matrix method and the model of oscillating dipoles (Section 2.1).

Comparing the behavior of the PL intensity and the in-coupling efficiency we can conclude that the distance between two peaks in the experimentally obtained dependence from Fig. 5.6a (at $\lambda_{ex} = 325\,\text{nm}$) is mainly determined by the Fabry-Pérot resonances for excitation light, i.e. excitation wavelength. From the other side, the function of the out-coupling efficiency is the envelope curve to the experimentally verified dependence of the PL intensity as a function of the buffer layer thickness. Thus, the ratio between the amplitude of the peaks in the experimental dependence (see Fig. 5.6a) is mainly determined by the period of the function of out-coupling efficiency, i.e. PL wavelength. The behavior of the PL intensity versus the thickness of buffer layer from excitation wavelengths $\lambda_{ex} = 488\,\text{nm}$ and $\lambda_{ex} = 633\,\text{nm}$ are explained the similar way.

Now we are in the position of optimization of PL intensity when both capping and buffer layer thicknesses are varied. In this case the behavior of the resulted PL intensity can also be described in terms of the in-coupling and out-coupling efficiencies which are two-dimensional functions of buffer and capping layer thicknesses. Figure 5.7 shows these functions as well as the resulted PL intensity for the interlayer thickness of 25 nm. The in-coupling and out-coupling efficiencies are periodical functions and their periods are determined by equation (5.1). In Fig. 5.7 we can see only one period of out-coupling efficiency in the presented range of the buffer and capping layer thicknesses. For the investigated samples with SiNCs, when $d_{int} = 25\,\text{nm}$, the optical width of interlayer, $n_{int}d_{int}$ is approximately 6.5 times less than the excitation wavelength and about 18 times less than the PL wavelength. Hence, the resulted PL is roughly the product of the in-coupling and out-coupling efficiency. However, we calculated the exact values of PL intensity by the method described in Section 2.1.2. From Fig. 5.7c we can see that the optimal thickness of buffer layer is $\approx 120\,\text{nm}$ which provide relatively high PL intensity for all thicknesses of capping layer. However at $d_{cap} \approx 0, 80, 200$ and 300 nm the PL intensity has its local maxima. The experimentally observed PL intensities are denoted by white dots in Fig. 5.7 and are in a very good

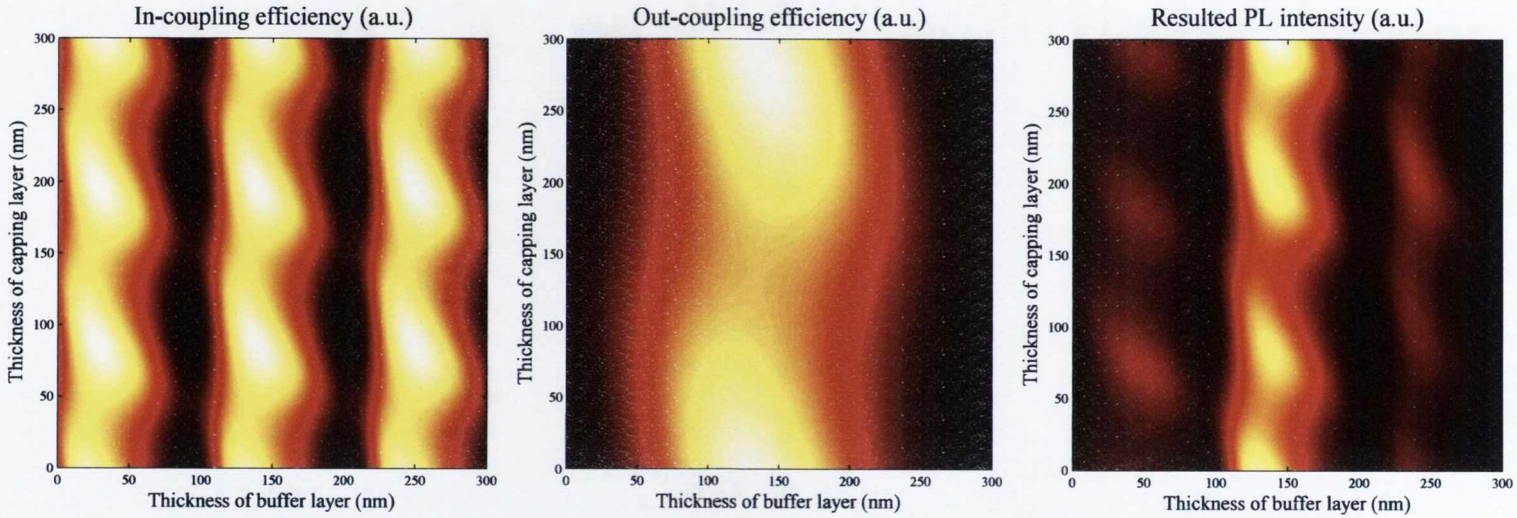

Figure 5.7: In-coupling efficiency (a), out-coupling efficiency (b) and resulted photoluminescence intensity (c) of the samples with silicon nanocrystals as two-dimensional functions of buffer and capping layer thicknesses. Excitation wavelength $\lambda_{exc} = 325\,\text{nm}$, photoluminescence wavelength $\lambda_{PL} = 890\,\text{nm}$, thickness of the layer with silicon nanocrystals $d_{int} = 25\,\text{nm}$. Periods of the functions of in-coupling and out-coupling efficiencies are precisely described by the condition of Fabry-Pérot resonances: $\Delta d = \frac{\lambda}{2n\cos\varphi}$, where d, n and φ are the thickness, refractive index and angle of light propagation for the capping layer or buffer layer.

agreement with theoretical data.

The experimental and calculated PL intensities for the series B of samples with variable SRON layer thickness are shown in Fig. 5.5b. It can be seen that dependencies of the PL intensity are neither a linear or monotonically increasing functions of the thickness of the interlayer, but have local maxima and minima. The position of local maxima is $d_{buf} = 100\,\text{nm}$ for the excitation wavelengths $\lambda_{ex} = 325\,\text{nm}$ and 633 nm, and $d_{buf} = 150\,\text{nm}$ for $\lambda_{ex} = 488\,\text{nm}$. This result is quite unexpected, since the number of SiNCs in the sample is proportional to the thickness of SRON layer and, at first sight, the PL intensity should also increase monotonically as a function of the SRON interlayer thickness. It is obvious now that such a statement is untrue, and it is possible, for example, to obtain more intense luminescence from a thinner emitting layer but enclosed with optimized buffer and/or capping layers. Note, that the agreement between calculated curves and experimental data plotted in Fig. 5.5b is not as good as for the series with different buffer layer thickness. This is most likely caused by thickness dependent changes in the SiNCs ensemble (e.g. SiNCs size distribution) which were not taken into account by our simple model [102]. As in case of series A, the features of the dependencies of PL intensity on the thickness of interlayer can be explained by Fabry-Pérot resonances for both excitation and PL lights.

From Figs. 5.5 and 5.7 it follows that the PL intensity of the samples with SiNCs is determined mainly by the inter- and buffer layer thicknesses whereas the contribution of the capping layer thicknesses is less important. Let us calculate the PL intensity for d_{int} varying from 0 to 250 nm, d_{buf} varying from 0 to 200 nm and fixed d_{cap} at a value of 50 nm. The theoretically evaluated PL intensities are shown in Fig. 5.8 as a two-dimensional function of buffer and interlayer thicknesses. For excitation with $\lambda_{ex} = 325\,\text{nm}$ the function has three local maxima in the investigated range of buffer layer and interlayer thicknesses. The local maximum at $d_{buf} = 50\,\text{nm}$, $d_{int} = 100\,\text{nm}$ is the most interesting from the experimental point of view because the total sample thickness is the smallest. The simulated PL intensity curves for $\lambda_{ex} = 488\,\text{nm}$ and 633 nm have two local maxima and the most interesting ones are observed at $d_{buf} = 75\,\text{nm}$, $d_{int} = 125\,\text{nm}$ for $\lambda_{ex} = 488\,\text{nm}$ and $d_{buf} = 75\,\text{nm}$, $d_{int} = 75\,\text{nm}$ for $\lambda_{ex} = 633\,\text{nm}$. The white dots in Fig. 5.8 represent experimental data (PL intensities of series A and B)

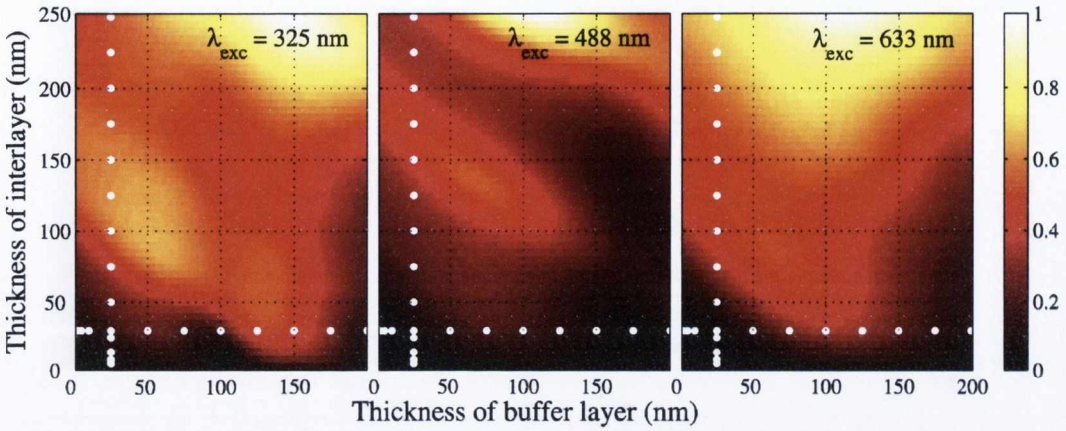

Figure 5.8: PL intensity as a function of interlayer and buffer layer thicknesses calculated using a model of oscillating dipoles. The white dots represent experimentally obtained data. The color scale on the right shows the calculated PL intensity.

which are in excellent agreement with the theory.

Dependencies shown in Fig. 5.6 enable us to determine quantitatively the contribution of interferences of excitation and PL lights to the observed enhancement of PL intensity. As can be seen from Fig. 5.6, the ratio of in-coupling efficiency at $d_{buf} = 133\,\text{nm}$ to in-coupling efficiency at $d_{buf} = 0\,\text{nm}$ for $\lambda_{exc} = 325\,\text{nm}$ is

$$\frac{I_{in}(d_{buf}^{max})}{I_{in}(0)} = 1.52. \tag{5.2}$$

The corresponding value for the out-coupling efficiency is

$$\frac{I_{out}(d_{buf}^{max})}{I_{out}(0)} = 4.97. \tag{5.3}$$

Hence, the contributions of the interferences of excitation and PL lights to the total enhancement of PL signal at $\lambda_{exc} = 325\,\text{nm}$ are related to each other as 1.52:4.97 and equal to 23% and 76%. For $\lambda_{exc} = 488\,\text{nm}$ the contributions of interferences of excitation and PL lights are 38% and 62% and for $\lambda_{exc} = 633\,\text{nm}$ are 35% and 65% respectively.

The PL intensity of the samples with silicon nanocrystals depends on the thicknesses of all three layers. Thus for each fixed thickness of the sample, d, one

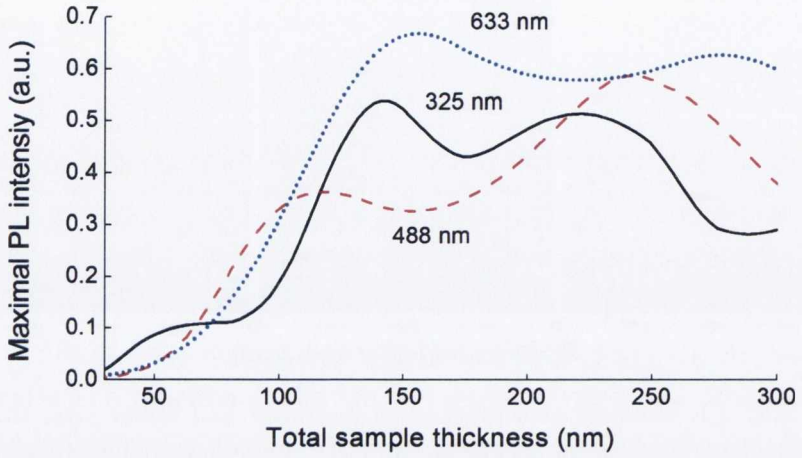

Figure 5.9: The highest PL intensity of the samples with silicon nanocrystals as a function of the total thickness of the sampele.

calculate the triplet of parameters (d_{cap}, d_{int}, d_{buf}), such as $d_{cap} + d_{cap} + d_{cap} = d$, that provides the maximal PL intensity. Fig. 5.9 shows the functions of the highest intensity from the total thickness of the sample, d.

For the excitation wavelength of 325 nm the highest intensity is achieved at the total sample thickness of 141 nm and the thicknesses of layers of $d_{cap} = 9\,\text{nm}$, $d_{int} = 78\,\text{nm}$, $d_{buf} = 54\,\text{nm}$. For the excitation wavelength $\lambda_{exc} = 488\,\text{nm}$ the optimal thickness of the sample is 117 nm and the respective thicknesses of layers are $d_{cap} = 9\,\text{nm}$, $d_{int} = 45\,\text{nm}$, $d_{buf} = 63\,\text{nm}$. Finally, for $\lambda_{exc} = 633\,\text{nm}$, the optimal thickness of the sample is 156 nm and the thicknesses of layers are $d_{cap} = 9\,\text{nm}$, $d_{int} = 78\,\text{nm}$, $d_{buf} = 69\,\text{nm}$.

Up to now we calculated the PL intensity for the fixed PL wavelength. At the same time, the photoluminescence occurs at all the wavelengths in some spectral range. It is obvious that the condition for Fabry-Pérot resonance (Eqn. (5.1)), which is satisfied for the wavelength of maximal PL intensity in the spectrum, is not met for other wavelengths. This fact leads to the shortening of the photoluminescence spectrum as well as to the shift of its peak position in comparison to the internal PL spectrum. Let us simulate the dependence of the PL peak position on the thickness of the buffer layer.

In order to exclude the influence of the inhomogeneous excitation and PL out-coupling conditions on the shape of PL spectrum we choose the thickness of the layer with silicon nanocrystals to be equal to 5 nm. This thickness corresponds to exactly one layer of spherical silicon nanocrystals, all of which are located in the same dielectric environment. The capping layer is 5 nm, the excitation wavelength is 325 nm, the angle of incidence is 0°, the angle of collection is 10° and the oscillating dipoles are located at the center of the active layer.

We start from the in-coupling efficiency which is presented in Fig. 5.10a as a two-dimensional function of the PL wavelength and the thickness of the buffer layer. It is obvious that the in-coupling efficiency does not depend on the PL wavelength. Then, we plotted the function of out-coupling efficiency Fig. 5.10b which changes with increase of both the PL wavelength and the thickness of the buffer layer. The resulted PL intensity in the approximation of homogeneous internal PL spectrum is shown in Fig. 5.10c and is approximately equal to the product of the in-coupling and out-coupling efficiencies for the investigated samples with silicon nanocrystals. In calculation we, however, used the exact method (method of oscillation dipoles), explained in Section 2.1.2. We call the dependence shown in Fig. 5.10c as an *excitation efficiency*. In fact, the results shown in Figs. 5.5–5.9 are related to the excitation efficiency, however in assumption of the fixed PL wavelength, the resulted PL intensity and the excitation efficiency are equivalent. In order to simulate how the spectrum of out-coupled photoluminescence changes with increase of the buffer layer thickness, we have to account for both the shape of the internal PL spectrum and the excitation efficiency. For convenience, we approximate the internal PL spectrum by the following Gaussian function:

$$I(\lambda) = I_0 e^{-\frac{(\lambda - \lambda_0)^2}{\sigma}}, \tag{5.4}$$

where $\lambda_0 = 850\,\text{nm}$ is the central wavelength and $\sigma = 7000$ is the parameter responsible for the full width at half maximum (FWHM). The internal PL spectrum is shown in Fig. 5.11a. The product of the internal PL spectrum and the excitation efficiency is the out-coupled photoluminescence (Fig. 5.11b). It can be seen from Fig. 5.11b that the out-coupled PL spectra have the maxima at approximately 850 nm but the exact peak position depends on the thickness of

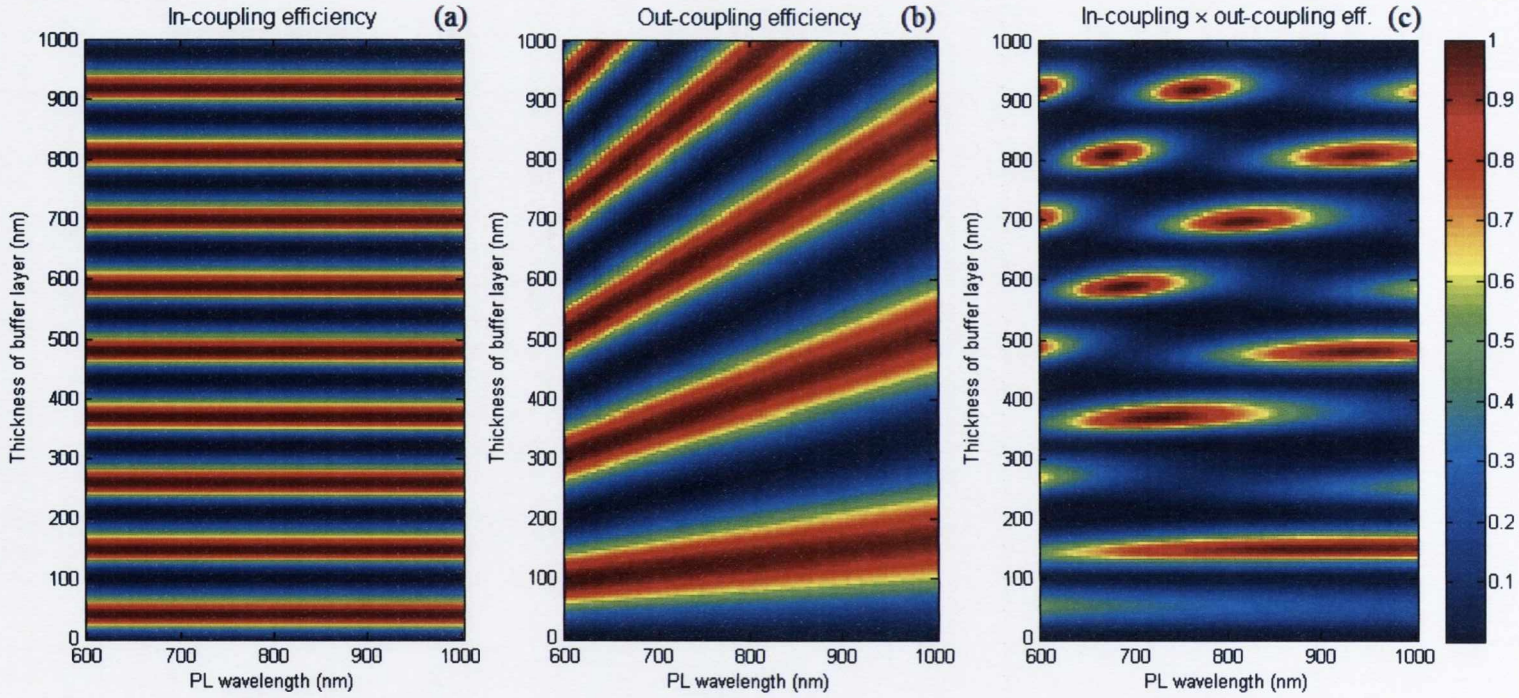

Figure 5.10: (a) In-coupling efficiency, (b) out-coupling efficiency and (c) resulted PL intensity in the approximation of homogeneous internal PL spectrum (excitation efficiency).

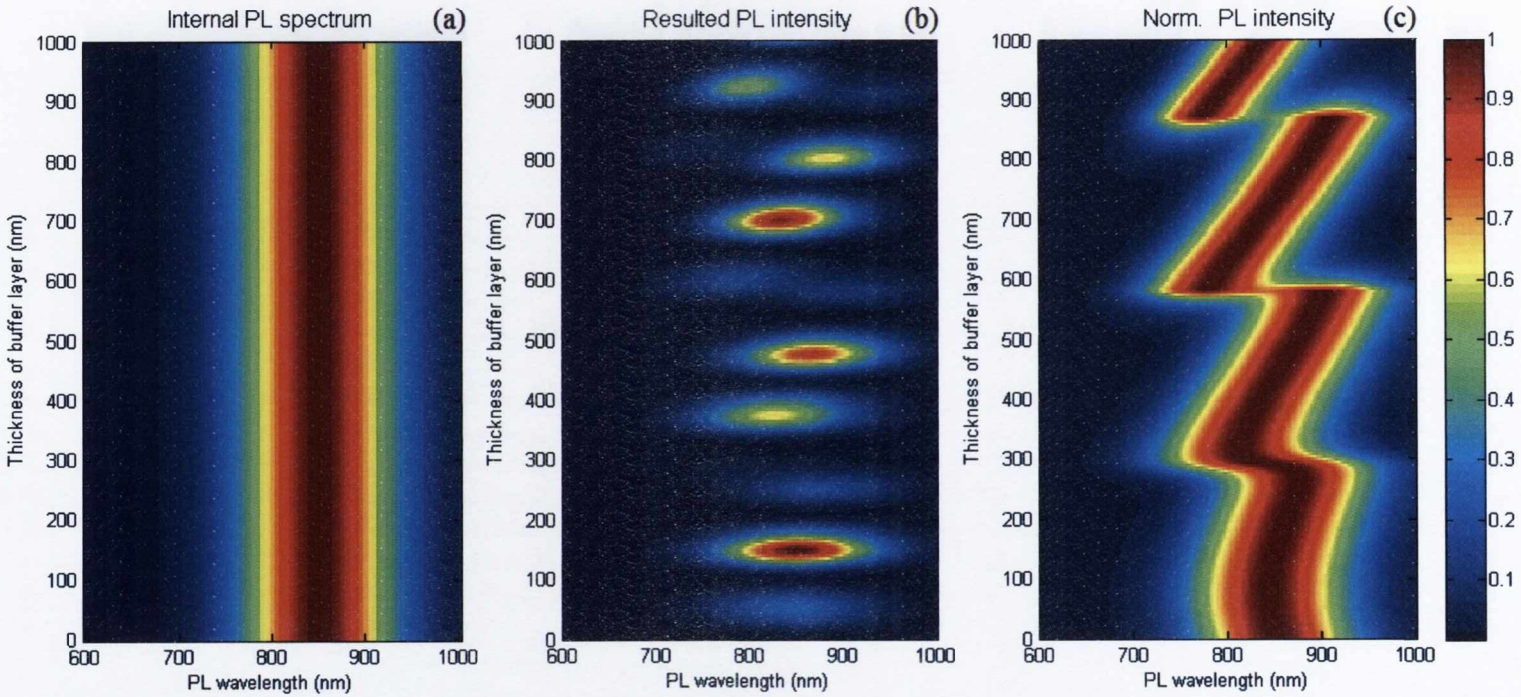

Figure 5.11: (a) Internal PL spectrum, (b) out-coupled PL intensity and (c) normalized out-coupled PL intensity.

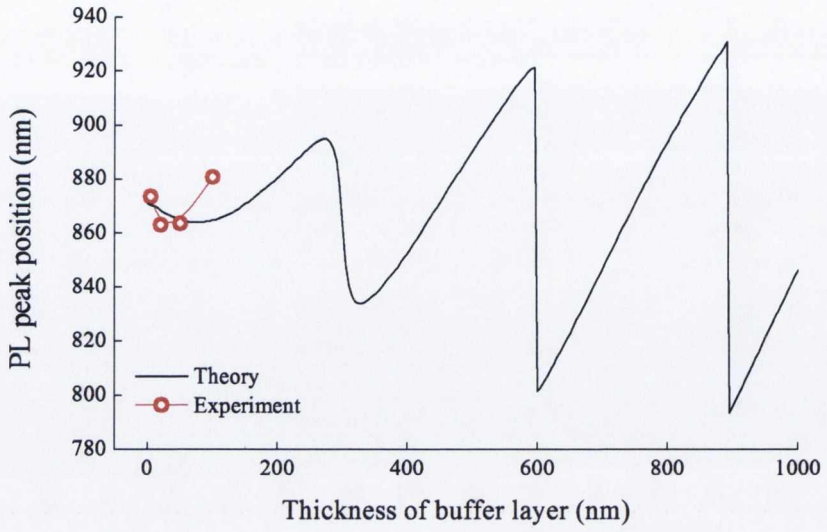

Figure 5.12: Theoretical (line) and experimental (dots) dependence of the PL peak position on the thickness of buffer layer for the series C of the sample. The parameters of the internal PL spectrum are $\lambda_0 = 870\,\text{nm}$, $\sigma = 7000$.

the buffer layer. The normalized PL spectrum as a function of the thickness of the buffer layer is shown in Fig. 5.11c. From Fig. 5.11c it can be seen that the PL peak position is between 780 nm and 910 nm depending on the thickness of the buffer layer. For the buffer layer thicknesses of $\approx$ 580 and 870 nm the PL spectrum has two peaks. We would like to emphasize that the described effect is attributed to the interferences of the excitation light as well as of the PL light propagated in the buffer layer. Fig. 5.12 shows the theoretical dependence of the peak position on the thickness of buffer layer calculated for the samples of series C and the corresponding experimental data are shown by circles. It can be seen from Fig. 5.12 that there is some agreement between theoretical and experimental curves however for detailed comparison more samples have to be analyzed. At the present moment we can say that the better agreement is a question of an appropriate choice of the central wavelength of the internal PL spectrum λ_0 and the parameter σ.

In conclusion, we performed a quantitative analysis of the processes of excitation of PL light and its subsequent emergence from the SiNCs containing sam-

ple. It was found that the PL intensity of the investigated samples is strongly influenced by the Fabry-Pérot resonances appearing during the propagation of excitation and PL light through the sample. The enhancement of the photoluminescence intensity by a factor of 20 can be observed for a structure with optimized buffer layer thickness compared to non-optimized one. Theoretically predicted PL intensities are in very good agreement with results of the photoluminescence measurements for the corresponding structures with silicon nanocrystals.

5.2 Resonance enhancement of Raman signal from one-dimensional periodical structures of porous silicon

5.2.1 Introduction

Porous silicon has been intensively studied over the last decades [71, 103, 104] because it offers new opportunities for control of light propagation. Porous silicon (por-Si) structures can be fabricated by electrochemical etching, which is relatively fast and low cost technology. During the fabrication process, the effective refractive index of por-Si can be controlled by the etching current density and etching time [105]. This facilitates the possibility of utilization of porous silicon for construction of new optical elements.

Raman scattering is a well known technique for characterization of porous silicon. Regardless of the Raman scattering efficiency and the orientation of the crystallographic planes, the scattered light can be out-coupled, absorbed by por-Si layers or by Si substrate, coupled to the waveguide modes or re-scattered by the inhomogeneity of the refractive index distribution in porous silicon [15, 16, 106]. The latter process is responsible for the Rayleigh scattering. The contribution of all of these mechanisms strongly depends on the spatial distribution of the refractive index of not merely a single layer but of the entire structure.

There are a number of publications [20, 107, 108, 109, 110, 111, 112, 113] where the intensity of Raman scattering from silicon or other substances is enhanced by proper choice of the refractive index distribution within the sample. In Refs. [107, 109, 110, 111] the interference enhancement of Raman scattering from single or double layered structures is studied. In Ref. [108] the surface-plasmon-palariton-assisted Raman enhancement was demonstrated for adsorbates even on transition metals with higher intrinsic damping. In Ref. [20] the enhanced Raman scattering from copper phthalocyanine thin film in the attenuated total reflection arrangement was observed. It was shown that the enhancement of Raman signal in this case is explained by strong electromagnetic fields induced in the copper phthalocyanine film upon excitation of the half-leaky guided modes.

In the present study we performed the investigation of intensity increase in Raman scattering of one-dimensional photonic crystal consisting of the periodical layers of porous silicon of different porosities. The local density of optical states in photonic crystals increase in the spectral region near the photonic band gap (PBG) [1]. We expect that this phenomenon can significantly change the intensity of Raman scattering from photonic crystal sample.

The purpose of the present study is a theoretical and an experimental investigation of the influence of the photonic band gap of the por-Si-based one-dimensional photonic crystal on the intensity of Raman scattering.

5.2.2 Experimental details

Multilayered samples of porous silicon were fabricated by electrochemical etching of (100)-oriented n-type crystalline Si (c-Si) wafers with a specific resistivity of 10–20 Ohm·cm in an electrolyte based on mixture of hydrofluoric acid (HF wt. 48% in water) and ethanol (C_2H_5OH) in the ratio of 1:1. The etching current density was periodically changed from 20 to 100 mA/cm^2 to form a sequence of

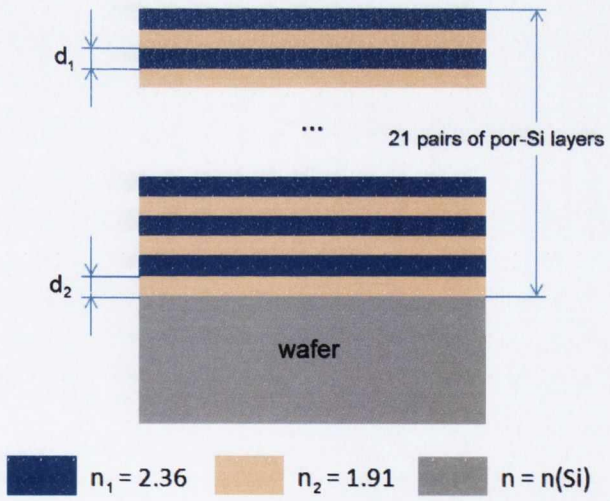

Figure 5.13: Model structure of one-dimensional photonic crystal sample made of porous silicon. Layers of por-Si, shown by blue and pink colors, are considered as homogeneous isotropic layers with refractive indexes 1.91 and 2.36, respectively.

Table 5.2: Parameters of the porous silicon structures.

Name of sample	Type of wafer	Effective refractive index of layers		Thickness of layers, μm		Number of layer pairs
		n_1	n_2	d_1	d_2	
NPS-1	n-Si	2.36	1.91	90	120	21
NPS-2	n-Si	2.36	1.91	100	130	21

por-Si layers with alternating porosity. The obtained multi-layered structures (see Fig. 5.13) were mesoporous with typical size of the Si nanocrystals of tens of nanometers. After fabrication, por-Si samples were dried in ambient atmosphere for several days. The structural parameters along with labels of the fabricated samples are given in Table 5.2. Reflection spectra in the near-infrared (NIR) range were measured by using an FT-IR spectrometer Bruker IFS-66 v/S. The Raman spectra were measured with the same spectrometer using an FRA-106 attachment, under excitation with a continuous-wave (CW) Nd:YAG laser at $9398\,\mathrm{cm}^{-1}$ ($1.064\,\mu$m) with power up to 150 mW. Measurements of the Raman scattering were performed in the backscattering geometry with a spectral resolution of $2\,\mathrm{cm}^{-1}$. The excitation light was s-polarized and focused to a spot with a diameter of about 1.5 mm. The angle of incidence of excitation light was varied from 0° to 60 °. All experiment were carried out at room temperatures.

5.2.3 Experimental results

The reflection spectra of the prepared multilayered structures of porous silicon are shown in Fig. 5.14. It can be seen from Fig. 5.14 that the structures demonstrate the photonic band gap in the near infrared spectral range and therefore act as one-dimensional photonic crystal. The position of the photonic band gap was different for both samples. The experimental reflection spectra were well fitted by theoretical calculations using the transfer matrix method [11].

Fig. 5.15 shows the angular dependences of the Raman scattering intensity for

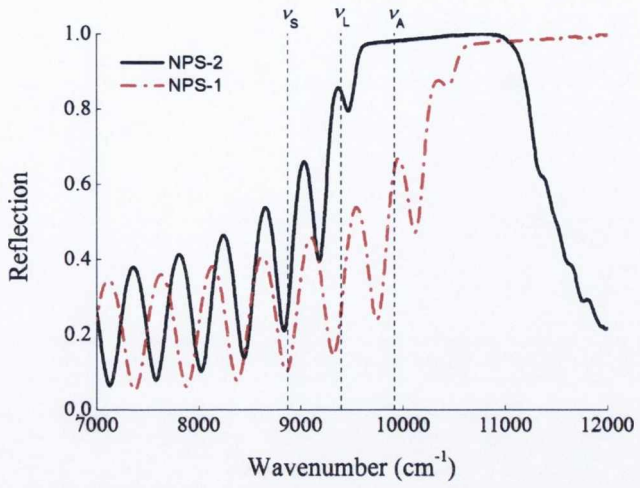

Figure 5.14: Reflectance spectra of the investigated multilayered structures measured at normal incidence of light. Vertical dashed and dotted lines indicate the spectral positions of the employed laser radiation (ν_L), Stokes (ν_S), and anti-Stokes (ν_A) components of the Raman scattering.

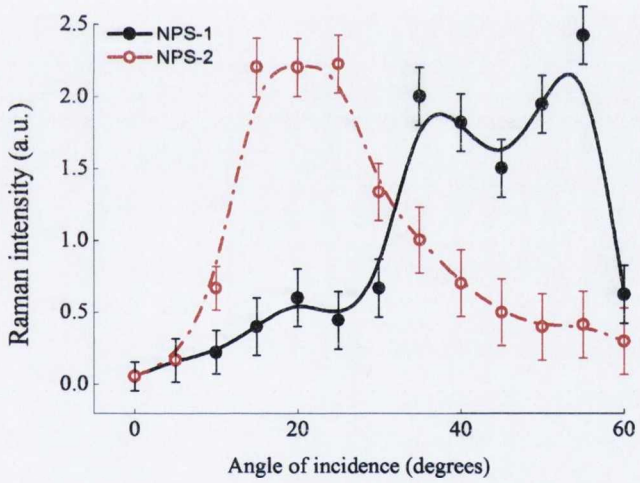

Figure 5.15: The dependences of the intensity of Stokes component for the investigated multilayered structures versus the angle of incidence of the excitation light. The angular dependences are corrected with respect to those measured for homogeneous por-Si layers.

the Stokes component of the investigated porous one-dimensional photonic crystals. The scattering intensities were normalized with respect to those measured

for homogeneous por-Si layers at the same angle of light incidence. Maximum intensity of the Raman scattering is observed at certain angles of incidence when the Stokes component frequency ($\nu_S = 8879\,\mathrm{cm}^{-1}$) falls at the edge of the PBG.

5.2.4 Theoretical model

The spontaneous Raman scattering is a quantum mechanical process with a random spatial distribution of the respective photons, but the optical behavior of the scattered light can be modeled using classical electromagnetism [15, 16, 17, 18, 19]. In order to calculate the Raman intensity from the multilayered samples we use the optical model reported in Refs. [15, 18]. According to this model one considers the ensemble of elementary scatterers as a system of chaotically oriented oscillating electrical dipoles. The amplitude of oscillation of a dipole is proportional to the electric field strength of excitation light at the position of a dipole. The intensity of Raman scattering from the samples is approximated by the intensity of the out-coupled emission of the oscillating dipoles.

Each layer of porous silicon within the model structure is considered as homogeneous isotropic layer with a certain effective dielectric permittivity and a certain thickness. The effective dielectric permittivity of each layer can be found by using effective medium theory [11] and is determined by the porosity of the layer. The model structure is shown in Fig. 5.13. The emitting dipoles are located on planes which are uniformly distributed over each layer. The number of planes in each layer is proportional to its thickness and to the filling fraction of silicon. The propagation of the plane waves of excitation light and the plane waves emitted by oscillating dipoles is simulated by the transfer matrix method [12]. The spectral dependence of the dielectric permittivity of Si is taken from the literature [101]. All Raman intensities were calculated at normal angle of collection. In calculations, the redshift of the Stokes component of Raman signal of 520 cm^{-1} is taken into account.

Note that the described theoretical approach enables us to calculate the Raman intensity by accounting for the absorption of the scattered light by c-Si from the wafer or by porous layers and for the coupling to the waveguide modes. At the same time, the contribution of the Rayleigh scattering of excitation light and

the Raman scattered lights in the porous layers is neglected.

5.2.5 Results of simulations

The calculated intensity of Raman scattering of the multilayered structure is shown in Fig. 5.16 by solid line as a function the wavenumber of excitation light in dimensionless units $\nu_{exc} = (2n_1d_1+n_2d_2)/\lambda_{exc}$. For these units the center of the fundamental (1st) PBG is located at $\nu_{exc} = 1$ for normal incidence of excitation light. For comparison, the reflection spectrum of this multilayered structure is shown on the same graph along with the Raman intensity of the homogeneous layer of porous silicon of the same thickness. The reflection spectrum has a region of high reflection which corresponds to the photonic stop-band of the multilayered structure. The dependence of the Raman intensity of homogeneous layer versus excitation wavenumber is a periodical function. This periodicity is due to the appearance of the Fabry-Perot resonances in the homogeneous layer. In contrast to the periodically changing intensity of homogeneous layer, the intensity of multilayered structure has two local peaks of high amplitude A and D located at $\nu_{exc} = 0.92$ and 1.13 respectively. At the same, there are two peaks of smaller amplitude (B and C) at $\nu_{exc} = 1.08$ and 0.97 one of which (B) is located at the edge of the photonic band gap, another one (C) is within the photonic band gap. For explanation of the origin of the described peaks, we calculated first the function of in-coupling efficiency as an average value of the square of amplitude of the electric field strength of excitation light over the multilayered structure (solid line in Fig. 5.17). In fact, the in-coupling efficiency is a relative intensity of excitation light which penetrates inside the structure. Then we calculated the function of Raman out-coupling efficiency (dashed line in Fig. 5.17) as an intensity of Raman scattered light from the sample for the special case when the amplitude of dipole oscillation does not depend on the electric field strength of the excitation light. The out-coupling efficiency is a relative intensity of Raman scattered light which is born inside a structure and emerges it. The local maxima of the function of in-coupling efficiency correspond to the local minima of the reflection spectra and vice versa. Hence, the local maxima A and B, which are located on the edge of the photonic band gap, are due to the resonant penetration

of light inside the structure. The function of out-coupling efficiency is blueshifted by a value $\Delta\nu_{exc} \approx 0.05$ ($520\,\mathrm{cm}^{-1}$) with respect to the spectral position of the photonic band gap. The local maxima C and D are due the resonant out-coupling of Raman light from the multilayered structure.

Considering the spectral position of the local maxima A–D with respect to that of the photonic band gap enables to understand the difference in the amplitude of these peaks. Indeed, at the local maximum B, the excitation light penetrates resonantly into the structure and the intensity of scattered light inside the structure is high. However, the frequency of Stokes component of the Raman light is within the photonic band gap. Thus, at maximum B the scattered light does not emerge the structure effectively but is absorbed by the mechanisms described in Introduction. This fact explains why the amplitude of the local maximum B is relatively low. At the maximum C, the situation is opposite. The scattered light is supported by Fabry-Perot modes and emerges the sample resonantly. At the same time, in the local maximum C, the penetration depth of excitation light is low because its wavenumber is inside the photonic band gap. Thus, the amplitude

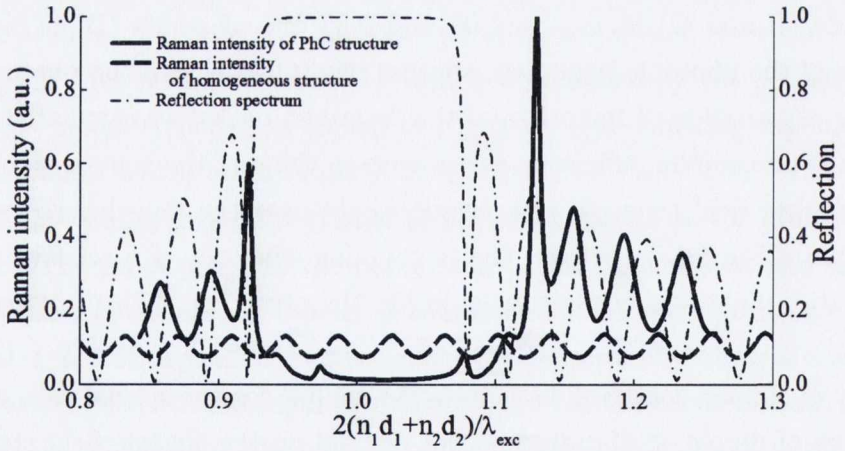

Figure 5.16: Intensity of Stokes component of Raman scattering of the model structure, shown in Fig. 1 (solid line), and of the homogeneous layer of por-Si with the thickness of multilayered structure and the refractive index of 2.36 (dashed line) as a function of the excitation wavenumber. The reflection spectrum of the model multilayer structure is shown by dotted line.

of the maximum C is low too. For the local maxima A and D, the wavenumbers of both excitation and scattered light are not within the photonic band gap. Furthermore, for the maximum A, the excitation light penetrates into the layered structure resonantly, and for the maximum D, the scattered light emerges the sample resonantly. These facts explains the enhancement of Raman signal for wavenumbers of excitation light at $\nu_{exc} = 0.92$ and 1.13.

5.2.6 Discussions

As shown in Sec. 5.2.2, during experimental investigations the Raman scattering was excited by the light with fixed wavelength of $9398\,\mathrm{cm}^{-1}$. The thicknesses of porous silicon layers and their porosity were chosen in such a way that the excitation wavelength is located near the photonic stop-band. In contrast to the experiment, the described theoretical dependencies are calculated for the varying excitation wavenumber. In the experiment, in order to shift the edge of the

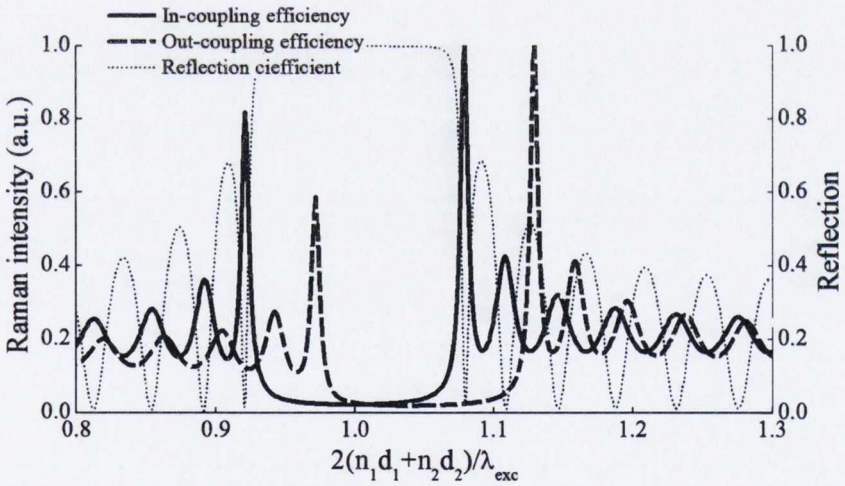

Figure 5.17: Solid line: calculated average value of square of amplitude of electric filed strength of excitation light (in-coupling efficiency). Dashed line: calculated Raman intensity for the special case when amplitude of the oscillation of electric dipoles does not depend on the electric field strength of excitation light (out-coupling efficiency). Dotted line: reflection spectrum from the model multilayer structure.

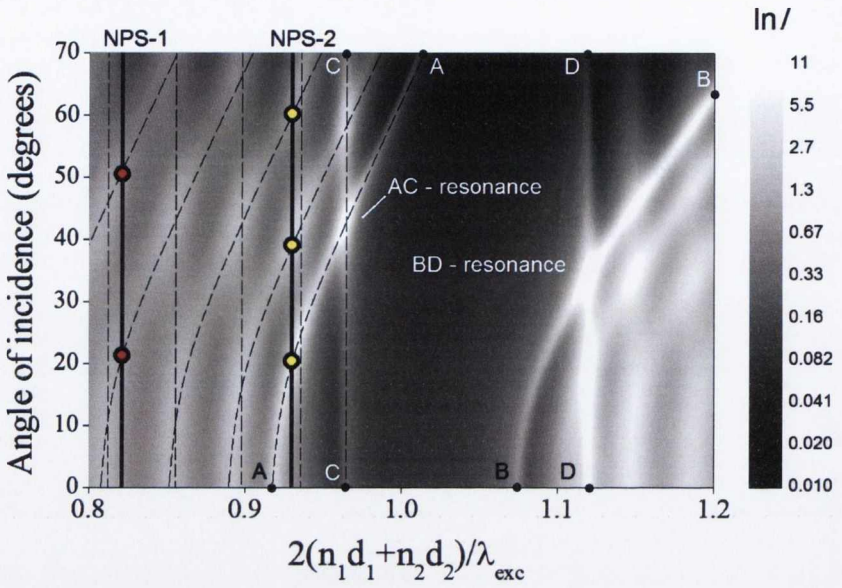

Figure 5.18: Raman intensity of the multilayered structures of porous silicon as a function of the excitation wavenumber and the angle of incidence of excitation light. Vertical black solid lines denote values of the parameter $\nu_{exc} = 2(n_1 d_1 + n_2 d_2)/\lambda_{exc}$ which correspond to the samples NPS-1 and NPS-2. The gray scale on the right shows the correspondence between the gray shade and the natural logarithm of Raman intensity.

photonic stop-band with respect to the position of the excitation wavelength, the angle of incidence was changed from 0° to 60°. The spectral shift of the photonic band gap was about 650 cm^{-1} towards higher wavenumbers for the angle of incidence increasing from 0° to 60°. In order to study the influence of the angle of excitation light incidence on the spectral positions of the described peaks A, B, C and D, we calculated the intensity of Raman scattering as a function of two parameters, namely, the excitation wavenumber in dimensionless units and the angle of incidence. The results of these calculations are shown in Fig. 5.18. The calculated function has the local maxima and minima which are formed by two types of resonances in the investigated structure. The resonances of the first type change their spectral position with increasing the angle of incidence. The spectral positions of the resonances of the second type are fixed. As it follows from the results presented in Sec. 5.2.5, it follows that the local maxima A, B,

C and D in Fig. 5.16 correspond to the initial spectral positions of the described resonances of the first and the second type. The resonances of the first type, including peaks A and B, are related to the resonant in-coupling of the excitation light into the sample. The resonances of the second type, including peaks C and D, are related to the resonant out-coupling of the Raman light from the sample. As can be seen from Fig. 5.18, the function of Raman intensity has the local peaks where the resonances of the first and the second types are intersected. In the local maxima denoted as "AC-resonance" and "BD-resonance" the theoretical intensity of Raman scattering is the highest. In these maxima the excitation light penetrates resonantly into the sample and the Stokes component of Raman light emerges the sample resonantly too. It means that the case of a double resonance is realized.

In order to compare the results of theoretical simulations with the experimental data, let us analyze the calculated Raman intensity as a function of the angle of incidence at fixed values of the dimensionless parameter $\nu = 0.83$ and 0.93 which correspond to the samples NPS-1 and NPS-2 (see vertical black lines in Fig. 5.18). It can be seen from Fig. 5.18 that for $\nu = 0.93$ and for increasing the angle of incidence of excitation light from 0° to 70° we obtain three local maxima at approximately 20°, 40° and 60° (shown by circles in Fig. 5.18). The corresponding experimental maxima for the sample NPS-2, taken from Fig. 5.15, are 20°, 40° and 55°. The Raman signal for angles of incidence lower than 15° for $\nu = 0.93$ is weak because for these angles of incidence the excitation wavelength is within the photonic band gap. For $\nu = 0.83$ the theoretical resonances are located at $\approx 20°$ and 50°. The corresponding experimental maxima for the sample NPS-1 are 20° and 55°. Note that the experimentally observed enhancement is attributed to the resonances of type A which is the case of resonance penetration of excitation light.

5.2.7 Conclusions

In conclusion, we performed a quantitative analysis of the processes of the Raman scattering and its subsequent emergence from the por-Si-based multilayered samples. It was found that the Raman intensity of the investigated samples

strongly depends on the spectral position of the excitation light with respect to the photonic stop-band and can be enhanced by a factor of 10. The effect of the enhancement of Raman scattering is explained either by resonant penetration of the excitation light into the sample or by resonant out-coupling of the scattered light from the sample or both. The experimentally observed enhancement relates to the case of resonant penetration of the excitation light.

5.3 Influence of the buffer layer properties on the intensity of Raman scattering of graphene

5.3.1 Introduction

Graphene is a one atom thick layer with honeycomb lattice made of carbon atoms (Fig. 5.19). Graphene has attracted a lot of interest since its discovery in 2004 due to its unique physical properties. Namely, graphene is a two-dimensional semiconductor with a zero-width band gap [114]. Quasi-particles in graphene are mathematically described by the Dirac-type Hamiltonian [114]. The high crystalline quality and high-career mobility make graphene a promising material for future electronics. The exceptional properties of monolayer graphene, however, are not always appropriate for the practical applications of graphene in integrated circuits or interconnects. On the contrary, few layers of graphenes have more suitable properties for integration in microelectronics. For example, transverse electric fields in bilayer and fewlayer graphene can open band gaps up to 0.2 eV, which is crucial for the operation of field-effect transistors [115]. In addition, few layers of graphene provide a better transparent conductive electrode due to the lower sheet resistance and is less susceptible to the effects of substrate impurities due to interlayer screening [116, 117]. Thus, knowledge of how electrical, ther-

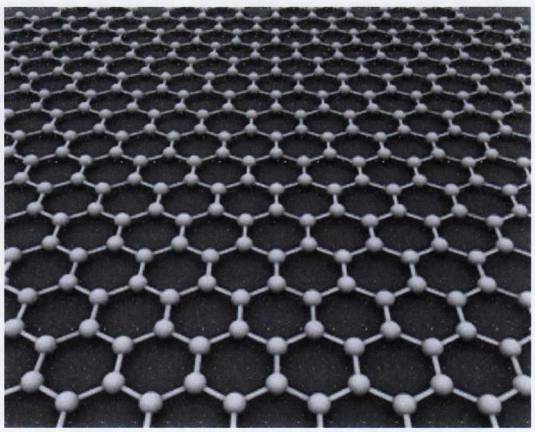

Figure 5.19: Schematic of the graphene is an atomic-scale honeycomb lattice made of carbon atoms.

mal, and mechanical and optical properties evolve from monolayer graphene to graphite will facilitate the development of graphene devices.

Typically, graphene layer/layers after being deposited on Cu or on one of the transition metals (Ti, Ni, Pd, Pt and Au) by chemical vapour deposition (CVD) [118, 119, 120, 121, 122] or UHV-CVD [121, 122, 123] will be transfered (or exfoliated) onto thin dielectric layer grown on silicon or other suitable substrates (see, for example, Ref. [118]). In some literature the intermidiate dielectric layer is called as a capping or a buffer layer and we will use the latter term in the present section. Because of their relatively low cost, grain size, good etch-ability, and their wide applicability in the semiconductor industry, Ni and Cu have received the most attention as a graphene substrate material [119, 120, 121, 122]. Single- and multi-layered graphene have successfully been grown on polycrystalline Ni [119, 120, 122], while large-area graphene has successfully been grown on Cu [121] substrates by CVD. High-yield production of graphene was also demonstrated recently in Ref. [124] by using a liquid-phase exfoliation of graphite.

For possible applications of graphene it is important to use an appropriate characterization technique which is capable to distinguish the single graphene layer from thicker flakes as well as to accurately measure the graphene thickness up to few layers of graphene (FLG). Besides, the area of single or few-layer flakes has also to be estimated. One of the possible techniques for these measurements is an optical microscopy. The visibility of graphene layer in this case depends on properties of the buffer layer, namely on its thickness and refractive index, and characterizes by the optical contrast. The number of investigations on optical contrast as well as on the best performance of the optical microscopy depending on the wavelength range used to increase the visibility of single graphene layer has been published recently [125, 126, 127, 128, 129]. Another method which proved itself as a powerful tool for distinguishing the graphene monolayers is Raman spectroscopy (see, for example, Ref. 123). Although Raman technique is incapable to measure the thickness of graphene directly, it enables to differentiate a single layer from the thicker flakes up to 10 monolayers and from graphite by the very distinguished behavior of the vibrational bands of graphene in the regions 1520–1640 cm^{-1} and 2500–2700 cm^{-1} [123, 130, 131, 132, 133, 134, 135, 136].

The differences between the aforementioned entities are well described in

terms of intensities, positions and widths of G-band (at $\sim$585 cm^{-1}), 2D-band (at $\sim$2670 cm^{-1}) and high-frequency peaks (at $\sim$1710 cm^{-1}) near the G-band of Raman spectra [123, 130, 131, 132, 133, 134, 135, 136] as well as recently discovered weak band (N-band, at $\sim$1510 cm^{-1}) [131] from the low-frequency side of G-band. In particularly, the ratio of G-band to Si–Si band (at $\sim$520 cm^{-1}), I_G/I_{Si}, is suggested for estimation of graphene layer/layers thickness, while the ratio of I_{2D}/I_G represents the intrinsic properties of a given type of graphene. The latter has been used to determine basic structural and electronic properties of graphene such as optical anisotropy, doping concentration and the number of layers. When the number of layers increases the 2D-band broadens and the I_{2D}/I_G ratio decreases from $\sim$2 for a single layer to $\sim$0.5 for double layer and to 0.3 for a triple layer of graphene.

Using Raman mapping technique (or Raman imaging) it is possible to measure the size of flakes and to determine the crystalline order of a single graphene layer in every measured point of the mapped area. The ability of Raman spectroscopy to investigate single graphene layers is based on the enhancement of Raman signal of graphene for certain thicknesses of buffer dielectric layers [109]. This phenomenon is explained by the interference of incident and Raman lights in the layered structure [109]. Thus, from the point of view of Raman intensity, the thickness of the buffer layer is also a very important parameter. In particular, for Raman mapping it is vital to be able to register the Raman spectrum with good signal to noise ratio for a shorter period of time. Otherwise the area-mapping of graphene flake of size ($100\times100\,\mu m^2$) may take up to 5–6 hours. Therefore, the use of the buffer layer with suitable characteristics is a very important issue for Raman imaging of graphene.

The aim of the present section is a simulation of the Raman intensity and optical contrast of graphene as a function of refractive index and thickness of the buffer layer at different excitation wavelengths (i.e. 457, 488, 514, 633 and 785 nm) in order to predict the best parameters of the buffer layer for simultaneous investigations using optical microscopy and micro-Raman spectroscopy to verify experimentally the obtained theoretical results.

5.3.2 Details of calculation

Each layer in the model structure from Fig 5.20 is considered as homogeneous isotropic layer with a certain refractive index, n, and a thickness, h. Monolayer of graphene is assumed to have a thickness of 0.335 nm equal to the extension of the π-orbitals out of plane [137]. The chaotically oriented emitting dipoles are located on a plane which is in the middle of the graphene layer. The propagation of the plane waves of excitation light and the plane waves emitted by oscillating dipoles is simulated by the transfer matrix method [12]. The spectral dependences of the refractive index of graphene, Si, SiO_2 and Al_2O_3 are taken from the literature [101, 138]. The refractive indexes used in calculations are shown in Table 5.3 for the most common wavelengths of Raman excitation sources. The wavenumbers of the Si–Si, G- and 2D- bands of the Raman signal were redshifted by 520, 1580 and 2670 cm^{-1} , respectively. In all calculations in this article, we assumed that the angle of incidence of the excitation light and the angle of collection of Raman signal are 60° that corresponds to the geometrical configuration of our experimental setup [1]. Note that the intensity of the signal at all frequencies is determined by the internal quantum efficiencies of the corresponding vibrational

[1] In fact, the Raman scattering is excited by the focused light beam and therefore one have to account for all angles of incidence from 0 to 60°. The same situation is with the angle of collection. In our calculations we neglected by the cone-like shape of the light; in spite of this, the theoretical data describes experimental results quite well.

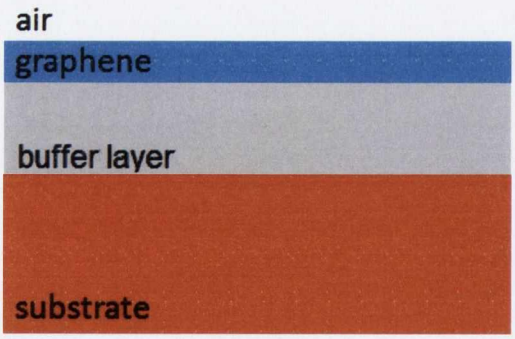

Figure 5.20: Schematic presentation of the investigated structures with graphene layer exfoliated onto SiO_2/Si substrate.

Table 5.3: Optical constants of the materials used in calculations.

Material	457 nm	488 nm	514 nm	633 nm
Si	$4.61 - 0.135i$	$4.37 - 0.084i$	$4.23 - 0.061i$	$3.88 - 0.0194i$
Al_2O_3	1.671	1.668	1.665	1.659
SiO_2	1.465	1.463	1.462	1.457
graphene	$2.69 - 1.486i$	$2.68 - 1.505i$	$2.68 - 1.536i$	$2.74 - 1.695i$

bands, optical effects such as multireflection and interference as well as by the spectral sensitivity of the experimental setup. The described calculation method is dealing only with the optical part of the Raman intensity.

In addition to calculation of intensity of Raman scattering it is important to evaluate the optical visibility of the graphene layer under white light illumination. In order to characterize the visibility of graphene layer we calculate the total color difference between the structure with graphene and substrate [126]. We start with calculation of the X, Y and Z tristimulus components by means of the CIE color-matching equations [139]:

$$\begin{cases} X = \dfrac{1}{N} \displaystyle\int_{\text{vis}} S(\lambda) R(\lambda) x(\lambda)\, \mathrm{d}\lambda \\ Y = \dfrac{1}{N} \displaystyle\int_{\text{vis}} S(\lambda) R(\lambda) y(\lambda)\, \mathrm{d}\lambda \\ Z = \dfrac{1}{N} \displaystyle\int_{\text{vis}} S(\lambda) R(\lambda) z(\lambda)\, \mathrm{d}\lambda \end{cases}, \tag{5.5}$$

Where $S(\lambda)$ is the light source spectrum, $R(\lambda)$ is the reflectance spectrum of the structure, $x(\lambda)$, $y(\lambda)$ and $z(\lambda)$ are the standard color matching functions. The color matching functions are the numerical description of the chromatic response of the human eye [139]. $1/N$ is the normalization factor and is usually chosen as

$\int_{\text{vis}} S(\lambda)y(\lambda)\,\mathrm{d}\lambda$. Then we have to move to CIE Lab space [140]:

$$\begin{cases} L = \begin{cases} 116(Y/Y_0)^{1/3} - 16 & (Y/Y_0 > 0.008856) \\ 903.3Y/Y0 & (Y/Y_0 \leq 0.008856) \end{cases} \\ a = \begin{cases} 500\left[(X/X_0)^{1/3} - (Y/Y_0)^{1/3}\right] & (X/X_0 > 0.008856) \\ 3893.5(X/X_0 - Y/Y_0) & (X/X_0 \leq 0.008856) \end{cases} \\ b = \begin{cases} 200\left[(Y/Y_0)^{1/3} - (Z/Z_0)^{1/3}\right] & (Z/Z_0 > 0.008856) \\ 1557.4(Y/Y_0 - Z/Z_0) & (Z/Z_0 \leq 0.008856) \end{cases} \end{cases}, \tag{5.6}$$

where the triple of the parameters (X_0, Y_0, Z_0) is called as a white point of the CIE standard light source. In this work we used D65 as a standard white light source. Knowledge of psychological lightness, L, and psychological chroma, a and b, enables us to calculate the total color difference:

$$\Delta E = \sqrt{(\Delta L)^2 + (\Delta a)^2 + (\Delta b)^2}, \tag{5.7}$$

which is the final image contrast between graphene and the substrate.

5.3.3 Results of modeling

In order to investigate how the excitation wavelength influences the optimal thickness of the buffer layer, we calculated the intensity of G-band of Raman signal as a function of λ_{exc} and h_{buf} in case of SiO_2 and Al_2O_3 buffer layers. The results of these calculations are shown in Fig. 5.21. The shaded vertical stripes in Fig. 5.21 denote the buffer layer thicknesses providing the total color difference higher than 2 which is enough for optical visibility of graphene.

Figure 5.21a shows that the maximal G-band intensity is achieved at UV excitation lines of 248 and 355 nm for SiO_2 layer thickness of 43 and 71 nm, respectively. For Al_2O_3 layer (see Fig. 5.21b) the maximum of G-band intensity is appeared at $h_{Al_2O_3} = 53$ nm and at $\lambda_{exc} = 350$ nm. In addition to that, as can be seen from the maps (in particular for SiO_2 buffer layer) the region correspondent to the high intensity of G-band is significantly wider for the smaller thickness values. This enables to get a reasonable enhancement of G-band for most of UV

and visible excitation lines for the thickness of SiO_2 layer of 90 nm (shown by the red crosses in Fig. 5.21a). This is in accordance with the results known from the literature [130, 132, 141]. The second and the third regions of enhanced G-band intensity from Fig. 5.21a are significantly tilted with respect to the first region as well as the above mentioned two regions are more than twice narrower. This results in much slimmer option for selection of the excitation lines for the Raman investigation of sample with one particular thickness as shown by red crosses for $h_{SiO_2} = 290$ nm, for example. In this specific case the strongest enhancement of G-band can be obtained for the excitation wavelength of 457 nm, while for

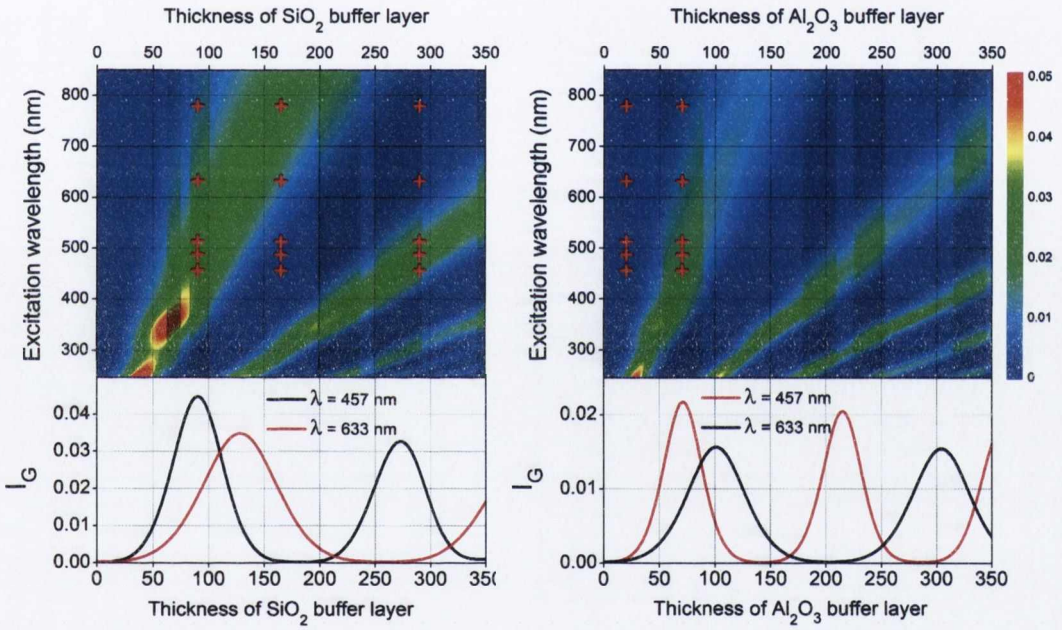

Figure 5.21: (Color online) Intensity of the G-band of Raman scattering of the samples with graphene layers as a two-dimensional function of the a) SiO_2 and b) Al_2O_3 buffer layer thicknesses and the excitation wavelength and as a plot of I_G and h_{dielec} for c) SiO_2 and b) Al_2O_3 at 457 and 633 nm excitations. The selected most common laser wavelengths corresponding to the extreme values of thicknesses of both type of buffer layers are shown by red crosses. The buffer layer thicknesses providing the highest optical contrast for each specific wavelength are denoted by black lines. The color scale on the right shows the expected Raman intensity in arbitrary units.

the red laser lines (633 and 785 nm) minimal enhancement of G-band will be observed. This again corresponds to the known literature data on weak Raman signal observed at 633 nm excitation from single graphene layer exfoliated onto 300 nm thick SiO_2 buffer layer [135, 141, 142].

In contrast, an opposite result can be expected, for example, for the thickness of the SiO_2 buffer layer of 165 nm (shown by red croses in Fig. 5.21a). In this case, the enhancement of G-band can be expected only for the 633 and 785 nm excitation lines. For Al_2O_3 similar situation is seen from the Fig. 5.21b. In order to see the enhancement factor more clearly Fig. 5.21c and 5.21d demonstrate the dependence of intensity of G-band on the buffer layer thickness for 457 nm excitation. From these figures one can conclude that for this excitation line we can expect a significant enhancement of G-band intensity for thicknesses of 90 and 290 nm and close to minimum enhancement for 165 nm thick SiO_2 buffer layer. In case of Al_2O_3 buffer layer the minimal G-band enhancement can be expected at thicknesses of ~10–20 nm and maximal enhancement at ~70 nm for 457 nm excitation wavelength. As can be seen from Fig. 5.21b for 120 nm thick Al_2O_3 buffer layer a similar situation, described above for 165 nm SiO_2 layer, can be obtained (see red crosses at 120 nm thickness in Fig. 5.21b).

Based on this analysis the thicknesses of SiO_2 and Al_2O_3 buffer layers corresponding to the extreme cases shown in Fig. 5.21 were selected for the experimental verification of the theoretical results, as described in the following section.

In addition to the above theoretical analysis, we have also calculated the dependence of the G-band Raman intensity on the number of graphene layers and the thickness of SiO_2 and Al_2O_3 buffer layer for 457 nm excitation line. The results of these calculations are presented as two-dimensional map on Figs. 5.22a and 5.22b. This map demonstrates that the highest enhancement factor due to the multiple reflection effect will be achieved for approximately 13 layers of graphene in case of SiO_2 buffer layer and 17 layers of graphene in case of Al_2O_3 buffer layer. The enhancement factor is up to 150 times in comparison to bulk graphite. As far as thickness of SiO_2 layer is concerned, the highest enhancement factor is achieved at thicknesses of 92, 293 and 494 nm. The results are in accordance for the data known from the literature for 90 and 300 nm thicknesses of SiO_2 buffer layer [130, 131, 132, 133, 135, 141, 142, 143]. We believe that the map shown in

Fig. 5.22 provide more accurate estimation of the si buffer layer thickness since in our calculations a recent data on dispersion of the graphene layer as well as other layers in the investigated layered structures were taken into account Our calculations performed for 532 nm excitation line (not shown here) coincide well with data published in Ref. [136].

5.3.4 Experimental details

Graphene was grown on the copper (Cu) foil and annealed at 1000°C for 30 minutes under hydrogen environment. Chemical vapor deposition (CVD) of graphene

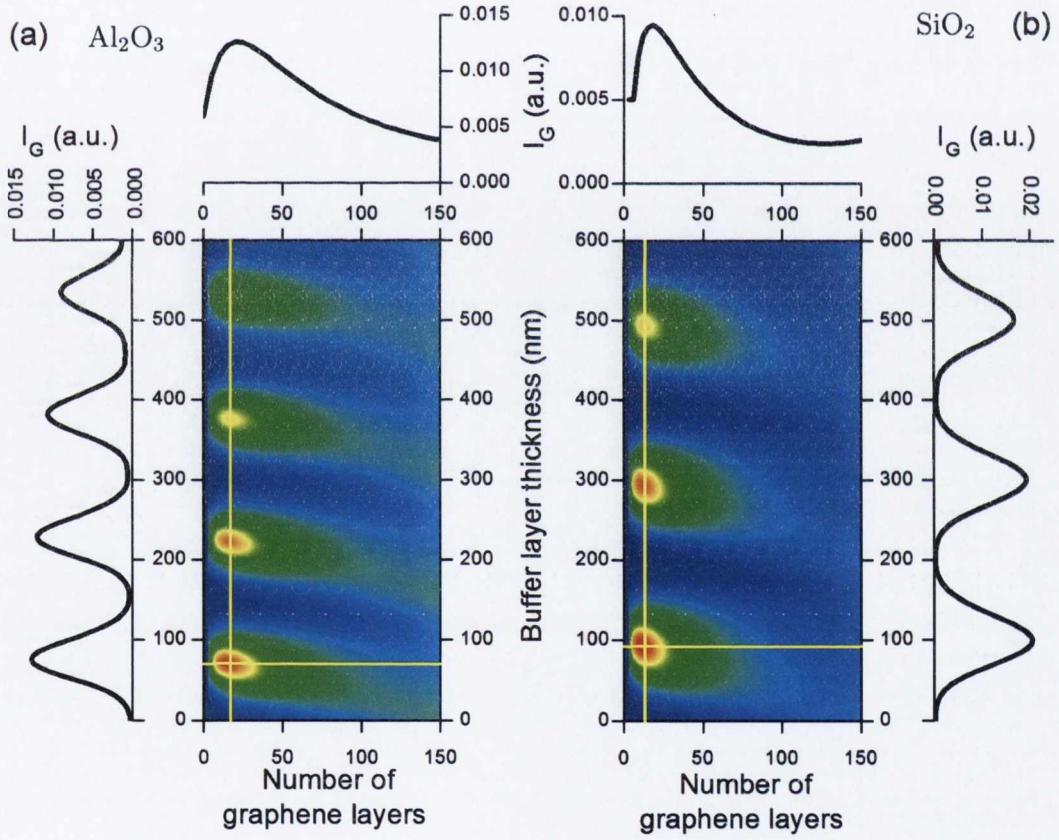

Figure 5.22: The dependence of the G-band intensity of Raman signal from the number of graphene layers and the thickness of SiO_2 and Al_2O_3 layer calculated for the excitation wavelength of 457 nm.

on Cu was carried out at a pressure of 30 Torr under the flow of methane and hydrogen. The deposition temperature was 1000°C, and the growth time was 30 min. After deposition the samples were cooled down to the room temperature in hydrogen environment (the total hydrogen pressure was 1 Torr). Then, the graphene layers were transferred onto SiO_2/Si and Al_2O_3/Si substrates using the polydimethylsiloxane (PDMS) wet etching method. Graphene was transfer onto 90, 165 and 300 nm thick thermally grown SiO_2 and 20 and 70 nm thick Al_2O_3 deposited by ALD (atomic layer deposition) technique. Figure 5.21 presents a schematic diagram of the samples experimentally investigated in this work.

Raman measurements were carried out in the backscattering geometry using Renishaw 1000 micro-Raman system. An Ar laser at 457, 488, 514 nm and HeNe laser at 633 nm with power of <10 mW were used as the excitation sources. The power was kept low to prevent the sample overheating. In addition to that, a semiconductor laser with the excitation wavelength of 785 nm with power of <10 mW nm was also used for Raman measurements of sample with 165 nm thick SiO_2 layer. The laser spot was focused on the sample surface using a 50× magnification objectives with short-focus working distance. Up to 8–10 measurements were taken from different points on each samples at each excitation wavelength. The results on the ratio of integrated intensities (namely I_G/I_{Si} and I_{2D}/I_G), discussed in the next section, were averaged from these measurements.

5.3.5 Results and discussions

The Raman spectra of the investigated sample with graphene layer are shown in Fig. 5.23. The most prominent spectral features corresponding to graphene are the G-band at 1582 cm^{-1} and the 2D-band at 2685 cm^{-1} . The G-band originates from in-plain vibrational E_{2_g} phonon mode at the Brillouin zone center and is associated with the first order Raman scattering. The 2D-band is associated with the second order Raman scattering. Using the shape and the spectral position of the 2D-band one could distinguish a single graphene layer from the bulk graphite. For the single graphene layer the 2D-band is a single sharp Lorentzian peak with a peak position below 2700 cm^{-1} and a line-width of ~30–40 cm^{-1} in contrast to the two- or multi-component peak appeared in case of the FLG and bulk graphite

[123]. In our case the 2D-band consists of single peak with a line-width of 30–37 cm^{-1} that corresponds to the single graphene layer. Raman spectra, shown in Fig. 5.23, are normalized to the intensity of the 2D-band for convenience of the presentation. Nevertheless, it can be clearly seen from the spectra presented that at this excitation line the intensity of Raman spectra in the region of G- and 2D-bands for 20 nm of Al_2O_3 layer is much smaller than intensity for the 70 nm of this type of buffer layer (see much lower signal-to-noise ratio). Similar conclusion can be drawn from the comparison of Raman spectra for graphene layer exfoliated onto 90, 165 and 300 nm SiO_2 buffer layer. For the SiO_2 layer of 165 nm thick the Raman spectrum again demonstrate much lower signal-to noise ratio, which means that the intensity of the original spectrum is lower than that for 90 and 300 nm thick SiO_2 layer. These results are in accordance with the maps shown in Figs. 5.21a and 5.21b. For comparison with the theoretical results described in Section 1.3, we plotted the Raman spectra of graphene on SiO_2 layer of different thicknesses for all three investigated samples registered at different excitation wavelengths, namely 457 nm (Fig. 5.24a) and 633 nm (Fig. 5.24b). As can be seen from Figs. 5.24a and 5.24b, the peak position G-band practically remains unchanged while the peak position of 2D-band is shifted by nearly 40 cm^{-1}

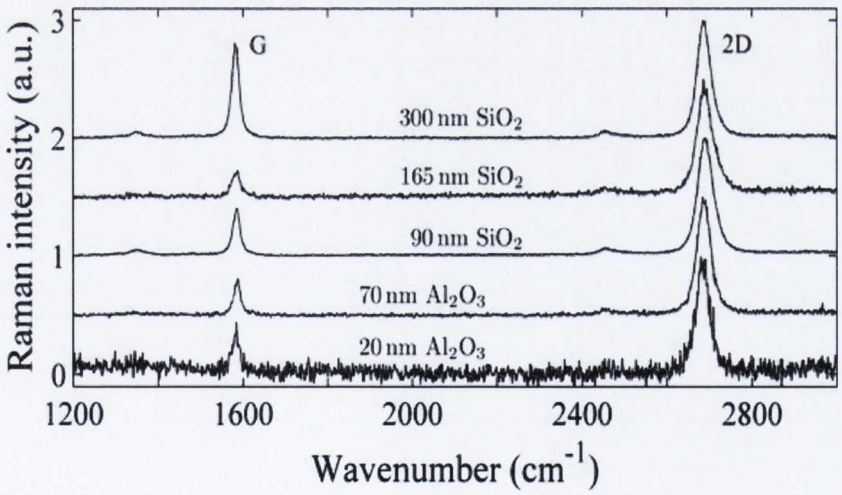

Figure 5.23: Raman spectra of graphene layers separated from the Si substrate by different buffer layers. Excitation wavelength is 514 nm.

from $\nu_{max} \sim 2690\,\mathrm{cm}^{-1}$ (for 457 nm excitation) to $\nu_{max} \sim 2652\,\mathrm{cm}^{-1}$ (for 633 nm excitation) due to the probing of different points in momentum space for the electronic and phonon dispersion at different excitation energy (or wavelength) [123]. Figure 5.24a shows that for 457 nm excitation line the graphene spectrum for 165 nm thick SiO_2 layer is of the smallest intensity, while the intensity of both bands (G- and 2D-) for 90 and 300 nm thick buffer layer is nearly 15 times higher. At the same time the Raman intensity of graphene for 300 nm thick buffer layer is slightly lower than that for 90 nm thick buffer. This exactly corresponds to the results followed from the map of Fig. 5.22a. Figure 5.22b shows Raman spectra of the same samples at 633 nm excitation line. One can see that the spectrum of graphene for 300 nm thick buffer layer has now the lowest intensity, while the intensity of G-band is much higher for graphene on 165 nm thick buffer and only

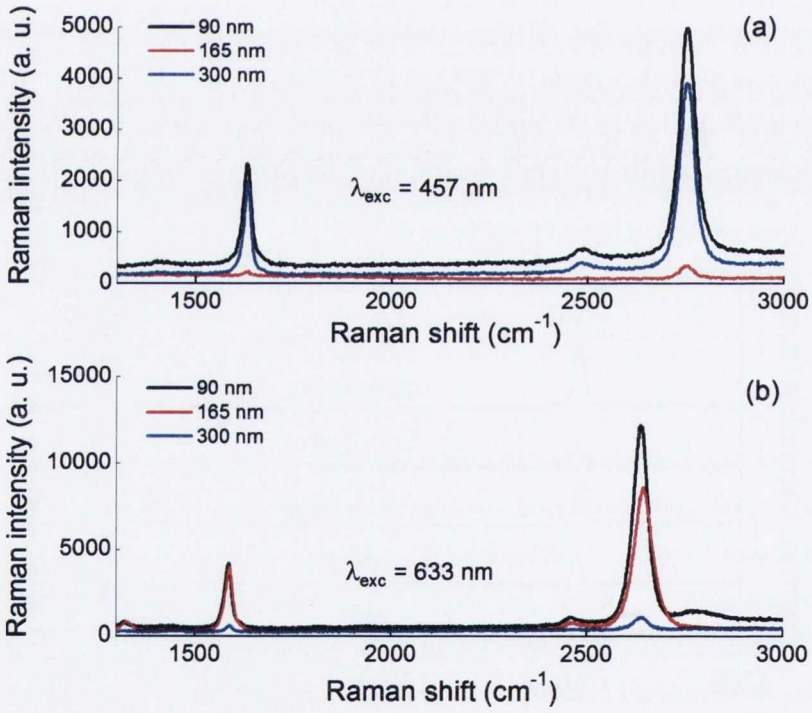

Figure 5.24: Raman spectra of graphene exfoliated onto SiO_2 buffer layer of various thicknesses (90 nm — black line, 165 nm — red line and 300 nm — blue line) for different excitation wavelengths: (a) 457 nm and (b) 633 nm.

slightly lower for 90 nm thick SiO_2 layer. Again this result exactly corresponds to the case demonstrated in Fig. 5.21a for these three samples at 633 nm excitation. As can be clearly seen from Figs. 5.23 and 5.24, the ratio of the G- and 2D-bands intensities depends on the thickness and the material of the buffer layer. The results of calculations of the ratio of intensities of the G- and 2D-bands of Raman spectra, I_{2D}/I_G, for all investigated samples with graphene layer transferred onto SiO_2 and Al_2O_3 buffer layers are presented in Fig. 5.25. The experimentally obtained ratios are shown by symbols on the same graph. The experimental and theoretical results are in good agreement demonstrating that the ratio of G- and 2D- bands intensities may vary by a factor of ~4. Similar results were demonstrated in Ref. [143] for the excitation wavelength of 514 nm. Intensities of G-band, which are obtained experimentally and calculated by the method oscillating dipoles, cannot be compared between each other directly because the observed Raman intensity depends on the experimental conditions. In order to compare quantitatively the theoretical and experimental results, let us calculate now the ratio of the intensity of the G-band to the intensity of the Si band (at 520 cm^{-1}), I_G/I_{Si}. Results of these calculation are shown for different excitation wavelengths in Figs. 5.25 and Fig. 5.26. As it was mentioned in Section 5.3.2, we have not made any assumptions on the internal quantum efficiencies of the

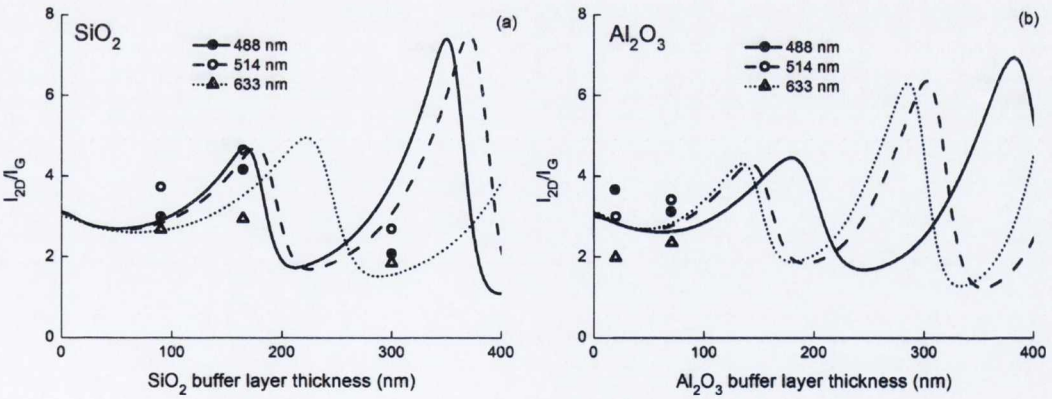

Figure 5.25: Calculated (lines) and experimental (symbols) ratios of the intensities of Raman 2D-band and G-band as a function of SiO_2 and Al_2O_3 buffer layer thicknesses for different excitation wavelengths.

Raman scattering at the frequencies of the G- or Si–Si bands. Therefore, the dependencies I_G/I_{Si}, presented in Figs. 5.24 and 5.25, concern only the optical part of the Raman signal. In order to demonstrate how the optical effects influence the ratio I_G/I_{Si} we normalized the experimental dependencies I_G/I_{Si} to the corresponding theoretical ones. It can be seen from Figs. 5.25 and 5.26 that the ratio is a periodical function of the buffer layer thickness. The period of this function depends on the excitation wavelength and can be found from the condition of two nearest Fabry-Perot resonances which appeared during the propagation of the excitation light through the buffer layer: $\Delta h_{buf} = \frac{\lambda}{2n\cos f}$, where λ is the excitation wavelength, n is the refractive index of the buffer layer and f is the angle of light propagation in the buffer layer. The maximal Raman intensities of the samples are up to 50 times higher than the minimal ones. The experimentally obtained data are in agreement with the theoretical curves. Intensities of

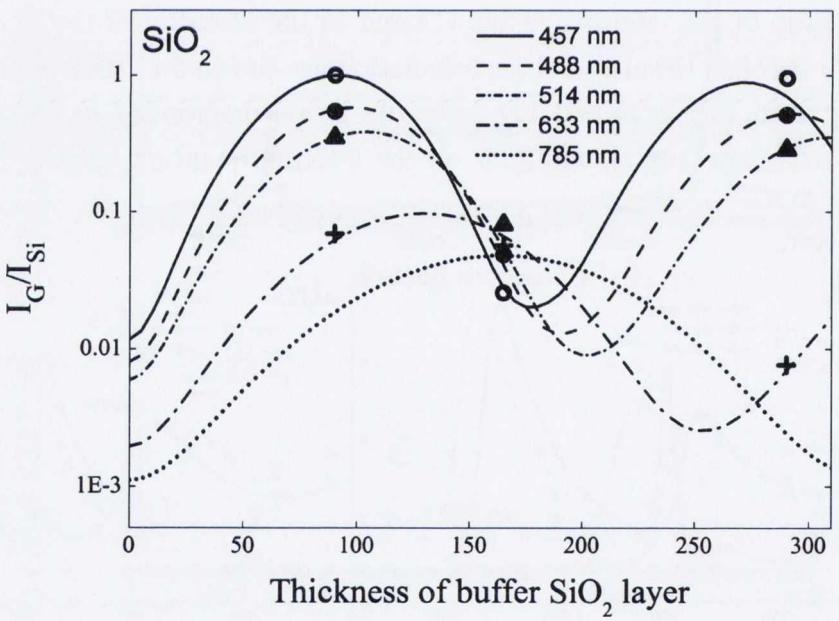

Figure 5.26: Calculated (lines) and experimental (symbols) values of the ratio I_G/ISi as a function of SiO_2 buffer layer thickness for different excitation wavelengths. The experimental data are normalized to the corresponding theoretical data.

the Raman scattering of graphene in case of SiO_2 buffer layer are approximately 1.5 times higher than that in case of Al_2O_3 layer. From Figs. 5.25 and 5.26 it also follows that the intensity of the G-band of Raman scattering in case of 457 nm excitation wavelength is approximately one order of magnitude higher than in case of 633 nm excitation wavelength. Therefore, the account only for the optical effects in the investigated samples with graphene leads to the conclusion that the use of 457 nm excitation line is more preferable than, for example, a 633 nm excitation. We would like to emphasize that this conclusion was drawn without any assumption about the internal efficiencies of different bands of Raman scattering. To comment on the better correspondence of the theoretical and experimental results shown in Figs. 5.26 and 5.27 from one side and in Figs. 5.25a and 5.25b from another side we can refer to some literature findings. In accordance with Ref. [144], for example, the intensity of the 2D-band depends more strongly on carrier density and less strongly on the number of layers [132, 144] than the in-

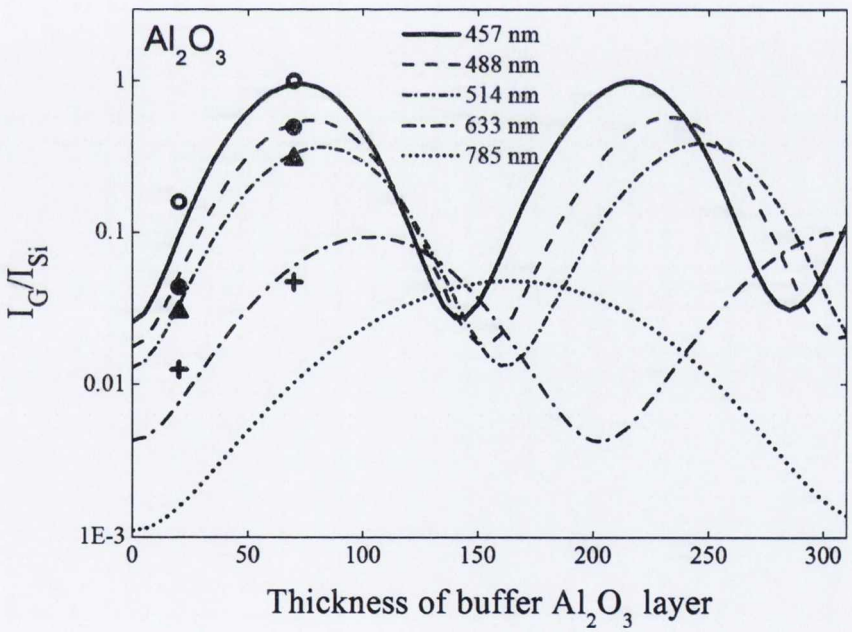

Figure 5.27: Calculated (lines) and experimental (symbols) values of the ratio I_G/ISi as a function of Al_2O_3 buffer layer thickness for different excitation wavelengths. The experimental data are normalized to the corresponding theoretical data.

tensity of G-band. Since the carrier density in each individual graphene flake is affected by impurities in and on the graphene flake, the I_{2D}/I_{Si} (as well as I_{2D}/I_G) ratios are not so reliable metric for the number of graphene layers. We believe that in our case the influence of defects in graphene layers affect more strongly the intensity of 2D-band and this results in more stronger deviation of experimental points from the experimental ones in Figs. 5.25a and 5.25b. Therefore, in this case the influence of effects other than purely optical can play a significant role and need to be included to the theoretical model for better correspondence of simulations with the experimental results.

For investigation of influence of the refractive index and the thickness of the buffer layer on the resulted Raman intensity of G-band we calculated the Raman intensity as a two-dimensional function of thickness and refractive index of the buffer layer. Figure 5.28 shows the results of this calculation for the excitation wavelength of 457 nm as a region where the intensity of G-band exceeds 25% of

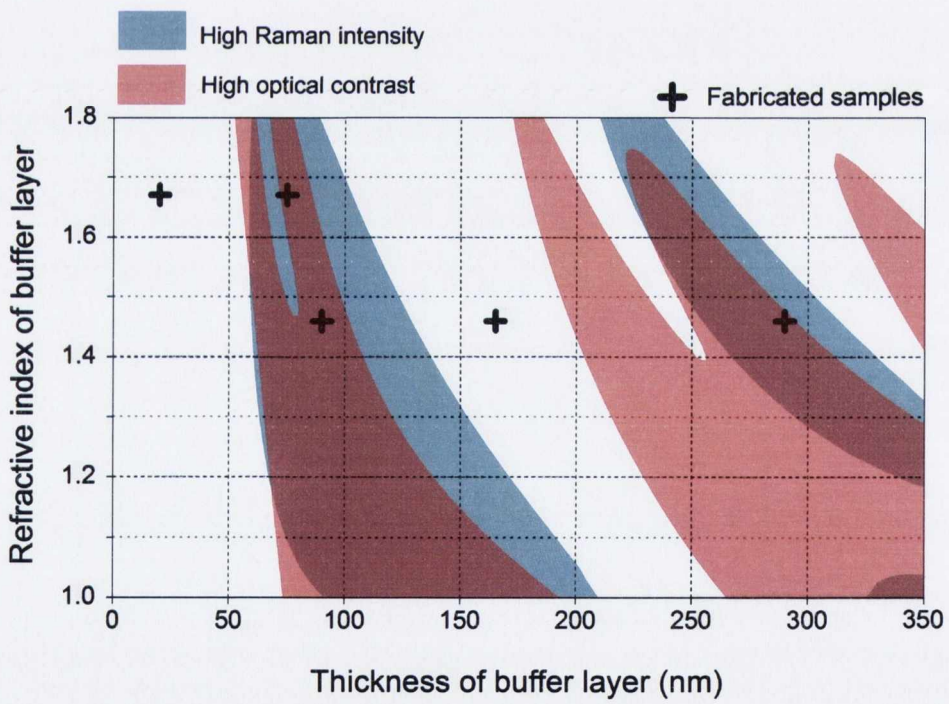

Figure 5.28: (Color online) Regions of the high Raman intensity ($> 0.25 I_{max}$) and high total color difference ($\Delta E > 2$)

the highest Raman intensity. In contrast to Figs. 5.26 and 5.27, the intensities of the G-band of Raman scattering, which are shown in Fig. 5.28, are not divided by the intensity of the Si band. Similar maps can be obtained for other excitation wavelengths. In addition to the high Raman intenisity, Fig. 5.28 shows the regions where the total color difference exceeds 2 that is enough for optical visibility of graphene. As can be seen from Fig. 5.28, the regions of the high Raman intensity and the high optical contrast does not coincide. The intersections of these regions correspond to the best substrate from the point of view of experimental investigation of graphene.

For the sake of completeness, the theoretical simulations of optical contrast of graphene are verified experimentally for investigated samples. Indeed, Fig. 5.29 demonstrates that the graphene areas are clearly seen for the buffer layers of 90 nm and 300 nm of SiO_2 and 70 nm of Al_2O_3 whereas the samples with 165 nm of SiO_2 and 20 nm of Al_2O_3 are characterized by low optical contrast.

In conclusion, we have suggested a simultaneous presentation of Raman intensity and optical contrast maps for single layer of graphene depending on the refractive index and thickness of the buffer layer. This presentation enables a selection of the buffer layer material in order to obtain the Raman and optical microscopy imaging at their best performance. The advantages of this presentation, demonstrated for 457 nm excitation wavelength, is confirmed experimentally for two dielectric materials, SiO_2 and Al_2O_3 , with different refractive indexes and thicknesses. It has been also shown that for the thickness of SiO_2 buffer layer in the range of 150–160 nm quite substantial enhancement of the G-band intensity from single graphene layer can be achieved even at longer excitation wavelengths, namely at 633 and 785 nm.

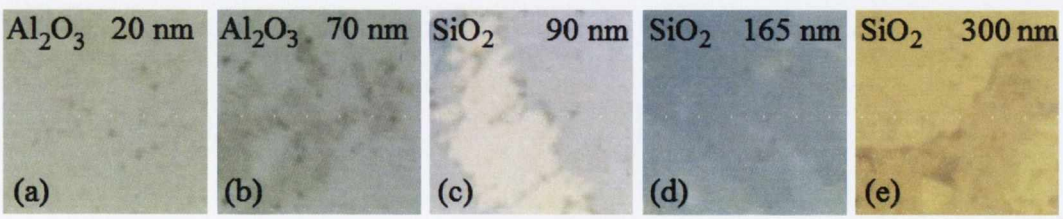

Figure 5.29: (Color online) Optical images of the samples with graphene layers (a), (b) in case of SiO_2 substrate and (c)–(e) Al_2O_3 substrate.

Chapter 6

Conclusions

In this work the optical properties of periodical one- and two-dimensional structures as well as the layered structures based on silicon were investigated theoretically and experimentally. The theoretical methods include the scattering matrix method, transfer matrix method and the method of oscillating dipoles. The infrared spectroscopy, Raman spectroscopy, photoluminescence spectroscopy and ellipsometry were used in this work as experimental characterization technique. The following results were obtained:

1. The reflection spectra of one-dimensional grooved silicon structures were investigated theoretically and experimentally in the spectral range $\lambda = 4-20\,\mu$m at normal angle of light incidence. The grooved silicon structures consists of alternating walls and grooves with the period of $a = 4-6\,\mu$m. It was shown that the inevitable light losses which are caused by the imperfections of geometry such as aperiodicity, deviation of the wall thickness from the average value as well as the roughness of surfaces, can be taken into account by an introduction of a small imaginary part to the refractive index of silicon in the periodical area. The theoretical reflection spectra were calculated by using the scattering matrix method and are in good agreement with the experimental results. Furthermore, the values of the effective refractive indexes of the grooved silicon structures are well described by above mentioned approach in the spectral region where the wavelength and the wall thickness are of the same order of magnitude.

2. The reflection and transmission spectra of two-dimensional photonic crystal with triangular lattice of air pores in silicon were investigated experimentally and theoretically. The calculation by the scattering matrix method accounts for the attributes of the real photonic crystal samples such as the limited number of periods, the presence of the interface between incoming medium and the periodical area as well as the geometrical imperfections. It was found that the presence of interface may cause the appearance of the dips in the spectral region of the photonic stop-bands of the reflection spectrum. These dips are associated with the photonic surface modes. We showed that for the surface mode, the electric field takes the shape of vortices located between the upper pores while the maxima of the magnetic field are in the center of these vortices. The modeling of the roughness of inner surfaces of pores enabled to properly describe the amplitude and the spectral position of the surface associate dips. The theoretical reflection and transmission spectra are in very good agreement with the experimental data. The described analysis of the surface modes was performed for the first time.

3. The quantitative analysis of the excitation of photoluminescence and its out-coupling from the layered structures with silicon nanocrystals was performed by using the method of oscillating dipoles. The propagation of light through the sample was modeled by the transfer matrix method which take into account all aspects of the optical system such as the angle of excitation light incidence, solid angle of collection of photoluminescent light, wavelengths and polarizations of excitation and photoluminescent light, thicknesses and refractive indexes of all the layers. We determined the thicknesses of buffer, active and capping layers which provide the optimal spatial distribution of the refractive index both for in-coupling of the excitation light and for out-coupling of the photoluminescent light. It was shown that the structure with optimized thicknesses of layers exhibit up to 50 times higher photoluminescence intensity than that with non-optimized thicknesses. The theoretical predictions are verified by the photoluminescence measurements of the sample with silicon nanocrystals fabricated by

the PECVD method.

4. The processes of the Raman scattering and its subsequent emergence from the porous-Si-based multilayered samples was investigated quantitatively. It was found that the Raman intensity of the investigated samples strongly depends on the spectral position of the excitation light with respect to the photonic stop-band and can be enhanced by a factor of 10. The effect of the enhancement of Raman scattering is explained either by resonant penetration of the excitation light into the sample or by resonant out-coupling of the scattered light from the sample or both. The experimentally observed enhancement relates to the case of resonant penetration of the excitation light.

5. The Raman scattering from single layer of graphene was investigated theoretically and experimentally. It was demonstrated that the intensity of Raman signal as well as the optical contrast of the single graphene layer depends on the thickness and the refractive of the buffer layer which separates graphene from the substrate. The thickness which provide the maximal Raman intensity and the high optical contrast in case of SiO_2 buffer layers is 90 nm and in case of Al_2O_3 buffer layer is 80 nm. The theoretical and experimental results show the good agreement between each other.

The **novelty** of the results can be expressed in the following statements:

1. Optical anisotropy of the grooved silicon structures was investigated theoretically and experimentally in the spectral region where the wavelength is comparable with the period of these structures.

2. For the first time, the analysis of influence of the photonic surface mode on the light propagation through two-dimensional photonic crystal with triangular lattice of air holes in silicon was performed.

3. It was demonstrated that the photoluminescence intensity of the multilayered samples with silicon nanocrystals can be increased up to 50 times by appropriate choice of the thicknesses of capping, active and buffer layer.

Future work:

1. There is still a lot to be learned about the surface modes, for instance, why some of the surface dips have much lower quality factor than other surface dips. For this we have to calculate the distribution of the electromagnetic field for the higher order modes and to calculate the dispersion relation of these modes.

2. The local dielectric environment of silicon nanocrystals influences not only the intensity of the out-coupled emission but also on the spontaneous emission rate of silicon nanocrystals [17, 97]. Therefore varying the thicknesses of capping, inter and buffer layers we can manipulate with the lifetime of the photoluminescence. It is interesting to calculate the ratio of the emission rates of silicon nanocrystal in the layered system and in vacuum, which is called the Purcell factor. It is also interesting to compare the theoretical data with time resolved measurements of photoluminescence.

3. In Section 5.3 we assumed that graphene is separated from substrate by a single buffer layer. At the same time in Ref. [128] it was shown that if the graphene layer is separated from substrate by the stack of two layers with different properties then the optical contrast can be enhanced. Therefore it would be quite interesting to investigate if this also affect the intensity of Raman scattering.

References

[1] K. Sakoda, *Optical Properties of Photonic Crystals.* Springer, 2001.

[2] K. Ohtaka, "Energy band of photons and low-energy photon diffraction," *Phys. Rev. B*, vol. 19, no. 10, pp. 5057–5067, 1979.

[3] N. Stefanou, V. Karathanos, and A. Modinos, "Scattering of electromagnetic waves by periodic structures," *Journal of Physics: Condensed Matter*, vol. 4, p. 7389, 1992.

[4] R. M. A. Azzam and N. M. Bashara, *Ellipsometry and polarized light*, vol. 31. North Holland, 1987.

[5] S. Brand and D. Hughes, "Calculations of bound states in the valence band of AlAs/GaAs/AlAs and AlGaAs/GaAs/AlGaAs quantum wells," *Semicond. Sci. and Techn.*, vol. 2, p. 607, 1987.

[6] C. Mailhoit and D. L. Smith, "$k - p$ theory of semiconductor superlattice electronic structure," *Phys. Rev. B*, vol. 33, no. 12, pp. 8360–8372, 1986.

[7] J. B. Pendry and A. MacKinnon, "Calculation of photon dispersion relations," *Phys. Rev. Lett.*, vol. 69, no. 19, pp. 2772–2775, 1992.

[8] D. M. Whittaker and I. S. Culshaw, "Scattering-matrix treatment of patterned multilayer photonic structures," *Phys. Rev. B*, vol. 60, no. 24, pp. 2610–2618, 1999.

[9] S. G. Tikhodeev, A. L. Yablonskii, E. A. Muljarov, N. A. Gippius, and T. Ishihara, "Quasiguided modes and optical properties of photonic crystals," *Phys. Rev. B*, 2002.

[10] A. Taflove, *Computational Electrodinamics: The Finite-Difference Time-Domain Method.* Boston: Artech House, 1995.

[11] M. Born, E. Wolf, and A. B. Bhatia, *Principles of optics: electromagnetic theory of propagation, interference and diffraction of light.* Cambridge Univ Pr, 1999.

[12] P. Markoš and C. M. Soukoulis, *Wave propagation: from electrons to photonic crystals and left-handed materials.* Princeton Univ Pr, 2008.

[13] D. Y. K. Ko and J. C. Inkson, "Matrix method for tunneling in heterostructures: Resonant tunneling in multilayer system," *Phys. Rev. B*, vol. 38, pp. 9945–9951, 1988.

[14] F. Abeles, "La détermination de l'indice et de l'épaisseur des couches minces transparentes," *J. Phys. Radium*, vol. 11, 1950.

[15] H. Benisty, R. Stanley, and M. Mayer, "Method of source terms for dipole emission modification in modes of planar structures," *J. Opt. Soc. Am. A*, no. 5, 1998.

[16] R. Meerheim, M. Furno, S. Hofmann, B. Lüssem, and K. Leo, "Quantification of energy loss mechanisms in organic light-emitting diodes," *Appl. Phys. Lett.*, vol. 97, p. 253305, 2010.

[17] R. J. Walters, J. Kalkman, A. Polman, H. A. Atwater, and M. J. A. De Dood, "Photoluminescence quantum efficiency of dense silicon nanocrystal ensembles in Sio_2," *Phys. Rev. B*, vol. 73, no. 13, p. 132302, 2006.

[18] K. A. Neyts, "Simulation of light emission from thin-film microcavities," *J. Opt. Soc. Am. A*, vol. 15, no. 4, pp. 962–971, 1998.

[19] C. E. Reed, J. Giergiel, J. C. Hemminger, and S. Ushioda, "Dipole radiation in a multilayer geometry," *Phys. Rev. B*, vol. 36, no. 9, p. 4990, 1987.

[20] S. Hayashi, T. Kitagawa, Y. Sekiguchi, and T. Kume, "Enhanced-raman scattering from organic thin films mediated by half-leaky guided modes," *Surf. Sci.*, vol. 427, pp. 126–130, 1999.

[21] K. Imakita, M. Fujii, T. Nakamura, S. Miura, E. Takeda, and S. Hayashi, "Enhancement of radiative recombination rate of excitons in si nanocrystals on au film," *Jpn. J. Appl. Phys.*, vol. 45, no. 8, pp. 6132–6136, 2006.

[22] E. Takeda, T. Nakamura, M. Fujii, S. Miura, and S. Hayashi, "Surface plasmon polariton mediated photoluminescence from excitons in silicon nanocrystals," *Appl. Phys. Lett.*, vol. 89, p. 101907, 2006.

[23] R. M. A. Azzam and N. M. Bashara, "Polarization characteristics of scattered radiation from a diffraction grating by ellipsometry with application to surface roughness," *Phys. Rev. B*, vol. 5, no. 12, p. 4721, 1972.

[24] T. M. Geppert, *Towards Photonic Crystal-Based Spectroscopic Gas Sensors.* PhD thesis, Universitaat Paderborn, Dept. Physik, 2005.

[25] D. Pergande, A. von Rhein, T. Geppert, and R. Wehrspohn, "Coupling schemes for low-group velocity photonic crystal devices," *J. Comput. Theor. Nanos.*, vol. 6, no. 9, pp. 1993–2000, 2009.

[26] D. Pergande, T. M. Geppert, A. von Rhein, S. L. Schweizer, R. B. Wehrspohn, and S. Moretton, "Miniature infrared gas sensors based on photonic crystals," *J. Appl. Phys.*, 2011.

[27] J. D. Joannopoulos, S. G. Johnson, R. D. Winn, and R. D. Meade., *Photonic Crystals. Molding the Flow of Light.* Princeton University Press, 2 ed., 2008.

[28] N. Malkova and C. Z. Ning, "Shockley and Tamm surface states in photonic crystals," *Phys. Rev. B*, vol. 73, no. 11, p. 113113, 2006.

[29] A. P. Vinogradov, A. V. Dorofeenko, S. G. Erokhin, M. Inoue, A. A. Lisyansky, A. M. Merzlikin, and A. B. Granovsky, "Surface state peculiarities in one-dimensional photonic crystal interfaces," *Phys. Rev. B*, vol. 74, no. 4, p. 045128, 2006.

[30] N. Malkova and C. Z. Ning, "Tamm surface states in a finite chain of defects in a photonic crystal," *J. Phys.: Condens. Matter*, vol. 19, p. 056004, 2007.

[31] E. Moreno, F. García-Vidal, and L. Martin-Moreno, "Enhanced transmission and beaming of light via photonic crystal surface modes," *Phys. Rev. B*, vol. 69, no. 12, p. 121402, 2004.

[32] A. Namdar, I. V. Shadrivov, and Y. S. Kivshar, "Backward Tamm states in left-handed metamaterials," *Appl. Phys. Lett.*, vol. 89, p. 114104, 2006.

[33] Y. S. Kivshar, "Nonlinear Tamm states and surface effects in periodic photonic structures," *Laser Phys. Lett.*, vol. 5, no. 10, pp. 703–713, 2008.

[34] A. P. Vinogradov, A. V. Dorofeenko, A. M. Merzlikin, and A. A. Lisyansky, "Surface states in photonic crystals," *Physics-Uspekhi*, vol. 53, p. 243, 2010.

[35] P. Yeh, A. Yariv, and A. Cho, "Optical surface waves in periodic layered media," *Appl. Phys. Lett.*, vol. 32, p. 104, 1978.

[36] F. Lederer, L. Leine, R. Muschall, T. Peschel, C. Schmidt-Hattenberger, T. Trutschel, A. Boardman, and C. Wachter, "Strongly nonlinear effects with weak nonlinearities in smart waveguides," *Opt. Commun.*, vol. 99, no. 1-2, pp. 95–100, 1993.

[37] N. Malkova, I. Hromada, X. Wang, G. Bryant, and Z. Chen, "Observation of optical Shockley-like surface states in photonic superlattices," *Opt. Lett.*, vol. 34, no. 11, pp. 1633–1635, 2009.

[38] T. Decoopman, G. Tayeb, S. Enoch, D. Maystre, and B. Gralak, "Photonic crystal lens: From negative refraction and negative index to negative permittivity and permeability," *Phys. Rev. Lett.*, vol. 97, p. 073905, Aug 2006.

[39] S. Xiao, M. Qiu, Z. Ruan, and S. He, "Influence of the surface termination to the point imaging by a photonic crystal slab with negative refraction," *Appl. Phys. Lett.*, vol. 85, p. 4269, 2004.

[40] A. Mihi, H. Míguez, I. Rodríguez, and S. Rubio, "Surface resonant modes in photonic crystals," *Phys. Rev. B*, no. 12, 2005.

[41] B. S. Song, S. Noda, T. Asano, and Y. Akahane, "Ultra-high-Q photonic double-heterostructure nanocavity," *Nature materials*, vol. 4, no. 3, pp. 207–210, 2005.

[42] E. Istrate and E. H. Sargent, "Photonic crystal heterostructures and interfaces," *Rev. Mod. Phys.*, vol. 78, pp. 455–481, 2006.

[43] Y. Takahashi, H. Hagino, Y. Tanaka, B. Song, T. Asano, and S. Noda, "High-q nanocavity with a 2-ns photon lifetime," *Optics Express*, vol. 15, no. 25, pp. 17206–17213, 2007.

[44] S. Tomljenovic-Hanic, C. M. de Sterke, and M. J. Steel, "Design of high-q cavities in photonic crystal slab heterostructures by air-holes infiltration," *Optics Express*, vol. 14, no. 25, pp. 12451–12456, 2006.

[45] S. Fan, S. G. Johnson, J. D. Joannopoulos, C. Manolatou, and H. A. Haus, "Waveguide branches in photonic crystals," *J. Opt. Soc. Am. B*, vol. 18, no. 2, pp. 162–165, 2001.

[46] A. Mekis, J. C. Chen, I. Kurland, S. Fan, P. R. Villeneuve, and J. D. Joannopoulos, "High transmission through sharp bends in photonic crystal waveguides," *Phys. Rev. Lett.*, vol. 77, pp. 3787–3790, Oct 1996.

[47] S. G. Johnson, C. Manolatou, S. Fan, P. R. Villeneuve, J. D. Joannopoulos, and H. A. Haus, "Elimination of cross talk in waveguide intersections," *Optics Letters*, vol. 23, no. 23, pp. 1855–1857, 1998.

[48] S. Fan, P. R. Villeneuve, J. D. Joannopoulos, and H. A. Haus, "Channel drop tunneling through localized states," *Phys. Rev. Lett.*, vol. 80, pp. 960–963, Feb 1998.

[49] M. Soljačić, M. Ibanescu, S. G. Johnson, Y. Fink, and J. D. Joannopoulos, "Optimal bistable switching in nonlinear photonic crystals," *Phys. Rev. E*, vol. 66, p. 055601, Nov 2002.

[50] M. Notomi, A. Shinya, S. Mitsugi, G. Kira, E. Kuramochi, and T. Tanabe, "Optical bistable switching action of Si high-Q photonic-crystal nanocavities," *Optics Express*, vol. 13, no. 7, pp. 2678–2687, 2005.

[51] E. V. Astrova, G. V. Fedulova, Y. A. Zharova, and E. V. Gushchina, "Sidewall roughness of deep trenches in 1D and 2D periodic silicon structures fabricated by photoelectrochemical etching," *Phys. Stat. Sol. (C)*, vol. 8, no. 6, pp. 1936–1940, 2011.

[52] A. A. Maradudin and D. L. Mills, "Scattering and absorption of electromagnetic radiation by a semi-infinite medium in the presence of surface roughness," *Phys. Rev. B*, vol. 11, no. 4, pp. 1392–1415, 1975.

[53] H. Benisty, D. Labilloy, C. Weisbuch, C. J. M. Smith, T. F. Krauss, D. Cassagne, A. Beraud, and C. Jouanin, "Radiation losses of waveguide-based photonic crystals: Positive role of the substrate," *Appl. Phys. Lett.*, 2000.

[54] H. Benisty, P. H. Lalanne, S. Olivier, M. Rattier, C. Weisbuch, C. J. M. Smith, T. F. Krauss, C. Jouanin, and D. Cassagne, "Finite-depth and intrinsic losses in vertically etched two-dimensional photonic crystals," *Opt. Quant. Electron.*, vol. 34, no. 1, pp. 205–215, 2002.

[55] S. A. Dyakov, E. V. Astrova, T. S. Perova, S. G. Tikhodeev, N. A. Gippius, and V. Y. Timoshenko, "Optical properties of grooved silicon microstructures: theory and experiment," *JETP*, vol. 113, no. 1, pp. 80–85, 2011.

[56] S. A. Dyakov, E. V. Astrova, T. S. Perova, V. A. Tolmachev, G. V. Fedulova, A. Baldycheva, V. Y. Timoshenko, S. G. Tikhodeev, and N. A. Gippius, "Optical spectra of two-dimensional photonic crystal bars based on macroporous Si," in *Proceedings of SPIE*, vol. 7943, p. 79431I, 2011.

[57] A. Christ, T. Zentgraf, J. Kuhl, S. G. Tikhodeev, N. A. Gippius, and H. Giessen, "Optical properties of planar metallic photonic crystal structures: experiment and theory," *Phys. Rev. B*, vol. 70, p. 125113, Sep 2004.

[58] I. E. Tamm *Phys. Z. Sowietunion*, vol. 1, p. 733, 1932.

[59] S.-T. Wu *Opt. Eng.*, vol. 26, no. 2, p. 1208, 1987.

[60] J. Schilling, A. Birner, F. Müller, R. B. Wehrspohn, R. Hillebrand, U. Gösele, K. Busch, S. Johnc, S. W. Leonardc, and H. M. van Drielc,

"Optical characterisation of 2d macroporous silicon photonic crystals with bandgaps around 3.5 and 1.3 μm," *Opt. Mat.*, vol. 17, no. 1, pp. 7–10, 2001.

[61] T. Geppert, S. L. Schweizer, U. Gösele, and R. B. Wehrspohn, "Deep trench etching in macroporous silicon," *Appl. Phys. A*, vol. 84, no. 3, pp. 237–242, 2006.

[62] R. B. Wehrspohn, S. L. Schweizer, and V. Sandoghdar, "Linear and nonlinear optical experiments based on macroporous silicon photonic crystals," *Phys. Stat. Sol. A*, vol. 204, no. 11, pp. 3708–3726, 2007.

[63] E. V. Astrova, G. V. Fedulova, and E. V. Guschina, "Formation of 2d photonic crystal bars by simultaneous photoelectrochemical etching of trenches and macropores in silicon," *Semiconductors*, vol. 44, no. 12, pp. 1617–1623, 2010.

[64] V. Lehmann, *Electrochemistry of Silicon.* D-69469 Weinheim: Wiley-VCH, 2002.

[65] V. Lehmann and H. Föll, "Formation mechanism and properties of electrochemically etched trenches in n-type silicon," *J. Electrochem. Soc.*, vol. 137, no. 2, pp. 653–659, 1990.

[66] S. A. Dyakov, V. A. Tolmachev, E. V. Astrova, S. G. Tikhodeev, V. Y. Timoshenko, and T. S. Perova, "Numerical methods for calculation of optical properties of layered structures," in *Proceedings of SPIE*, vol. 7521, p. 75210G, 2009.

[67] E. V. Astrova, T. S. Perova, V. A. Tolmachev, R. A. D., J. K. Vij, and A. Moore, "IR birefringence in crystal fabricated by anisotropic etching of silicon," *Semiconductors*, no. 4, 2003.

[68] E. Y. Krutkova, V. Y. Timoshenko, L. A. Golovan, P. K. Kashkarov, E. V. Astrova, T. S. Perova, B. P. Gorshunov, and A. A. Volkov, "Infrared and submillimeter spectroscopy of grooved silicon structures," *Semiconductors*, vol. 40, no. 7, pp. 834–838, 2006.

[69] V. A. Tolmachev, T. S. Perova, E. V. Astrova, B. Z. Volchek, and J. K. Vij, "Vertically etched silicon as 1D photonic crystal," *Phys. Stat. Sol. (A)*, vol. 197, no. 2, 2003.

[70] V. A. Tolmachev, E. V. Astrova, Y. A. Pilyugina, T. S. Perova, R. Moore, and J. K. Vij, "1D photonic crystal fabricated by wet etching of silicon," *Opt. Mat.*, vol. 28, no. 5, pp. 831–835, 2005.

[71] D. A. Mamichev, V. Y. Timoshenko, A. V. Zoteyev, L. A. Golovan, E. Y. Krutkova, A. V. Laktyunkin, P. K. Kashkarov, E. V. Astrova, and T. S. Perova, "Enhanced raman scattering in grooved silicon matrix," *Phys. Status Solidi B*, vol. 246, no. 1, pp. 173–176, 2009.

[72] V. A. Tolmachev, T. S. Perova, E. V. Astrova, J. Pilyugina, A. Moore, and K. Berwick, "Optical characteristics of ordinary and tunable 1D Si photonic crystals in the mid-infrared range," vol. 5825 of *Proc. SPIE*, 2005.

[73] E. V. Astrova, V. A. Tolmachev, G. V. Fedulova, V. A. Melnikov, A. V. Ankudinov, and T. S. Perova, "Optical properties of one-dimensional photonic crystals fabricated by photo-electrochemical etching of silicon," *Appl. Phys. A*, vol. 98, no. 3, pp. 571–581, 2010.

[74] A. V. Zoteev, L. A. Golovan, E. Y. Krutkova, A. V. Laktyunkin, D. A. Mamichev, P. K. Kashkarov, V. Y. Timoshenko, E. V. Astrova, and T. S. Perova, "Enhancement of the raman scattering in grooved silicon structures," *Semiconductors*, vol. 41, no. 8, pp. 970–972, 2007.

[75] M. Elwenspoek and H. V. Jansen, *Silicon micromachining.* United Kingdom: Cambridge University Press, 2004.

[76] D. L. Kendall, "Vertical etching of silicon at very high aspect ratios," *Ann. Rev. Mater. Sci*, vol. 9, pp. 373–403, 1979.

[77] G. Barillaro, A. Nannini, and F. Pieri, "Dimensional constraints on high aspect ratio silicon microstructures fabricated by hf photoelectrochemical etching," *J. Electrochem. Soc.*, vol. 149, no. 3, pp. C180–C185, 2002.

[78] E. V. Astrova and G. V. Fedulova, "Formation of deep periodic trenches in photo-electrochemical etching of n-type silicon," *J. Micromech. Microeng.*, vol. 19, 2009. 095009.

[79] M. Hoffmann and E. Voges, "Bulk silicon micromachining for mems in optical communication systems," *J. Micromech. Microeng.*, no. 12, pp. 349–360, 2002.

[80] E. V. Astrova, V. A. Tolmachev, Y. A. Zharova, G. V. Fedulova, A. V. Baldycheva, and T. S. Perova, "Silicon periodic structures and their liquid crystal composites," *Solid State Phenomena*, vol. 156, pp. 547–554, 2010.

[81] A. Chu, S. H. Zaidi, and S. R. J. Brueck, "Fabrication and raman scattering studies of one-dimensional nanometer structures in (100) silicon," *Appl. Phys. Lett.*, vol. 63, no. 7, pp. 905–907, 1993.

[82] A. Holke and H. T. Henderson, "Ultra-deep anisotropic etching of (110) silicon," *J. Micromech. Microeng.*, vol. 9, no. 1, pp. 51–57, 1999.

[83] S. Godefroo, M. Hayne, M. Jivanescu, A. Stesmans, M. Zacharias, O. I. Lebedev, G. Van Tendeloo, and V. V. Moshchalkov, "Classification and control of the origin of photoluminescence from si nanocrystals," *Nat. Nanotechnol.*, vol. 3, no. 3, pp. 174–178, 2008.

[84] L. Pavesi, L. Dal Negro, C. Mazzoleni, G. Franzo, and F. Priolo, "Optical gain in silicon nanocrystals," *Nature*, vol. 408, no. 6811, pp. 440–444, 2000.

[85] R. J. Walters, G. I. Bourianoff, and H. A. Atwater, "Field-effect electroluminescence in silicon nanocrystals," *Nature Mater.*, vol. 4, no. 2, pp. 143–146, 2005.

[86] F. Iacona, G. Franzò, and C. Spinella, "Correlation between luminescence and structural properties of si nanocrystals," *J. Appl. Phys.*, vol. 87, p. 1295, 2000.

[87] F. Iacona, C. Bongiorno, C. Spinella, S. Boninelli, and F. Priolo, "Formation and evolution of luminescent si nanoclusters produced by thermal annealing of sio_x films," *J. Appl. Phys.*, vol. 95, p. 3723, 2004.

[88] D. Comedi, O. H. Y. Zalloum, E. A. Irving, J. Wojcik, T. Roschuk, M. J. Flynn, and P. Mascher, "X-ray-diffraction study of crystalline si nanocluster formation in annealed silicon-rich silicon oxides," *J. Appl. Phys.*, vol. 99, p. 023518, 2006.

[89] M. Falconieri, E. Borsella, L. De Dominicis, F. Enrichi, G. Franzò, F. Priolo, F. Iacona, F. Gourbilleau, and R. Rizk, "Probe of the Si nanoclusters to er energy transfer dynamics by double-pulse excitation," *Appl. Phys. Lett.*, vol. 87, p. 061109, 2005.

[90] X. D. Pi, O. H. Y. Zalloum, T. Roschuk, J. Wojcik, A. P. Knights, P. Mascher, and P. J. Simpson, "Light emission from si nanoclusters formed at low temperatures," *Appl. Phys. Lett.*, vol. 88, p. 103111, 2006.

[91] L. Penninck, S. Mladenowski, and K. Neyts, "The effects of planar metallic interfaces on the radiation of nearby electrical dipoles," *J. of Optics*, vol. 12, p. 075001, 2010.

[92] S. Mladenovski, S. Reineke, and K. Neyts, "Measurement and simulation of exciton decay times in organic light-emitting devices with different layer structures," *Opt. Lett.*, vol. 34, no. 9, pp. 1375–1377, 2009.

[93] A. W. Lu and A. D. Rakić, "Design of microcavity organic light emitting diodes with optimized electrical and optical performance," *Appl. Opt.*, vol. 48, no. 12, pp. 2282–2289, 2009.

[94] S. Mladenovski, K. Neyts, D. Pavicic, A. Werner, and C. Rothe, "Exceptionally efficient organic light emitting devices using high refractive index substrates," *Opt. Express*, vol. 17, no. 9, pp. 7562–7570, 2009.

[95] F. Iacona, G. Franzò, E. C. Moreira, and F. Priolo, "Silicon nanocrystals and er ions in an optical microcavity," *J. Appl. Phys.*, vol. 89, p. 8354, 2001.

[96] A. Hryciw, Y. Jun, and M. L. Brongersma, "Plasmon-enhanced emission from optically-doped mos light sources," *Opt. Exp.*, vol. 17, no. 1, pp. 185–192, 2009.

[97] E. M. Purcell, "Spontaneous emission probabilities at radio frequencies," *Physical Review*, vol. 69, p. 681, 1946.

[98] T. Nakamura, M. Fujii, S. Miura, M. Inui, and S. Hayashi, "Enhancement and suppression of energy transfer from si nanocrystals to er ions through a control of the photonic mode density," *Phys. Rev. B*, vol. 74, no. 4, p. 045302, 2006.

[99] S. Miura, T. Nakamura, M. Fujii, M. Inui, and S. Hayashi, "Size dependence of photoluminescence quantum efficiency of si nanocrystals," *Phys. Rev. B*, vol. 73, no. 24, p. 245333, 2006.

[100] S. Takeoka, M. Fujii, and S. Hayashi, "Size-dependent photoluminescence from surface-oxidized si nanocrystals in a weak confinement regime," *Phys. Rev. B*, vol. 62, pp. 16820–16825, Dec 2000.

[101] E. D. Palik and G. Ghosh, *Handbook of optical constants of solids*, vol. 3. Academic press, 1998.

[102] Y. C. Fang, W. Q. Li, L. J. Qi, L. Y. Li, Y. Y. Zhao, Z. J. Zhang, and M. Lu, "Photoluminescence from SiO_x thin films: effects of film thickness and annealing temperature," *Nanotechnology*, vol. 15, p. 494, 2004.

[103] Y. Qu, L. Liao, Y. Li, H. Zhang, Y. Huang, and X. Duan, "Electrically conductive and optically active porous silicon nanowires," *Nano Lett.*, vol. 9, no. 12, pp. 4539–4543, 2009.

[104] H. C. Yuan, V. E. Yost, M. R. Page, P. Stradins, D. L. Meier, and H. M. Branz, "Efficient black silicon solar cell with a density-graded nanoporous surface: Optical properties, performance limitations, and design rules," *Appl. Phys. Lett.*, vol. 95, p. 123501, 2009.

[105] O. Bisi, S. Ossicini, and L. Pavesi, "Porous silicon: a quantum sponge structure for silicon based optoelectronics," *Surface Science Reports*, vol. 38, no. 1-3, pp. 1–126, 2000.

[106] S. A. Dyakov, D. M. Zhigunov, A. Hartel, M. Zacharias, T. S. Perova, and V. Y. Timoshenko, "Enhancement of photoluminescence signal from ultrathin layers with silicon nanocrystals," *Appl. Phys. Lett.*, vol. 100, no. 6, p. 061908, 2012.

[107] D. Blue, K. Helwig, M. Moskovits, and R. Wolkow, "Interference effects in surface enhanced raman scattering by thin adsorbed layers," *J. Chem. Phys.*, vol. 92, p. 4600, 1990.

[108] M. Futamata, E. Keim, A. Bruckbauer, D. Schumacher, and A. Otto, "Enhanced raman scattering from copper phthalocyanine on pt by use of a weierstrass prism," *Appl. Surf. Sci.*, vol. 100, pp. 60–63, 1996.

[109] Y. Y. Wang, Z. H. Ni, Z. X. Shen, H. M. Wang, and Y. H. Wu, "Interference enhancement of raman signal of graphene," *Appl. Phys. Lett.*, vol. 92, p. 043121, 2008.

[110] S. Gupta, G. Morell, R. Katiyar, J. Abelson, H. C. Jin, and I. Balberg, "Interference enhanced raman scattering of hydrogenated amorphous silicon revisited," *J. Raman Spectr.*, vol. 32, no. 1, pp. 23–25, 2001.

[111] R. J. Nemanich, C. C. Tsai, and G. A. N. Connell, "Interference-enhanced raman scattering of very thin titanium and titanium oxide films," *Phys. Rev. Lett.*, vol. 44, no. 4, pp. 273–276, 1980.

[112] D. A. Mamichev, K. A. Gonchar, V. Y. Timoshenko, G. K. Mussabek, and V. E. Nikulin, "Enhanced raman scattering in structures of porous silicon," *J. Raman. Spectrosc.*, 2011.

[113] K. A. Gonchar, G. K. Musabek, T. I. Taurbayev, and V. Y. Timoshenko, "Enhancement of photoluminescence and raman scattering in one-dimensional photonic crystals based on porous silicon," *Semiconductors*, vol. 45, no. 5, pp. 614–617, 2011.

[114] A. K. Geim and K. S. Novoselov, "The rise of graphene," *Nature Mat.*, vol. 6, no. 3, pp. 183–191, 2007.

[115] P. Gava, M. Lazzeri, A. M. Saitta, and F. Mauri, "Ab initio study of gap opening and screening effects in gated bilayer graphene," *Physical Review B*, vol. 79, no. 16, p. 165431, 2009.

[116] X. Li, Y. Zhu, W. Cai, M. Borysiak, B. Han, D. Chen, R. D. Piner, L. Colombo, and R. S. Ruoff, "Transfer of large-area graphene films for high-performance transparent conductive electrodes," *Nano letters*, vol. 9, no. 12, pp. 4359–4363, 2009.

[117] I. Khrapach, F. Withers, T. H. Bointon, D. K. Polyushkin, W. L. Barnes, S. Russo, and M. F. Craciun, "Novel highly conductive and transparent graphene-based conductors," *Advanced Mat.*, vol. 24, no. 21, pp. 2844–2849, 2012.

[118] C. Mattevi, H. Kim, and M. Chhowalla, "A review of chemical vapour deposition of graphene on copper," *J. Mater. Chem.*, vol. 21, no. 10, pp. 3324–3334, 2010.

[119] Q. Yu, J. Lian, S. Siriponglert, H. Li, Y. Chen, and S. S. Pei, "Graphene segregated on ni surfaces and transferred to insulators," *Appl. Phys. Lett.*, vol. 93, no. 11, pp. 113103–113103, 2008.

[120] K. S. Kim, Y. Zhao, H. Jang, S. Y. Lee, J. M. Kim, K. S. Kim, J. H. Ahn, P. Kim, J. Y. Choi, and B. H. Hong, "Large-scale pattern growth of graphene films for stretchable transparent electrodes," *Nature*, vol. 457, no. 7230, pp. 706–710, 2009.

[121] X. Li, W. Cai, J. An, S. Kim, J. Nah, D. Yang, R. Piner, A. Velamakanni, I. Jung, E. Tutuc, *et al.*, "Large-area synthesis of high-quality and uniform graphene films on copper foils," *Science*, vol. 324, no. 5932, pp. 1312–1314, 2009.

[122] W. Liu, C. H. Chung, C. Q. Miao, Y. J. Wang, B. Y. Li, L. Y. Ruan, K. Patel, Y. J. Park, J. Woo, and Y. H. Xie, "Chemical vapor deposition of large area few layer graphene on si catalyzed with nickel films," *Thin solid films*, vol. 518, no. 6, pp. S128–S132, 2010.

[123] L. M. Malard, M. A. Pimenta, G. Dresselhaus, and M. S. Dresselhaus, "Raman spectroscopy in graphene," *Physics Reports*, vol. 473, no. 5-6, pp. 51–87, 2009.

[124] Y. Hernandez, V. Nicolosi, M. Lotya, F. M. Blighe, Z. Sun, S. De, I. T. McGovern, B. Holland, M. Byrne, Y. K. Gunko, J. J. Boland, P. Niraj, G. Duesberg, S. Krishnamurthy, R. Goodhue, J. Hutchison, V. Scardaci, A. C. Ferrari, and C. J. N., "High-yield production of graphene by liquid-phase exfoliation of graphite," *Nature Nanotechnology*, vol. 3, no. 9, pp. 563–568, 2008.

[125] P. Blake, E. Hill, A. H. C. Neto, K. S. Novoselov, D. Jiang, R. Yang, T. J. Booth, and A. K. Geim, "Making graphene visible," *Appl. Phys. Lett.*, vol. 91, p. 063124, 2007.

[126] L. Gao, W. Ren, F. Li, and H. M. Cheng, "Total color difference for rapid and accurate identification of graphene," *ACS Nano*, vol. 2, no. 8, pp. 1625–1633, 2008.

[127] O. Albrektsen, R. L. Eriksen, S. M. Novikov, D. Schall, M. Karl, S. I. Bozhevolnyi, and A. C. Simonsen, "High resolution imaging of few-layer graphene," *J. Appl. Phys.*, vol. 111, no. 6, pp. 064305–064305, 2012.

[128] C. Kontis, M. R. Mueller, C. Kuechenmeister, K. T. Kallis, and J. Knoch, "Optimizing the identification of mono-and bilayer graphene on multilayer substrates," *Appl. Opt.*, vol. 51, no. 3, pp. 385–389, 2012.

[129] K. Peters, N. Gayer, A. Graf, V. Paulava, U. Wurstbauer, W. Hansen, *et al.*, "Enhancing the visibility of graphene on GaAs," *Appl. Phys. Lett.*, vol. 99, no. 19, p. 191912, 2011.

[130] A. Gupta, G. Chen, P. Joshi, S. Tadigadapa, and P. C. Eklund, "Raman scattering from high-frequency phonons in supported n-graphene layer films," *Nano Letters*, vol. 6, no. 12, pp. 2667–2673, 2006.

[131] F. Herziger, P. May, and J. Maultzsch, "Layer-number determination in graphene by out-of-plane phonons," *Phys. Rev. B*, vol. 85, no. 23, p. 235447, 2012.

[132] Y. K. Koh, M. H. Bae, D. G. Cahill, and E. Pop, "Reliably counting atomic planes of few-layer graphene ($n > 4$)," *ACS Nano*, vol. 5, no. 1, pp. 269–274, 2011.

[133] D. Graf, F. Molitor, K. Ensslin, C. Stampfer, A. Jungen, C. Hierold, and L. Wirtz, "Spatially resolved raman spectroscopy of single-and few-layer graphene," *Nano Letters*, vol. 7, no. 2, pp. 238–242, 2007.

[134] P. H. Tan, W. P. Han, W. J. Zhao, Z. H. Wu, K. Chang, H. Wang, Y. F. Wang, N. Bonini, N. Marzari, and N. Pugno, "The shear mode of multilayer graphene," *Nature Materials*, vol. 11, no. 4, pp. 294–300, 2012.

[135] A. C. Ferrari, J. C. Meyer, V. Scardaci, C. Casiraghi, M. Lazzeri, F. Mauri, S. Piscanec, D. Jiang, K. S. Novoselov, and S. Roth, "Raman spectrum of graphene and graphene layers," *Phys. Rev. Lett.*, vol. 97, no. 18, p. 187401, 2006.

[136] D. Yoon, H. Moon, Y. W. Son, J. S. Choi, B. H. Park, Y. H. Cha, Y. Kim, and H. Cheong, "Interference effect on raman spectrum of graphene on SiO_2/Si," *Phys. Rev. B*, vol. 80, no. 12, p. 125422, 2009.

[137] L. Pauling, *The Nature of the Chemical Bond.* Ithaca: Cornell University Press, 1960.

[138] J. W. Weber, V. E. Calado, and M. C. M. Van de Sanden, "Optical constants of graphene measured by spectroscopic ellipsometry," *Appl. Phys. Lett.*, vol. 97, p. 091904, 2010.

[139] S. Janos, *Colorimetry: understanding the CIE system.* John Wiley & Sons: New Jersey, 2007.

[140] "International Color Consortium Specification icc.1:2001-04," 2001.

[141] J. Wasyluk, T. S. Perova, C. Miao, and Y. H. Xie, "Raman mapping analysis of graphene on Ni, Cu and SiO_2/Si substrates," in *the XIX International Materials Research Congress (IMRC)*, 2010.

[142] C. H. Lui, Z. Li, Z. Chen, P. V. Klimov, L. Brus, and T. F. Heinz, "Imaging stacking order in few-layer graphene," *Nano Letters*, vol. 11, no. 1, pp. 164–169, 2011.

[143] Z. H. Ni, H. M. Wang, J. Kasim, H. M. Fan, T. Yu, Y. H. Wu, Y. P. Feng, and Z. X. Shen, "Graphene thickness determination using reflection and contrast spectroscopy," *Nano Letters*, vol. 7, no. 9, pp. 2758–2763, 2007.

[144] A. Das, S. Pisana, B. Chakraborty, S. Piscanec, S. K. Saha, U. V. Waghmare, K. S. Novoselov, H. R. Krishnamurthy, A. K. Geim, and A. C. Ferrari, "Monitoring dopants by raman scattering in an electrochemically top-gated graphene transistor," *Nature Nanotechnology*, vol. 3, no. 4, pp. 210–215, 2008.

[145] A. Yariv and P. Yeh, *Optical Waves in Crystals*. New York: Wiley, 1984.

[146] P. Yeh, "Electromagnetic propagation in birefringent layered media," *J. Opt. Soc. Am.*, vol. 69, no. 5, pp. 742–756, 1979.

[147] J. Cos, J. Ferre-Borrull, J. Pallares, and L. F. Marsal, "Tunable fabry-pérot filter based on one-dimensional photonic crystals with liquid crystal components," *Opt. Comm.*, vol. 282, pp. 1220–1225, 2009.

Appendix A

Example of application of transfer matrix method for microcavity structure

This paragraph demonstrates the example of application of the transfer matrix method for calculation of optical properties of a one-dimensional photonic crystal with the defect. The structure consists of alternating layers of the materials with the refractive indexes $n_1 = 3.42$ and $n_2 = 1.2$. The geometrical thicknesses of the layers are equal to $d_1 = d_2 = 120\,\text{nm}$. The layered structure has a defect layer with the refractive index n_2 and the thickness of 300 nm. The angle of incidence is $\varphi = 45°$. The schematic of the described structure is shown in Fig A.1. The reflection spectra of the model structure in the spectral range 300–400 nm are shown in Fig. A.2 for s- and p-polarizations. The wide regions of high reflection in spectrum for s-polarization are associated with the photonic band gaps. The resonance dip at s-polarization has the spectral position at $\lambda \approx 312\,\text{nm}$, while for p-polarization at $\lambda \approx 320\,\text{nm}$. As can be seen from Fig A.2, the reflection coefficients at $\lambda \approx 312\,\text{nm}$ are equal to 0 for both polarizations. The materials are assumed to be non-absorbing, therefore the transmission coefficient at this wavelength is 1. The full transmission in s-polarization is due to the light coupling to the defect mode. Thus, the electromagnetic field is localized mainly in the defect layer. In order to demonstrate this fact we calculated the electric field distribution of the incident light at $\lambda = 312\,\text{nm}$ in the model structure (Fig. A.1).

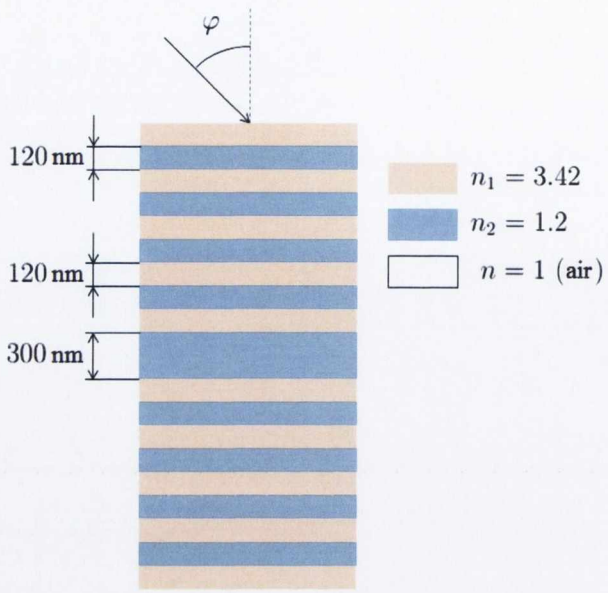

Fig. A.1: Schematic of the microcavity structure.

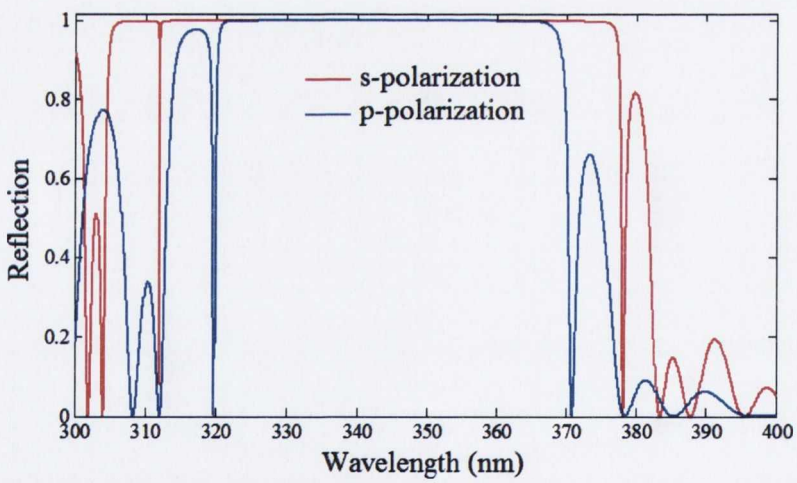

Fig. A.2: Reflection spectra of the microcavity structure for s- and p-polarizations of incidenct light.

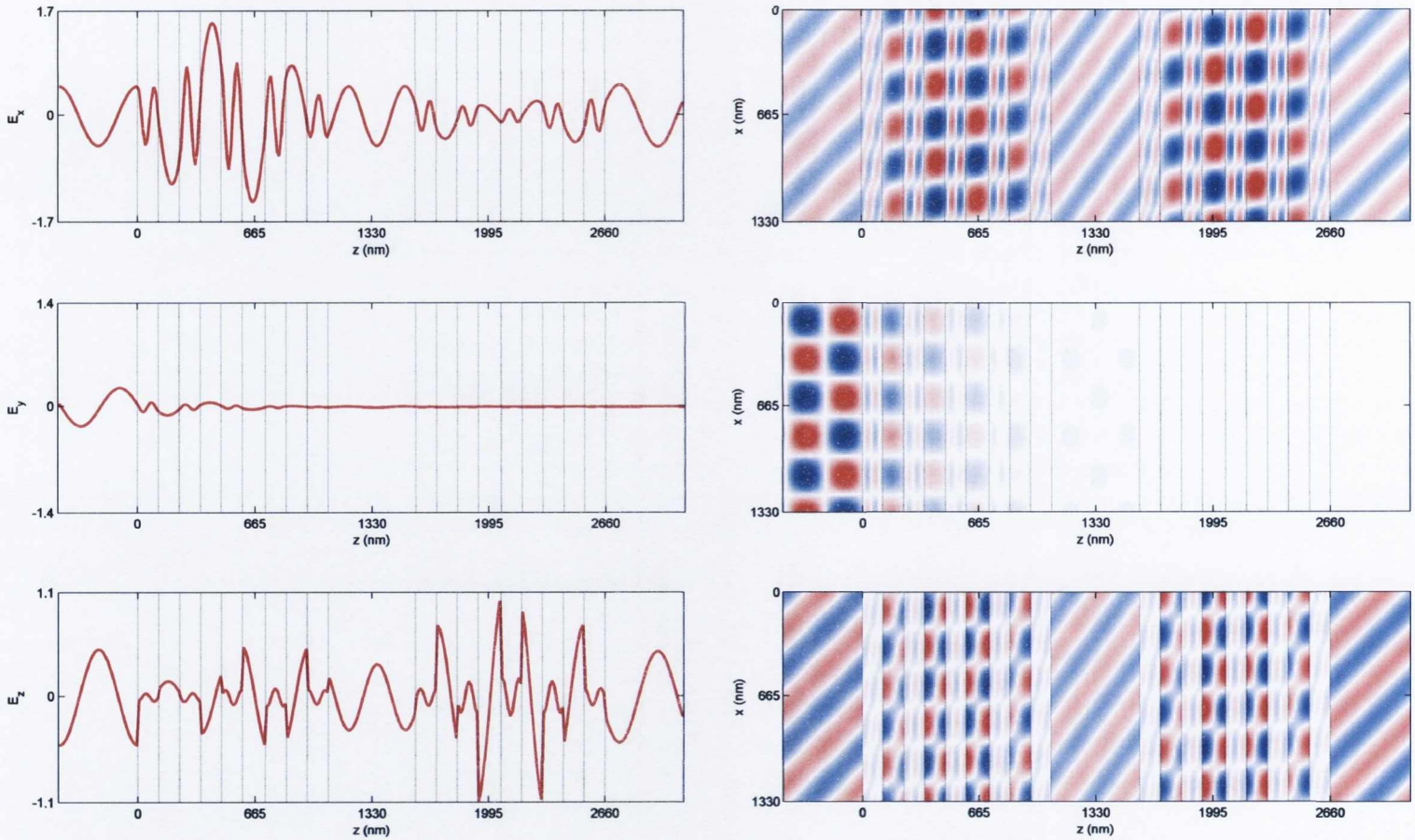

Fig. A.3: Spatial field distributions of the incident light in the microcavity structure. (a), (b), (c): Distributions of the x-, y- and z-components of the electric field along z-direction. (d), (e), (f) Distributions of the x-, y- and z-components of the electric field along x- and z-directions. The red (blue) color indicates positive (negative) values of the electric field strength. The redder (bluer) means the higher amplitude. $\lambda = 312\,\mathrm{nm}$

As can be seen from Fig. A.3, for p-polarization (x- and z-components), the incident light passes through the structure without losses and the average spatial light localization is the same within the structure. For s-polarization the intensity of transmitted light is equal to the intensity of the incident light, however the amplitude of oscillations of y-component of electric field is maximal in the defect layer.

Note that according to the boundary conditions for the electric field , the tangential components of the electric field vector, E_x and E_y, are continuous, whereas the vertical component, E_z, has the discontinuity of the first kind at the interfaces between the layers.

Appendix B

Transfer matrix method for anisotropic media

As was mentioned in the Section 2.1, the 2×2 transfer matrix method is mainly applicable for the simulation of the layered structure with isotropic components. In order to operate with anisotropic structures another approach must be used.

Let us consider a layered structure as in the case of 2×2 transfer matrix method (see Fig.2.1). In case of anisotropic layers we describe materials by means of the dielectric constants tensor

$$\hat{\varepsilon} = A \cdot \begin{pmatrix} \varepsilon_1 & 0 & 0 \\ 0 & \varepsilon_2 & 0 \\ 0 & 0 & \varepsilon_3 \end{pmatrix} \cdot A^{-1} = \begin{pmatrix} \varepsilon_{11} & \varepsilon_{12} & \varepsilon_{13} \\ \varepsilon_{21} & \varepsilon_{22} & \varepsilon_{23} \\ \varepsilon_{31} & \varepsilon_{32} & \varepsilon_{33} \end{pmatrix}, \tag{B.1}$$

where ε_{ik} are the principal dielectric constants and A is the coordinate rotation matrix. Each layer is characterized by its propagation 4×4 matrix P and each interface by its dynamical matrix D. We define z-axis to be perpendicular to the layers. The matrixes D can be determined by the following expression [145, 146, 147]:

$$D(n) = \begin{pmatrix} e_x \cdot \mathbf{p}_1^{(n)} & e_x \cdot \mathbf{p}_2^{(n)} & e_x \cdot \mathbf{p}_3^{(n)} & e_x \cdot \mathbf{p}_4^{(n)} \\ e_y \cdot \mathbf{q}_1^{(n)} & e_y \cdot \mathbf{q}_2^{(n)} & e_y \cdot \mathbf{q}_3^{(n)} & e_y \cdot \mathbf{q}_4^{(n)} \\ e_y \cdot \mathbf{p}_1^{(n)} & e_y \cdot \mathbf{p}_2^{(n)} & e_y \cdot \mathbf{p}_3^{(n)} & e_y \cdot \mathbf{p}_4^{(n)} \\ e_x \cdot \mathbf{q}_1^{(n)} & e_x \cdot \mathbf{q}_2^{(n)} & e_x \cdot \mathbf{q}_3^{(n)} & e_x \cdot \mathbf{q}_4^{(n)} \end{pmatrix}, \tag{B.2}$$

In case of isotropic layer, the matrix (B.3) would equal to a zero matrix. In order to solve this problem we must define the dynamical matrix in such a way that it is block diagonalized when the mode coupling disappears. In this case we obtain the following D matrix:

$$D(n) = \begin{pmatrix} 1 & 1 & 0 & 0 \\ \dfrac{\gamma_1}{\mu_0\omega} & \dfrac{\gamma_2}{\mu_0\omega} & 0 & 0 \\ 0 & 0 & \dfrac{\gamma_3}{\mu_0\omega} & \dfrac{\gamma_4}{\mu_0\omega} \\ 0 & 0 & 1 & 1 \end{pmatrix}, \tag{B.3}$$

The propagation matrix is defined then by

$$P(n) = \begin{pmatrix} e^{-j\gamma_1^{(n)}d_n} & 0 & 0 & 0 \\ 0 & e^{-j\gamma_2^{(n)}d_n} & 0 & 0 \\ 0 & 0 & e^{-j\gamma_3^{(n)}d_n} & 0 \\ 0 & 0 & 0 & e^{-j\gamma_4^{(n)}d_n} \end{pmatrix}, \tag{B.4}$$

where n is the number of layer, e_x and e_y are the unit vectors in the x- and y-directions, and $p_k^{(n)}$ and $q_k^{(n)}$ are the polarization vectors of the layer n defined as:

$$\mathbf{p}_k^{(n)} = N_k \begin{pmatrix} \left(\frac{\omega}{c}\right)^2 \varepsilon_{zz}\left[\left(\frac{\omega}{c}\right)^2 \varepsilon_{yy} - \gamma_k^2\right] - \left(\frac{\omega}{c}\right)^4 \varepsilon_{yz}^2 \\ \left(\frac{\omega}{c}\right)^4 \varepsilon_{yz}\varepsilon_{xz} - \left(\frac{\omega}{c}\right)^4 \varepsilon_{xy}\varepsilon_{zz} \\ \left(\frac{\omega}{c}\right)^4 \varepsilon_{xy}\varepsilon_{yz} - \left(\frac{\omega}{c}\right)^2 \varepsilon_{xz}\left[\left(\frac{\omega}{c}\right)^2 \varepsilon_{yy} - \gamma_k^2\right] \end{pmatrix}, \tag{B.5}$$

$$\mathbf{q}_k^{(n)} = \frac{\gamma_k c}{\mu_0} e_z \times \mathbf{p}_k^{(n)}, \tag{B.6}$$

where k =1,2,3,4, ω is the circular frequency of the descending light, c is the light speed, N_k is the normalization constants such that $\mathbf{p}_k^{(n)} \cdot \mathbf{p}_k^{(n)} = 1$. In order to calculate the propagation constant γ_k we have to solve the following biquadratic equation:

$$\begin{vmatrix} \left(\frac{\omega}{c}\right)^2 \varepsilon_{xx} - \gamma_k^2 & \left(\frac{\omega}{c}\right)^2 \varepsilon_{xy} & \left(\frac{\omega}{c}\right)^2 \varepsilon_{xz} \\ \left(\frac{\omega}{c}\right)^2 \varepsilon_{yx} & \left(\frac{\omega}{c}\right)^2 \varepsilon_{yy} - \gamma_k^2 & \left(\frac{\omega}{c}\right)^2 \varepsilon_{yz} \\ \left(\frac{\omega}{c}\right)^2 \varepsilon_{zx} & \left(\frac{\omega}{c}\right)^2 \varepsilon_{zy} & \left(\frac{\omega}{c}\right)^2 \varepsilon_{zz} \end{vmatrix} = 0. \tag{B.7}$$

Then the total transfer 4×4 matrix of a structure consisting of N layers can be obtained from the expression:

$$M = D^{-1}(air) \cdot \prod_{n=1}^{N} (D(n)P(n)D^{-1}(n)) \cdot D(air) \tag{B.8}$$

The complex Fresnel reflection and transmission matrixes are

$$J_t = \begin{vmatrix} t_{xx} & t_{xy} \\ t_{yx} & t_{yy} \end{vmatrix} = 0, \qquad J_r = \begin{vmatrix} r_{xx} & r_{xy} \\ r_{yx} & r_{yy} \end{vmatrix} = 0, \tag{B.9}$$

where elements of the Jones matrix t_{ab} (r_{ab}) implies transmittance (reflectance) coefficient for incoming light polarized in the direction b and outcoming light polarized in the direction a. Expressions for t_{ab} and r_{ab} are as following:

$$r_{xx} = \frac{M_{21}M_{33} - M_{23}M_{31}}{M_{11}M_{33} - M_{13}M_{31}}, \qquad r_{xx} = \frac{M_{33}}{M_{11}M_{33} - M_{13}M_{31}} \tag{B.10}$$

$$r_{xy} = \frac{M_{41}M_{33} - M_{43}M_{31}}{M_{11}M_{33} - M_{13}M_{31}}, \qquad r_{xy} = \frac{-M_{31}}{M_{11}M_{33} - M_{13}M_{31}} \tag{B.11}$$

$$r_{yx} = \frac{M_{11}M_{23} - M_{21}M_{13}}{M_{11}M_{33} - M_{13}M_{31}}, \qquad r_{yx} = \frac{-M_{13}}{M_{11}M_{33} - M_{13}M_{31}} \tag{B.12}$$

$$r_{xx} = \frac{M_{11}M_{43} - M_{41}M_{13}}{M_{11}M_{33} - M_{13}M_{31}}, \qquad r_{xx} = \frac{M_{11}}{M_{11}M_{33} - M_{13}M_{31}}. \tag{B.13}$$

In order to demonstrate the results of simulations, obtained with 4×4 TMM,

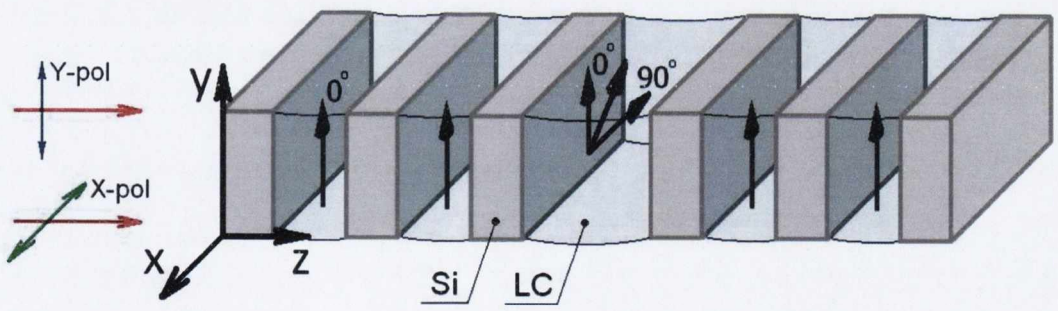

Fig. B.1: Schematic representation of the layered structure with liquid crystal. Thick arrows show the orientation of the liquid crystal director, Φ, in the xy-plane in the mirrors and in the cavity.

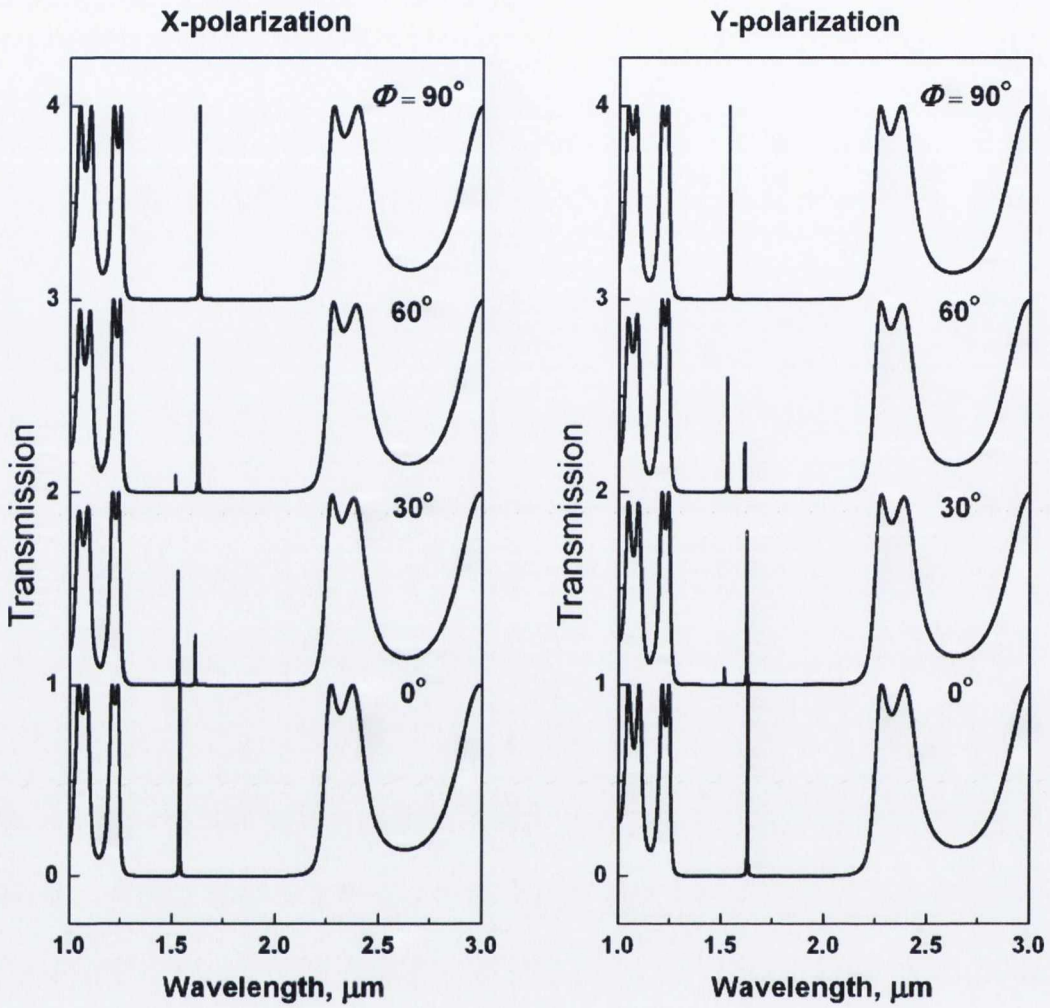

Fig. B.2: Transmission spectra of the silicon one-dimensional photonic crystal structure infiltrated with liquid crystal E7 calculated for different angles Φ between the LC director and y-axis and for different polarization.

we use the silicon one-dimensional photonic crystal structure infiltrated with nematic liquid crystal E7 (see Fig. B.1). The structure consists of the cavity placed between two Bragg's mirrors. The orientation of LC director in the mirrors is constant and aligned along y-axis, while in the cavity the angle Φ between the LC director and y-axis varies from 90° to 0° as shown in Fig. B.1. The ordinary and extraordinary refractive indexes of liquid crystal E7 are $n_o = 1.522$ and $n_e = 1.704$,

respectively. The optical thicknesses of the silicon walls and liquid crystal slabs are determined as a quarter of wavelength, λ ($\lambda \simeq 1.55\,\mu$m).

The transmission spectra of the structure, presented in Fig. B.2, were calculated by means of 4×4 TMM for x- and y-polarizations and shown in Fig. B.2. As can be seen from Fig. B.2 for x-polarization the position of the cavity mode shifts from $1.63\,\mu$m to $1.53\,\mu$m when the angle Φ between the LC director and y-axis changes from 90° to 0°Àt the same time for y-polarization the position of the cavity mode changes from $1.53\,\mu$m to $1.63\,\mu$m when the angle between y-axis and LC director changes from 90° to 0°. Note that the spectra for $\Phi = 90°$ and $\Phi = 0°$ calculated by both the 2×2 and 4×4 matrix methods are coincide. However, for all other angles between 0° and 90° the application of 2×2 TMM results in transmission spectrum with only one cavity mode, while 4×4 TMM yields spectrum with two cavity modes of different relative intensity.